2012

Mixing and segregation in 3D multi-component, two-phase fluidized beds

Norman K.G. Keller
Iowa State University

Mixing and segregation in 3D multi-component, two-phase fluidized beds

by

Norman K. G. Keller

A dissertation submitted to the graduate faculty

in partial fulfillment of the requirements for the degree of

DOCTOR OF PHILOSOPHY

Major: Mechanical Engineering

Program of Study Committee:
Theodore J. Heindel, Major Professor
Shankar Subramaniam
Baskar Ganapathysubramanian
Rodney Fox
Hui Hu

Iowa State University

Ames, Iowa

2012

Table of Contents

List of Figures

List of Tables

Acknowledgements

Special thanks goes to my advisor Dr. Ted Heindel for his guidance and input during this work and the opportunity to conduct this research in his lab.

I also want to thank Dr. Rodney Fox, Dr. Shankar Subramaniam, Dr. Hui Hu and Dr. Baskar Ganapathysubramanian for serving on my committee and providing valuable input and support throughout this work.

Thanks to all my labmates, especially Enes Kadic and Tim Morgan for their support and friendship.

Support for portions of the work described in this paper from the Phillips 66 Company is acknowledged.

Abstract

To operate a fluidized bed reactor most efficiently, one needs to have a good understanding of the hydrodynamics inside the bed as well as a good understanding of the mixing and segregation patterns that occur if the bed is multi-component. Many studies have been carried out in an attempt to address these issues, and the findings have contributed to make a variety of processes more efficient. However, since fluidized beds are an opaque medium, it remains difficult to experimentally investigate hydrodynamics and mixing/segregation patterns without significant trade-offs. This study discusses experimental efforts aimed at understanding mixing and segregation in multi-component cold-flow fluidized bed reactors.

A non-invasive measurement technique called X-ray computed tomography (CT) has been used to experimentally investigate mixing and segregation in 3D fluidized beds. New analysis tools for quantifying the bed “mixedness” and level of segregation in a fluidized bed were developed. The method and analysis techniques are explained in detail. The fluidization gas flow rate, particle size, particle density, mixture ratio, fluidized bed size, and the humidity of the gas stream can have a significant effect on the level of segregation of the fluidized bed. The newly developed analysis tools have been proven to represent the varying levels of segregation sufficiently and have been found to be superior to previous introduced measures.

Chapter 1 Introduction

1.1 Motivation

Fluidized beds have been used in industry since the early 20th century for fuel production and other applications. They feature many positive characteristics such as uniform temperature distribution, high heat and mass transfer rates, etc., that makes it interesting for industrial applications. Although they have been widely used, fluidized beds as a whole are still poorly understood because of the complexity of gas, liquid and solid interactions. Extensive research in areas such as the hydrodynamics and mixing/segregation patterns are necessary to efficiently utilize fluidized beds.

Fluidized beds are usually used for drying processes or chemical conversion processes through heat addition and/or a catalyst. In rare cases they are also used for segregation processes. In all cases, the efficiency of the process is determined by the relative contact area between the different media. Therefore, the more even the material is dispersed, the more efficient the process.

Academic approaches to better understand the operation of these vessels have been found to date back as far as 1955 [1]. Ever since then a lot of different studies have been carried out with varying objectives, mostly addressing specific applications. However, since fluidized beds are an opaque medium, trade-offs need to be made to allow for measurements. In general, measurement techniques can be divided into invasive and non-invasive measurement techniques. Invasive measurement techniques can give insight into a variety of parameters inside the bed when operated, but, due to

their nature, have the potential of altering the processes and behavior of the bed. Non-invasive measurement techniques have the advantage of not interfering with the fluidized bed, but have often been found to yield unsatisfying results or required other trade-offs that altered size, shape, or operating parameters of fluidized beds typically found in industry. As an example, several researchers use optical means to record experimental data [2-6] but, in order to make the fluidized bed transparent, they focused on only a very thin 2D fluidized bed. In this case, valuable information can be gathered with the trade-off of highly increased wall effects and lowered particle-particle interactions.

Studies have also been conducted using computational fluid dynamics models (CFD) for fluidized beds [3, 7-13]. However, since experimental data is very limited, the accuracy of these models is too.

To further improve the usage of fluidized beds in industrial applications and assist the computational development of these facilities, detailed experimental data from 3D fluidized beds gathered through measurements that do not alter the behavior are necessary.

Therefore, this study shows an approach on gaining experimental data on mixing and segregation of multi-component 3D fluidized beds using X-ray CT scans as a non-invasive measurement technique. The method has been built upon the successful completion of earlier studies aimed at the hydrodynamics of single component beds using the same measurement means, conducted by Heindel et al. [14, 15], Franka et al. [16-19] and Drake and Heindel [20, 21].

1.2 Objectives

The objectives of this study are to develop a measurement technique for mixing and segregation in multi-component fluidized beds and to provide accurate experimental data that can be used for verification of computational models. To accomplish this, the following tasks have been identified:

1) Identify parameters that influence mixing and segregation in fluidized beds through a literature review and preliminary experiments by means of visual observation.
2) Conduct preliminary experiments with X-ray CT scans to validate system capabilities.
3) Develop a method to visualize fluidized beds in terms of material distribution using X-ray CT scans.
4) Develop algorithms to analyze material distribution from the CT scans of fluidized beds.
5) Develop methods to characterize the level of “mixedness” in fluidized beds based on material distribution.
6) Complete studies over a range of flow and particle size conditions.

Chapter 2 Literature Review

This chapter discusses aspects of fluidized beds and their operation that are related to this particular research. The first part gives a general overview and examples of industrial use followed by a brief explanation of important characteristics of a fluidized bed. The next section discusses different measurement techniques to study fluidized beds; it is shown how the different techniques are used to acquire data and their associated advantages and disadvantages. Finally the last part gives an overview of the research that has already been done in the field of mixing and segregation in fluidized beds.

2.1 Fluidized Beds

This section provides an overview of fluidized beds from theory and physical setup to operation in industry. It is aimed at summarizing the basics about fluidized beds and fluidized bed processes with respect to the particular research about mixing and segregation mechanisms.

2.1.1 Usage

The first fluidized bed reactor built for industrial application was introduced by Fritz Winkler in 1922 for gasification of coal [22]. The commercial breakthrough for this technology, however, did not happen for another 20 years, when large scale catalytic cracking for fuel was demanded. In the early 1940s, fluid catalytic cracking (FCC) was developed by the oil industry and since then, has become the standard for processing crude oil and the production of fuels and chemicals. Today, more than 350 facilities

utilizing fluidized bed reactors are used to supply the world's energy demand in crude oil products [22].

As the understanding of fluidized bed technology grew, so did the applications and, by the 1950s fluidized beds were used for drying processes, sulfide roasting, and calcinations.

Today fluidized beds are used for catalytic cracking of crude oil, biomass to fuel conversions, and drying and coating processes in many industries.

2.1.2 Overview

A fluidized bed is formed when a dilute phase, such as a gas or liquid, is directed through a solid particulate medium. The fluidization medium enters the bed through the bottom and, as it flows through the bed, loosens up the particles, significantly reducing the friction between particles, which results in the fluid-like behavior.

This process, called fluidization, results in the solid medium achieving fluid-like properties such as free-flow due to gravity and lighter particles floating to the top surface.

2.1.2.1 Physical Design

There are basically two different types of fluidized beds, stationary or fixed fluidized beds (FFB) and circulating fluidized beds (CFB). They use different operating principles and are designed for different applications. A fixed fluidized bed is typically operated with a lower fluidization velocity. Elutriation of particles is not desired; the particles stay in the bed and are in a "batch" mode. A circulating fluidized bed is typically operated

with a higher fluidization velocity to transport particles out of the bed. The particles are then reintroduced at the bottom of the bed to circulate through the system. Depending on the application, each type can be operated as a gas-solid, gas-liquid-solid, or liquid-solid system. Since this study is looking at basic mixing/segregation patterns, it will focus on fixed beds using a gas-solid system.

The vessel in which a fluidized bed is operated is called a fluidized bed reactor (FBR). Although there are a variety of design aspects, any FBR will exhibit the components shown in Figure 2.1 in some form:

- A distributor through which the fluidizing medium is entrained into the bed material.
- A reactor chamber in which the bed is contained.

In addition to these basic design features, typical laboratory FBRs also include:

- A plenum chamber to help evenly disperse the fluidizing gas to the distributor.
- A freeboard region to minimize elutriation.

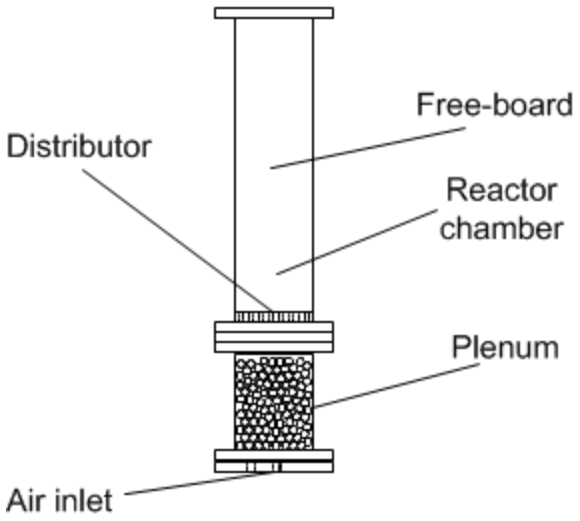

Figure 2.1: Schematic of FBR used for this study.

The fluidizing medium enters the bed through the distributor, which can be a porous or perforated plate, a single nozzle or nozzle array, or just a drilled pipe located on the bottom of the vessel. The design of the distributor has a significant influence on the operation and performance of the vessel and, in general, the more even the fluidizing medium is dispersed when entering the bed, the better the FBR operates.

2.1.2.2 Fluidization Regimes

Depending on the superficial velocity U, which is measured by the volumetric flow rate of the fluidizing medium over the cross-sectional area of the bed, with which the fluidizing gas or liquid passes through the bed, the fluidizing stage of the bed is described by three distinct regimes: (i) fixed bed stage, (ii) incipiently fluidized stage, or (iii) fully fluidized stage.

The rise velocity of the fluidizing medium varies locally throughout the bed. Therefore the fluidizing regimes are described by the superficial velocity.

For sufficiently low superficial velocities, the fluidizing medium merely percolates through the voids between the particles of the bed, the aerodynamic drag on the particles is low, and the bed remains in a fixed stage. As the superficial velocity is increased, drag on the particles increases and begins to counteract gravitational forces causing the particles to separate from each other and the bed expands. The point at which the superficial velocity is just high enough so that the aerodynamic drag on the particles counterbalances the gravity force marks the incipiently fluidized stage and the particles are suspended in the fluid. This state is also known as minimum fluidization. As U is increased, the bed expands further, decreasing the bulk density, and particle motion increases.

Depending on the ratio of fluidization medium density to bed material density, two different stages of fluidization are recognized. For only a small difference in density the bed is fluidized smoothly and gross flow instabilities are damped. This is known as homogeneous fluidization. For a large difference in density the bed is more turbulent, bubbles and channels form frequently and the bed is less stable. This is known as heterogeneous fluidization.

2.1.2.3 Minimum fluidization Velocity

The minimum fluidization velocity, U_{mf}, marks the point at which the particles are just suspended in the fluidizing medium. It is an important measure for all academic research as well as industrial operations to classify a fluidized bed since it sets the lower boundary for the fluidization of the particular bed. The minimum fluidization velocity depends on numerous variables such as particle and fluidizing medium

properties and size and shape of the fluidized bed vessel. It is usually determined experimentally by measuring the pressure drop through the bed [17, 23].

With increasing superficial velocity, pressure drop across the bed initially increases until the minimum fluidization velocity is reached. At this point, the pressure drop through the bed has reached its maximum value and will remain constant for further increases in superficial velocity.

Figure 2.2 provides an idealized graph of a minimum fluidization measurement.

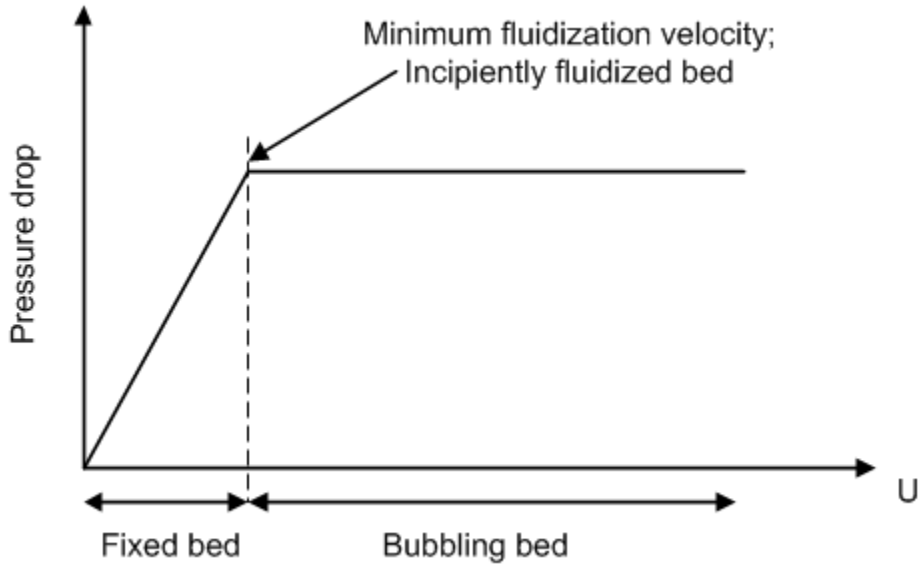

Figure 2.2: Idealized pressure measurement to determine minimum fluidization velocity.

The minimum fluidization velocity may also be calculated with empirically derived equations. Different approaches to calculate the minimum fluidization velocity have been used in the past [3, 22, 24-26]. Their accuracy or range of usage is not part of this study and will not be further discussed.

In terms of multi-component beds, determining the minimum fluidization velocity is more complicated, since through the measuring process itself segregation may occur. With lighter particles segregating out on the top of the bed, the boundaries of the measurement change. A bulk of light particles on the top may operate like a separate bed itself, fluidized by the fluid leaving the lower part. In general, lighter particles also fluidize at a lower superficial velocity. For a multi-component bed this leads to an already fluidized part of the bed on the top, while the lower part might still be in the fixed bed stage.

2.1.2.4 Bubbles and Holdup

Another important aspect for understanding fluidized beds is the effect of bubbling and local and global holdup or concentration.

Bubble size and rise velocity have an influence on the bed mixing and the reaction efficiency. They form in a heterogeneous bed for superficial velocities greater than the minimum fluidization velocity. The higher the superficial velocity, the more violent the bed fluidization, and bubbles may form more frequently and rise faster. Studies have found that bubble size and rise velocity are mostly influenced by the inert bed particle size, the superficial velocity, and the type of distributor [27-31]. In a study by Nienow et al. [32], bubbles were identified as the main influence for mixing. They concluded that mixing occurs as particles are being moved upward by being caught in the wake of bubbles and then move downward when trapped in sinking regions of the bed. Depending largely on the superficial velocity, bubbles may also coalesce and form bigger bubbles as they move upward. This influences the local holdup as the

neighboring regions will be less sufficiently fluidized. For a fluidized bed to operate most efficiently and provide the best mixing, large bubbles should be avoided.

Many studies have also included or been carried out on the holdup of the fluidizing medium and its influence on the performance of the fluidizing bed [27, 28, 30, 31, 33]. As with the bubble behavior, numerous variables were studied to improve the ability to predict or control fluidized bed operations or to simulate fluidized beds using computational fluid dynamics (CFD) software.

2.1.3 Bed Materials

Fluidized bed operations are controlled by many parameters and, depending on the application, a variety of variables shape the physical setup of the bed such as type of particles, number of different types of media in the bed, etc., which makes classification difficult.

A lot of research has been completed to better understand fluidized bed operations. Different researchers focused on a variety of different aspects, such as size and/or shape of the reactor, or reactor components (e.g. the distributor) [28, 34-40]. Other researchers have focused on the size and rise velocity of bubbles or on gas holdup distribution for different types of media [17, 18, 20, 29, 31, 41, 42]. An important factor of fluidized bed behavior is particle size and particle size distribution.

2.1.3.1 Particle Classification

One widely accepted method of classifying fluidization particles in a gas fluidized bed is the Geldart scheme [43] and is an approach to explain fluidization behavior in terms of the particle type. Geldart divided the particles into four different groups,

depending on their fluidization behavior. The reference is marked by the difference in density of the particles to the density of the fluidizing gas and the mean particle diameter. Figure 2.3 illustrates the different particle classes, where ρ* is the difference in solid and fluid density.

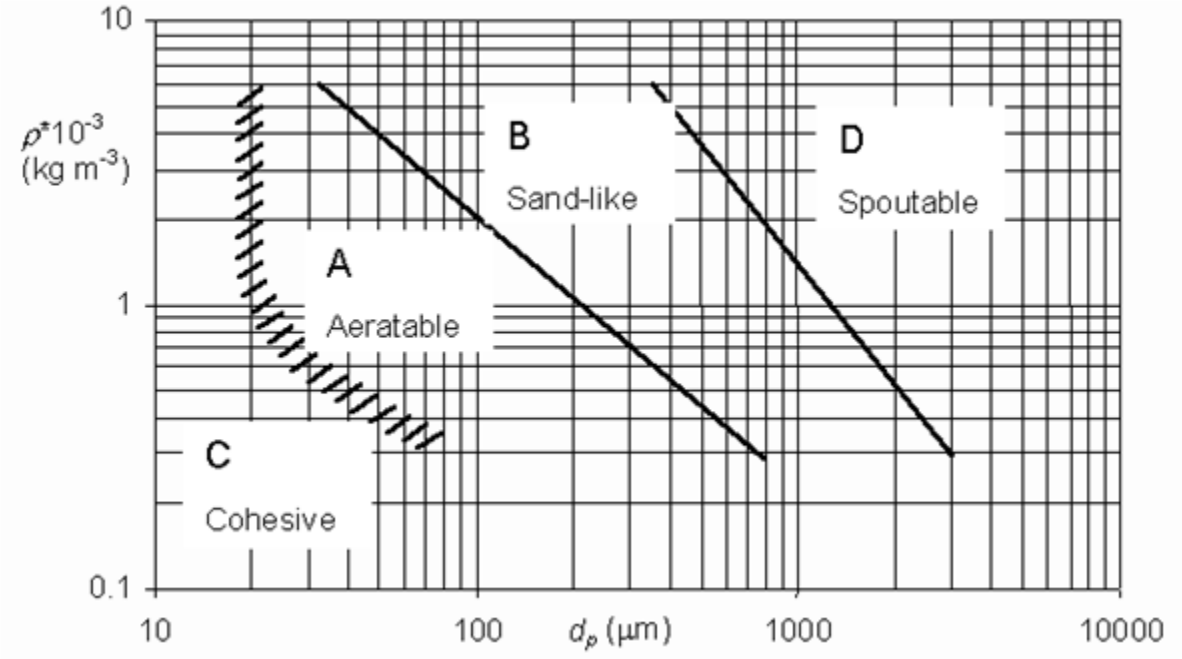

Figure 2.3: Fluidized bed particle classification [43].

According to Geldart, beds of group A particles expand notably when fluidized and bubbles appear to form, split and coalesce frequently indicating that this type of particle is well aeratable. For group B particles, bubble formation starts with a superficial gas velocity just above the minimum fluidization velocity, causing the bed to mix well even at a low superficial gas velocity with less significant bed expansion compared to group A particles.

Group C particles appear to adhere to each other, making it difficult to establish “normal” fluidization of the bed. Mixing and heat transfer between the particles and the

walls or fluidizing gas is poorer in group C particles when compared to group A or B particles. Group D particles are characterized by spouting behavior. Bubbles rise more slowly and mixing is poor even at high superficial gas velocities.

2.1.3.2 Particle Size Distribution

It is difficult, if not impossible, to obtain any amount of inert bed material that is truly mono-dispersed. Therefore the bed material is usually classified over a certain particle size range. Depending on how a certain size range of particles is obtained, it is generally assumed that the particles within a given range follow a Gaussian distribution. There is, in general, a correlation between mixing characteristics and particle size of the inert bed material [44-47]. This leads to different effects if the actual size distribution is different from the assumed distribution.

It has been found that approximations for the minimum fluidization velocities of Geldart B and D powders are most accurate for Gaussian distributions. A flat or bimodal particle size distribution lowers the minimum fluidization significantly and segregation may occur [48].

2.2 Measurement Techniques

Many different techniques have been proposed to study fluidized bed processes. Any measurement is usually aimed at one or more of the following fluidized bed properties: bubble size, bubble rise velocity, fluid holdup, particle concentration, and/or phase velocities. The main obstacle to overcome is that fluidized beds by nature are an opaque medium, making it difficult to draw any conclusions of the internal structures. This section provides an overview of different measurement techniques that have been

used in the past to characterize fluidized beds and gives a guideline for proper operational parameters in different processes. In general, measurement techniques can be categorized into two types, invasive and non-invasive measurement techniques. Each type is further explained in the following subsections.

2.2.1 Invasive Measurement Techniques

Invasive measurements use means of optical or pressure probes located inside the flow to mainly gain local measurements that can later be used to draw conclusions about the global behavior. While there are many possible ways to measure fluidized bed characteristics with invasive measurement techniques, it is not the author's attempt to cover all of them, rather a brief overview is given below.

The main drawback on any of these techniques is that they have the potential of altering the flow and therefore only allow for limited conclusions.

Many researchers have used what is called a pseudo 2D bed. For example Goldschmidt et al. [2] used digital images acquired with a transparent, rectangular, 1.5 cm thick, pseudo 2D bed that allowed visual observations of mixing effects. He used two types of particles that were marked with different distinct colors to allow for differentiation. The observed effects of mixing and segregation can be somewhat extrapolated to a 3D fluidized bed, but wall effects are enhanced while particle-particle interaction is reduced in 2D beds.

It is also possible to place sensors inside the flow. For example, a wire mesh sensor is placed orthogonal to the direction of the flow and can be used to measure bubble frequency, size and velocity. This method may have a good temporal resolution as

shown by Prasser et al. [49] though it cannot give any information about the location of bubbles in the flow and bubble coalescence may be disturbed.

Optical or pressure probes may be placed at the walls of the vessel containing a fluidized bed. With this measuring technique, the flow of the bed is slightly disturbed due to the taps in the walls that are necessary [50]. Also, depending on the size of the vessel, conclusions about internal structures are not feasible since all measurements are local.

2.2.2 Non-Invasive Measurement Techniques

Non-invasive measurement techniques offer detailed information about internal structures without altering the flow. In general, these methods are categorized as either tomographic or radiographic, which gives concentration and holdup measures, or as velocimetry, which provides dynamic features of the bed such as flow patterns and velocity fields. These techniques can be nuclear based, like gamma or X-ray tomography, X-ray stereography and radiography, neutron tomography and radiography or positron emission tomography to name a few, or non-nuclear based techniques like electrical capacitance tomography or ultrasonic tomography. Since this research utilizes an X-ray facility to acquire computed tomography data, the X-ray techniques will be discussed in more detail. A very detailed description of the application of X-rays for flow visualization has recently been presented by Heindel [51]. An overview of other commonly used non-invasive techniques as well as advances in multiphase flow visualization can be found in Heindel [51], Chaouki et al. [52] and Boyer et al. [50].

2.2.2.1 X-ray Radiography/Stereography

X-ray radiography is an imaging method in which X-rays produced by a generator are projected toward an object. The X-rays will penetrate the object and, depending on the density of the object and its internal structure and composition, some portion of the X-ray beam will be absorbed. The transmitted X-rays are captured by a detector on the opposite side of the object creating a two dimensional projection of the three dimensional object with internal structures superimposed upon each other.

For fluidized bed research, this technique can be used to show density variations. More important for research though is stereography. Stereography basically utilizes two radiographic systems at the same time, imaging the same object. Two independent X-ray sources penetrate the object of interest perpendicular to each other. Two detectors on the opposite side of each X-ray source then capture the projections, which are perpendicular to each other. This technique may also be used for particle tracking. A particle that has a significantly different density than the surrounding bed material would be identifiable in the images and, since two planes are imaged, the exact position can be determined. At a fast enough capturing rate, the movement of the particle can then also be tracked [53, 54].

2.2.2.2 X-ray Computed Tomography

X-ray computed tomography (CT) imaging is a technique where multiple radiographic images of the same object are collected and then used to reconstruct a 3D image of the object.

Since radiographs show a superimposed density map of the object from one angle, to being able to identify internal structures, many radiographic images must be acquired from many different angles. Major factors influencing the quality of the X-ray scan are the system characteristics as well as the algorithm used for reconstruction. For example, it is desired to penetrate the object with a monochromatic beam to eliminate effects like beam hardening (which will be explained further in chapter 4). However, since it is not possible to create a perfectly monochromatic beam, the effect of beam hardening cannot be avoided completely. Also, inaccuracy and variations of the source and detector have an influence on the quality of the image.

Different methods for reconstruction include filtered back projection and algebraic methods. Filtered back projection is the most common method used, especially in medical applications, because it is quick and accurate. It also allows for different filtering methods that can be optimized based on the application [55, 56].

These techniques for reconstruction and imaging have been researched intensely by various researchers [55, 57-60] since it was first developed in the early seventies.

2.3 Mixing and Segregation Studies

Studying mixing and segregation in multi-component fluidized beds is important because it is the key factor for efficient operation and has thus been the objective of research as early as the 1960s [61]. As explained in previous sections, any experimental data acquired includes assumptions and drawbacks based on the physical setup. A physical setup to measure particle mixing and segregation without altering the

behavior has only been available on a limited basis and may only offer coarse spatial and/or time resolution. Therefore, high quality experimental data are rare.

Rowe and Nienow [62] studied mixing and segregation with two component beds by visually observing a two dimensional fluidized bed. They concluded that mixing is solely caused by rising bubbles that take particles upward in their wake while downward patterns are observed at the edges of the reactor. They also introduced the terms “jetsam” and “flotsam” for the particles that have a larger density and accumulate at the bottom of the bed relative to the lighter particles that will float, respectively. According to their study, mixing is a function of excess gas velocity, described as the excess flow above the minimum fluidization velocity, which in turn is a function of particle size and density. Segregation will occur close to the minimum fluidization velocity while the bed will mix at superficial velocities above that point, theoretically leading to a perfectly mixed bed for high enough velocities. The study of Rowe and Nienow [62] was also a review and summary of research conducted over a number of years. Based on these findings, a variety of papers were published discussing different issues of single and multi-component beds [24, 31-33, 63].

Since then, research has focused on a variety of different aspects. Baeyens and Geldart [64] studied bubble rise velocities and their impact on particle velocities, proposing a model to predict particle velocities of downward moving particles.

Garcia-Ochoa et al. [65] studied mixing and segregation, varying superficial gas velocities and the mixture composition of multi-component beds using different density particles of larger size in the millimeter range. In their work, they measured vertical

concentration profiles of a circular fluidized bed and compared their findings with the segregation model introduced by Gibilaro and Rowe [11]. They found that their experimental technique was reliable and gave reproducible results. The model by Gibilaro and Rowe was also found to predict the average concentrations well. To allow for comparison of the experimental results with the model, they needed to be able to express solids concentrations in different phases as the bed is fluidized. For this, they used a setup in which vertical plates were inserted into the bed right before the fluidizing gas was shut off, capturing the solids in vertical slices. This allowed for an estimate of the void fractions which was necessary for the model calculations.

Rice and Brainovich [4] studied the effects of size differences for equal density particles in binary mixtures. In their study they used both a 2D and a 3D fluidized bed. The 2D fluidized bed was examined by means of visual observations. For the 3D bed, a vacuum was used to take off a small layer from the top after the bed has been collapsed by shutting off the fluidizing gas. The extracted particles were then examined through sieving and weighing to find the fractions of the respective particle sizes. To express the “mixedness” of the bed, they used a “mixing index”, introduced by Rowe et al. [66], assuming that the fraction of jetsam particles in the upper part of the bed were evenly distributed and can therefore be represented by only a thin layer from the top.

A similar study has been completed by Goldschmidt et al. [2]. A 2D bed was utilized with equal density glass bead particles marked by distinct colors for two different particle diameters that were mixed together in the bed. The fluidized bed vessel was transparent and thus allowed for visual observation of mixing and segregation of the two, distinctly marked, types of particles. The main advantage of this study compared to

earlier ones was that modern high speed imaging technology for data acquisition and computer-automated image processing were used. In the scope of this study a new measure to quantify segregation was also introduced, named the “segregation rate”.

Much of the research today also focuses on developing computer models that accurately simulate a fluidized bed reactor [2, 7-13, 27, 67-84]. But in order to verify simulations and validate computer models, high quality experimental data is essential, which this study will provide.

2.4 Summary

Fluidized beds and fluidized bed research is a challenging field of multiphase flows and combines many different disciplines in the fields of physics and chemistry.

Through different research efforts, much has been discovered about fluidized beds and their characteristics. However, most of the internal structures are still unknown, especially in multi-component fluidized beds.

Particle mixing and segregation for equal size or equal density particles have been studied extensively. However, as has been explained, time and spatial resolution or a physical setup that approximates physical data, are still missing. Also, an appropriate measure on how to quantify segregation has yet to be presented. This research will address these shortcomings.

Chapter 3 Experimental Procedures

To complete the tasks of this study, several experimental setups have been used. The preliminary visual observations have been completed using a small and a large laboratory scale fluidized bed reactor. For the visualizations using the X-ray CT imaging system another small laboratory scale fluidized bed reactor has been used. The physical setups, data acquisition, and custom data analysis software for data processing will be discussed in this chapter.

3.1 Model Fluidized Bed Reactors

Three different model fluidized bed reactors have been used throughout this study, two smaller models for the preliminary visual inspections and the X-ray CT imaging, and a larger model for visual observations only. All experimental setups are discussed in this section.

3.1.1 9.5 cm ID Cold-Flow Fluidized Bed Reactor

For the first set of experimental data through visual observation, a laboratory scale model fluidized bed reactor with 9.5 cm inner diameter (ID), made of clear acrylic plastic to allow visual inspection, has been used.

As illustrated in Figure 3.1, the total height of bed chamber and riser is 40 cm. During the experiments, a wire mesh screen mounted on top of the reactor prevents particles from elutriating. Air enters the plenum through the air inlet on the side of the plenum and is gradually expanded through the distributor, which is a tube with 16, 0.6 cm diameter holes. The air then passes through the aeration plate which contains 100,

1 mm diameter holes, each spaced 0.4 cm apart on a square grid, giving the aeration plate an open area ratio of 1.1%.

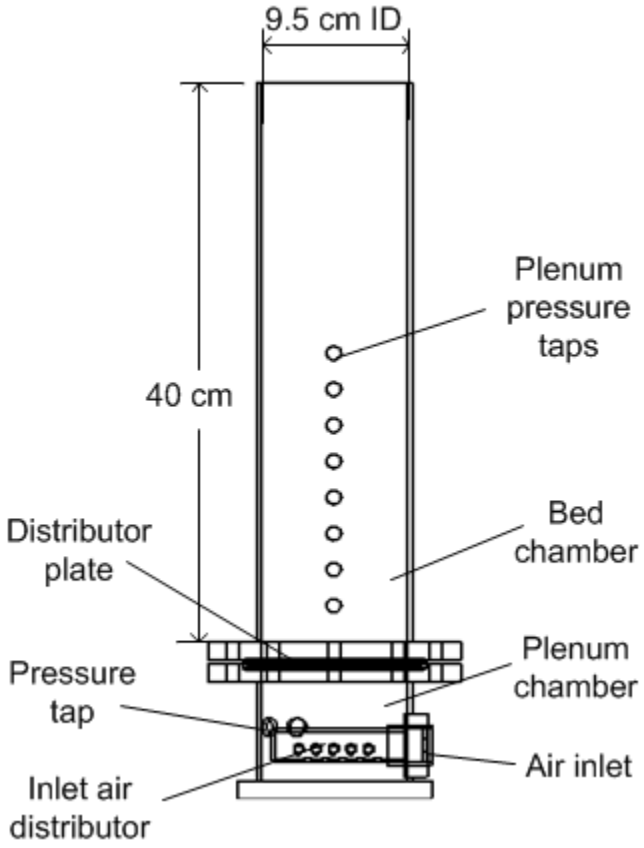

Figure 3.1: Schematic of 9.5 cm ID model cold-flow fluidized bed reactor, used for preliminary visual observations.

3.1.2 10.2 cm ID Cold-Flow Fluidized Bed Reactor

The other smaller model fluidized bed reactor used for this study is comprised of an acrylic tube with an inner diameter of 10.2 cm. The low density acrylic material is chosen to reduce artifacts in the X-ray images. The reactor includes a plenum, bed chamber, and riser or free-board region, following the design of industrial FBRs. Figure 3.2 shows a schematic of the laboratory-scale reactor.

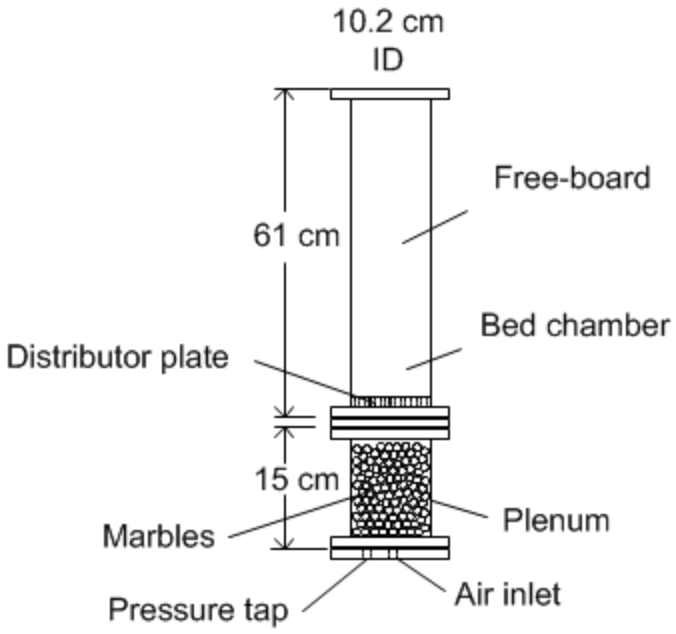

Figure 3.2: Schematic of 10.2 cm ID cold-flow fluidized bed reactor, used for X-ray CT scans.

Air enters the plenum through the inlet in the bottom of the plenum, which is filled with marbles to evenly disperse the air over the bottom of the aeration plate.

The aeration plate, mounted between the plenum and bed chamber, is made of an acrylic plate containing 63 1 mm diameter holes drilled in concentric circles, giving the aeration plate an open area ratio of 0.62%. To prevent particles from falling through the holes or plugging them, a 45 wire mesh screen with 0.04 cm openings is placed right above the distributor plate. Even though the 0.04 cm openings are actually larger than some of the particles that were used (212-300 μm GWS) the chance of particles passing through the screen and the aeration plate is marginal and no particles were found to have fallen through into the plenum chamber at any time during the experiments. Figure 3.3 shows the aeration plate schematic to illustrate the hole pattern and a photograph where the wire mesh screen is already mounted and covers the aeration holes. The aeration plate protrudes into the bed so the bed bottom can be

clearly imaged with X-rays, this plate is attached to a 1.2 cm thick acrylic flange to facilitate mounting.

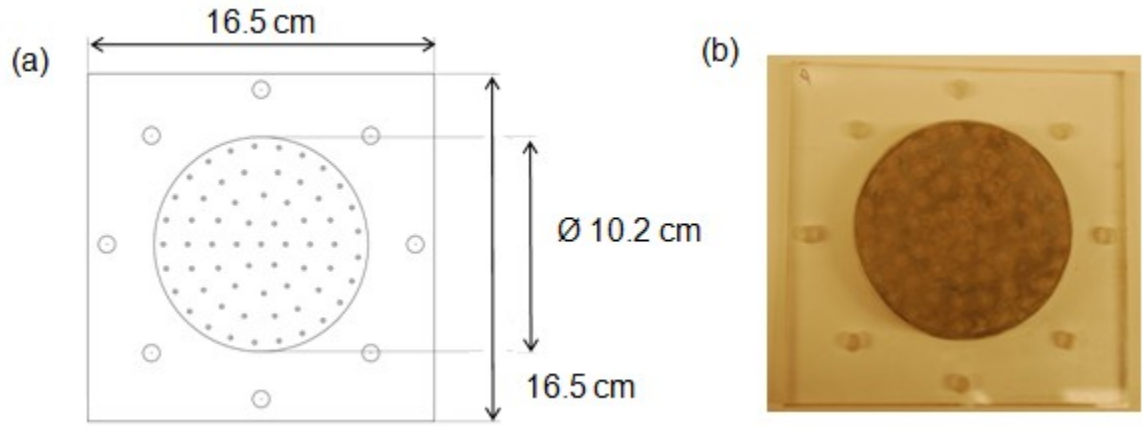

Figure 3.3: Aeration plate, (a) schematic, illustrating the hole pattern, and (b) photograph.

It was required that all materials used to build the reactor be low density to minimize artifacts in the X-ray images. Therefore the reactor walls were 0.64 cm thick acrylic and the connecting flanges were 1.2 cm thick acrylic plates. The various bed sections were held together with nylon bolts and sealed with rubber gaskets. These materials are strong enough to withstand the pressures while minimizing X-ray attenuation. In contrast, steel or other high density reactor materials would attenuate a significant portion of the X-rays.

In addition, to enhance X-ray image quality, it is important that the material surrounding the bed not only have a relatively low density, but also a constant thickness. This promotes an even X-ray absorption by the containing vessel from every angle and thus improves the quality of the images. The flange region was therefore designed with an aeration plate that could be inserted into the bed, effectively moving

the bottom of the bed out of the flange region. The distributor is designed to tightly fit into the reactor tube, so that particles cannot get trapped in the gap between the distributor and the reactor wall. Figure 3.4 shows a photograph of the fluidized bed reactor used in this study with the mounted aeration plate.

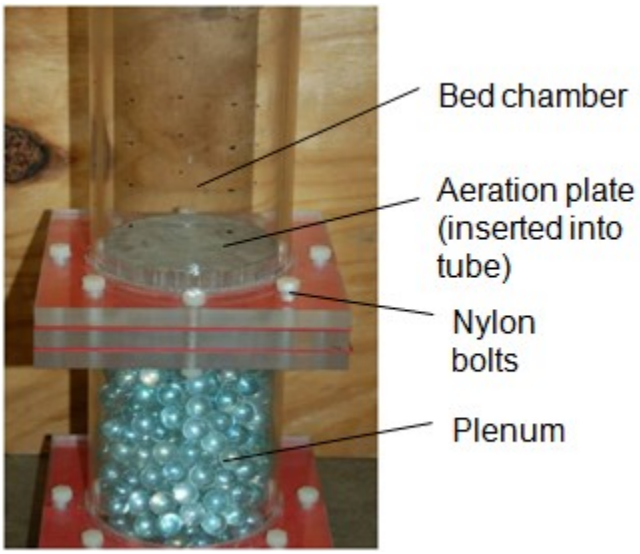

Figure 3.4: Photograph of the fluidized bed reactor used in this study with the mounted aeration plate.

3.1.3 15.2 cm ID Cold-flow Fluidized Bed Reactor

For part of the preliminary visual observations a larger model fluidized bed reactor has been used. As shown in Figure 3.5, its inner diameter is 15.2 cm; other parameters are very similar to those of the smaller fluidized bed reactors, such as the materials used and the design of the distributor.

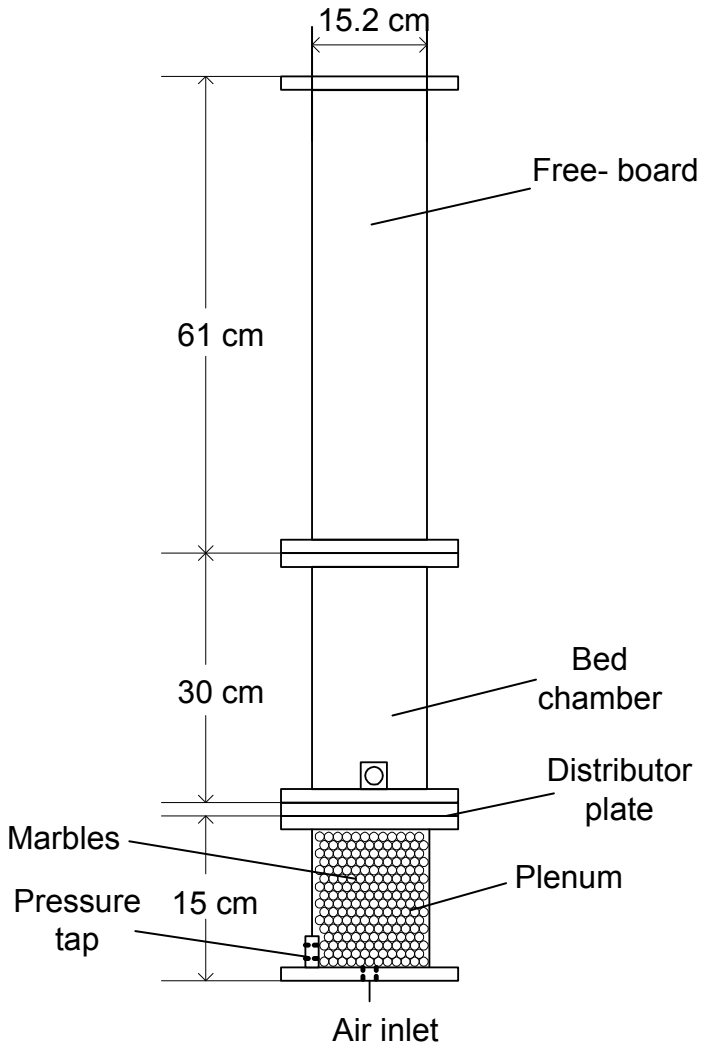

Figure 3.5: Schematic of 15.2 cm ID cold-flow fluidized bed reactor.

The air inlet is located at the bottom of the plenum, which is filled with marbles to evenly disperse the air over the bottom of the aeration plate.

The aeration plate, mounted between the plenum and bed chamber, is made from acrylic comprising 132 1 mm diameter holes drilled in concentric circles, giving the aeration plate an open area ratio of 0.57%. The aeration plate also protrudes into the bed chamber to move the bottom of the bed out of the region of the flange. To prevent

particles from falling through the holes or plugging them, a 45 wire mesh screen is placed right above the distributor plate.

3.2 Fluidized Bed Materials

The materials selected for this study are based on what is usually used in fluidized bed reactors. The inert bed material is often refractory sand because of its thermal properties and availability. For this study, glass beads (GB) have been selected as the inert bed material because they have very similar properties to that of sand, but are better characterized and more uniform in shape, which is beneficial for laboratory experiments. This also allows the experimental data to be used as comparison to simulation results from CFD calculations.

As the second granular material in the bed, ground corncob (GCC) or ground walnut shell (GWS) was selected. In earlier preliminary experiments by visual inspection, GCC was used as the second granular material to model biomass. In subsequent experiments, GCC was replaced with GWS, because GWS is better characterized and therefore can be better modeled in simulations.

GWS is also very similar to biomass, typically used in gasifiers for biomass-to-fuel conversions. It has a lower density than the GB, which is necessary for use with the X-ray system. Close-ups of the GB, GCC and GWS are shown in Figure 3.6. The photographs are taken with a magnification of factor of 10 and show particles in the range of 500-600 μm for each GB, GCC and GWS.

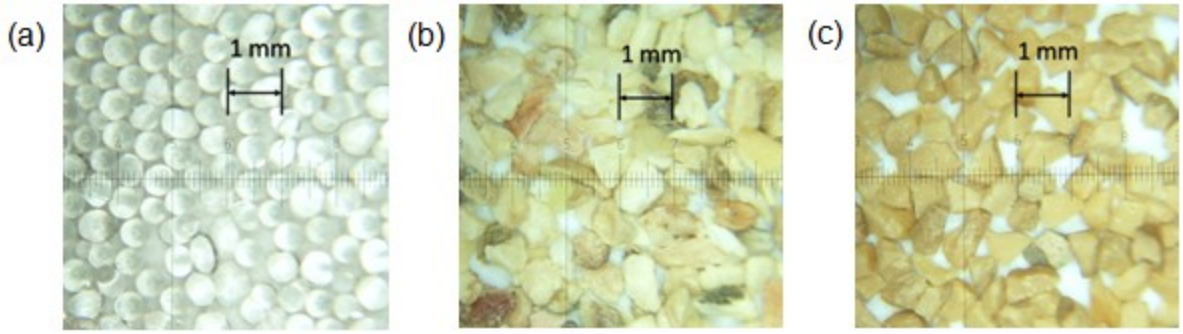

Figure 3.6: Close-ups of (a) 500-600 μm GB, (b) 500-600 μm GCC and (c) 500-600 μm GWS.

As shown in Figure 3.6a, the GB particles are smooth, solid, and nearly spherical, and the particles appear to be in a fairly tight range. Figure 3.6b and (c) show that the GCC and GWS particles are not as smooth and round as glass beads because they are a natural material and the manufacturing process is different; the GCC appear to be more “chuck-like”, “plate-like” or “stalk-like” while the GWS appear to be just “chuck-like”.

For all experiments, glass beads in the size range of 500-600 μm diameter are used as the inert bed material, while the ground corncob and ground walnut shell in three different size ranges (212-300 μm, 500-600 μm and 800-1000 μm) were selected as the second component. After sieving the particles multiple times with American standard sieves, it is assumed that the particles are normally distributed within the size ranges. The particle size range, densities and individual particle mass are listed in Table 3.1. Since this study focuses on the mixing and segregation of two granular type components, all particles were chosen so that they comply with Geldart type B for easy fluidization (Figure 3.7).

Table 3.1: Bed material properties.

Particle properties	Diameter [µm]	Individual particle density (average) [g/cm^3]	Individual particle mass [10^4 g]
Glass beads (GB)	500-600	2.60	1.70 - 2.90
Ground corncob (GCC)	212-300	1.00	0.05 - 0.14
	500-600		0.65 - 1.10
	800-1000		2.60 - 5.20
Ground walnut shell (GWS)	212-300	1.30	0.06 - 0.18
	500-600		0.85 - 1.50
	800-1000		3.50 - 6.80

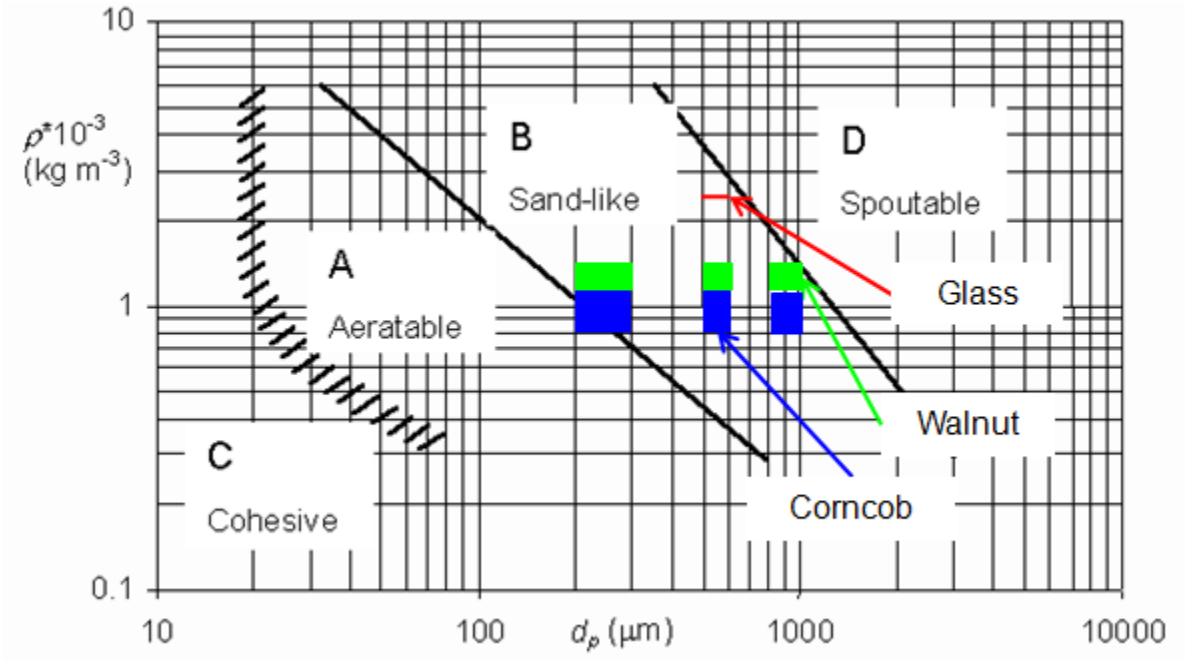

Figure 3.7: Illustration of bed materials within the Geldart classification [43].

3.3 Minimum Fluidization Tests

The minimum fluidization velocity, U_{mf}, is the most used characteristic property of a fluidized bed and is thus used as the reference point for this research study. Although empirical correlations are available (see for example [22]), the composition of the

analyzed beds varies and therefore the experimentally determined minimum fluidization velocity for a full bed of glass beads in the size range of 500-600 μm for a bed of one diameter bed height has been chosen as the reference point.

The minimum fluidization is then determined by measuring the pressure drop through the bed. Since there is a noticeable hysteresis effect between fluidization and de-fluidization, which is caused by packing effects, the pressure drop through the bed is typically measured during de-fluidization. In this study, pressure measurements are taken in five Lpm increments starting at 175 Lpm. A pause of five seconds is maintained before taking the pressure measurement after every adjustment to a new flow rate to allow the system to stabilize.

Measuring the pressure for different flow rates with no bed material in the reactor gives the pressure drop that is attributed to the plenum and aeration plate and can then be subtracted from the bed measurement. All experiments have been repeated multiple times to yield a good sample average. For a bed height of one column diameter of glass beads in the size range of 500-600 μm, the 9.5 cm cold-flow fluidized bed reactor used in this study had a minimum fluidization velocity of U_{mf} = 15.3 cm/s (65 Lpm), the 10.2 cm FBR had a minimum fluidization velocity of U_{mf} = 21.3 cm/s (105 Lpm), and the 15.2 cm FBR had a minimum fluidization velocity of U_{mf} = 20.1 cm/s (220 Lpm).

3.4 Flow Loop and Data Acquisition

The test setup used for this research study is an integrated and, for the most part, a computer automated system. The fluidizing medium is air from the compressed air supply of the laboratory. After filtering the compressed dry air, it enters a control board

featuring a pressure regulator, flow meter, and several ball valves to adjust the flow rate. The pressure regulator is a stainless steel “Watts Fluidair” with a regulating pressure range of 0-862 kPa (0-125 psi) and a maximum inlet pressure of 2.07 MPa (300 psi). The flow rate is measured with an Aalborg mass flow meter, model GFM 771, that allows measuring flow rate in the range of 0-1000 Lpm. The flow meter is connected to a data acquisition computer so that the reading can be automatically recorded.

The flow rate can be adjusted in two ways, depending on the application. For the mixing and segregation experiments, a constant flow rate is desired and the most convenient way to adjust the flow is using a series of ball valves. The first ball valve is mounted right in front of the flow meter and is used to adjust the flow rate; another ball valve is mounted right at the inlet to the fluidized bed reactor and is used for rapidly ramping to the desired flow rate and abruptly shutting off the fluidizing gas to collapse the bed. For minimum fluidization tests, an automatic control valve is also available that allows for a computer controlled flow rate.

Figure 3.8 shows a schematic of the flow loop setup. The automatic control valve, as well as the flow meter, is interfaced with a data acquisition computer that is also used to control the X-ray imaging facility and record the X-ray images. This is further explained in section 3.5.

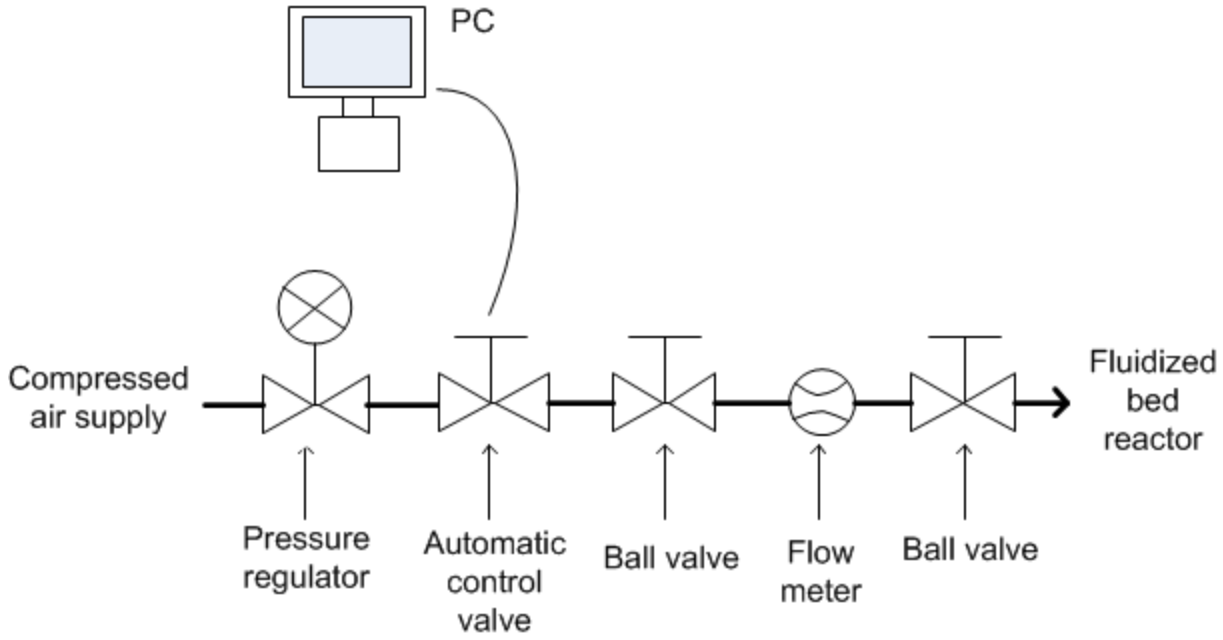

Figure 3.8: Schematic of flow loop.

3.5 X-ray Imaging System

The X-ray imaging facility used for this research is unique in its design and was specifically developed at Iowa State University to visualize opaque multiphase flows. It uses two Lorad LPX 200 portable X-ray tubes that produce X-rays at a specific, user selected power level. The X-rays are emitted through a window that allows for a 60° horizontal and 40° vertical cone beam. Voltage and current can be adjusted from 10 to 200 kV and 0.1 to 10 mA, respectively, with a maximum total power output of 900 W per tube. The tube heads are liquid cooled. The beam is limited by a collimator surrounding the source. Additionally, copper or aluminum filters may be placed in front of the window to filter out lower energy X-rays. Opposite each X-ray source is a detector with a CCD camera. The detector can be either an intensifier or a scintillator screen. The intensifier uses electrons to create a visible picture and typically has high temporal and spatial resolution. The coupled CCD camera can record up to 60 frames per second (fps)

depending on binning settings, and can therefore be used for dynamic systems, e.g. for particle tracking velocimetry. The drawback with this detector/camera pair is that the image is created by electrons. Thus it is sensitive to magnetic fields.

The other detector/camera pair is the primary imaging device used for CT imaging and was used extensively in this study. It uses a square 44×44 cm cesium-iodide (CsI) scintillator screen, which transforms the incident radiation into visible light. The crystals in the scintillator screen need to be excited before taking any data, because the measured intensity might vary otherwise. Because of this, the scintillator screen has poor temporal resolution, but good spatial resolution. The images from the CsI detector are captured by an Apogee Alta U9 camera with a 50 mm Nikon lens. The camera has 3072×2048 pixels with binning options and is thermoelectrically cooled to allow for long exposure times.

The X-ray sources and detector/camera pairs are mounted on a rotating ring with an inner diameter of 1.0 m. The cooling lines and all the electrical connections are all combined to go through one location on the ring. This allows for a complete rotation around the object of interest from 0 to 360°. As explained earlier, to reconstruct a 3D image from a tomographic scan, multiple images must be acquired from different angles. Therefore, the X-ray source and detector/camera pairs are rotated around the object and images are taken at every degree, resulting in 360 images. Figure 3.9 shows a photograph of the facility with a fluidized bed mounted in the imaging region.

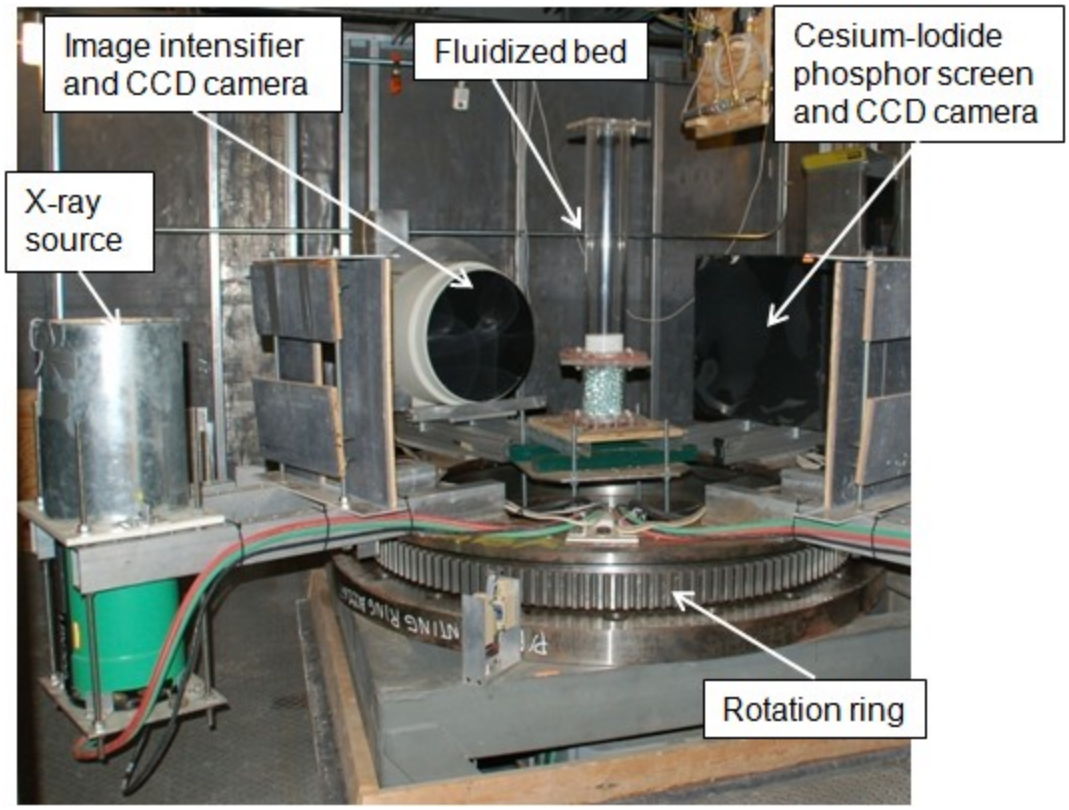

Figure 3.9: Photograph of the X-ray flow visualization facility.

To ensure safety when operating the X-ray facility, all components are mounted inside a fully leaded, 2.0 m tall and 3.4 m by 3.8 m wide room. All components are controlled from the outside. The X-ray sources have their own control units as part of the Lorad LPX 200 system. A data acquisition computer controls all other components:

- The stepper motor to rotate the ring.
- The cameras to capture images.
- The automatic control valve and flow meter for the fluidizing gas.

3.5.1 X-ray CT Data Acquisition

A custom developed program acquires the images for a CT scan by acquiring an image, rotating the source detector pair by one degree, then taking another image. This

is done through 360 degrees. Each of the 360 images are saved to a hard drive and then reconstructed to form a CT scan.

The program also applies a normalization algorithm to the images. This is to compensate for irregularities for each pixel between minimum and maximum value possible. Theoretically, these values should be identical for each pixel, but they actually vary because of manufacturing variations. Radial variations in X-ray intensity are also observed because the X-ray beam is cone-shaped, with the intensity in the center of the beam being higher than on the edges. To account for this, a normalization algorithm is applied to each frame. The minimum values are recorded for no X-ray exposure at all, commonly referred to as a “dark” image. All values in this image will be zero or very close to it. The maximum values are recorded with the X-rays on at the desired power level and no object is between the source and detector. This image is commonly referred to as the “flat” image. With the X-rays on at the same power level and the object in the center of the ring, all recorded values will be in between the dark and flat image. Using the dark and flat images, every pixel for every recorded image is then scaled to compensate for the irregularities and the cone-shaped beam.

For this research only the Apogee Alta U9 camera with the scintillator screen has been used. The 3072×2048 pixels have been condensed by 4×4 binning, i.e., the average value of 16 pixels in every consecutive 4×4 array is calculated and set for one pixel value. Therefore the collected images are 768×512 pixels. This is necessary so that the reconstructed 3D images later are not too large in size yet still provide high enough spatial resolution.

3.5.2 3D Image Reconstruction

The 3D reconstruction of the 360 X-ray images is completed using the filtered back-projection algorithm. Among all methods available, this is the most common because it offers a high quality result with acceptable computational effort [55, 56]. Basically, for every 3D pixel in space, called a voxel, the corresponding pixels from the 2D images are found and the voxel value is calculated as the average.

Before reconstruction, the images are saved on the hard drive of the data acquisition computer in a special format, commonly known as “sinogram” files. For this file format all pixel values that correspond to the same row from each 2D image are sorted into one sinogram file.

After reconstruction the files are saved in the “volume” file format as a 3D image. One voxel of the image represents a cube with side length a = 580 µm. Figure 3.10 gives an illustration of a sample of a static bed.

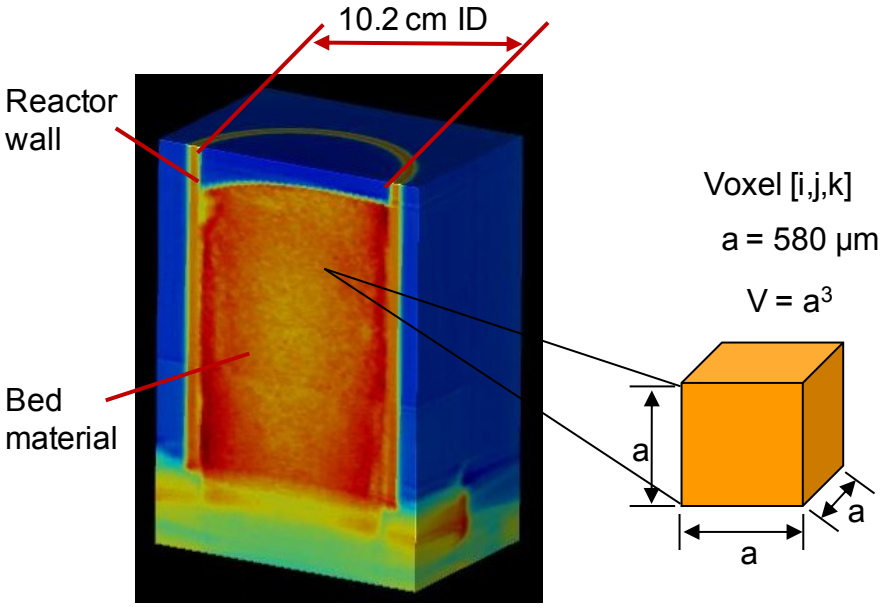

Figure 3.10: Example of 3D image of a random bed, not fluidized.

3.6 Experimental Overview

This section describes the experiments that have been completed for this study. The first part describes the preliminary series of experiments by means of visual observation, which have been completed to identify factors that influence mixing and segregation in a fluidized bed. The second part describes the experiments completed with the X-ray CT system.

3.6.1 Preliminary Visual Observations

To identify factors associated with fluidized bed operation that influences the mixing/segregation of a two-component bed the most, a series of experiments have been completed by means of visual observation. These experiments have been completed using the 9.5 cm ID FBR and the 15.2 cm ID FBR. The model biomass used first was GCC in three different particle size ranges (212-300 μm, 500-600 μm, and 800-1000 μm), mixed with 500-600 μm GB as the inert bed material. Since it was found that GCC is not adequate for modeling in simulations, because it is not as well characterized, for subsequent experiments GWS in the same particle size ranges has been used. Experiments have been completed with different mixture ratios of GCC/GB or GWS/GB (25/75, 50/50, and 75/25) as well as different initial conditions (GCC on top of GB or the other way round, and also for GWS) and other parameters. Table 3.2 lists all the parameters considered for these experiments.

Table 3.2: Parameters of experiments for preliminary visual observations.

Parameter	Range
Model FBR	9.5 cm ID, 15.2 cm ID
Volume ratio [% GCC/% GB or % GWS/% GB]	25/75, 50/50, 75/25
Initial condition	GCC or GWS on top of GB (segregated) GB on top of GCC or GWS (segregated) GCC or GWS and GB well-mixed
Fluidization time	0, 10 s, 20 s, 30 s, 1 min, 2 min, 5 min, 10 min
U_g/U_{mf}	1, 1.5, 2, 3
GCC, GWS particle size [μm]	212-300, 500-600, 800-1000
Gas stream humidification	yes, no

The experiments have been recorded by means of visual observation using a Sony Cyber-shot 12.1 mega pixel digital camera. Videos of dynamic beds have been recorded with a resolution of 640 x 480 pixels. Also, for the above noted fluidization intervals, pictures have been recorded of collapsed beds after the fluidizing gas was abruptly shut off.

Although the recorded images do not allow for detailed or quantitative analysis of the 3D bed, it was useful for determining factors that influence the mixing in a fluidized bed. During this phase it was found among other things that the equilibrium condition is reached quickly and doesn't change when fluidized longer. Figure 3.11 shows an example series to illustrate these points.

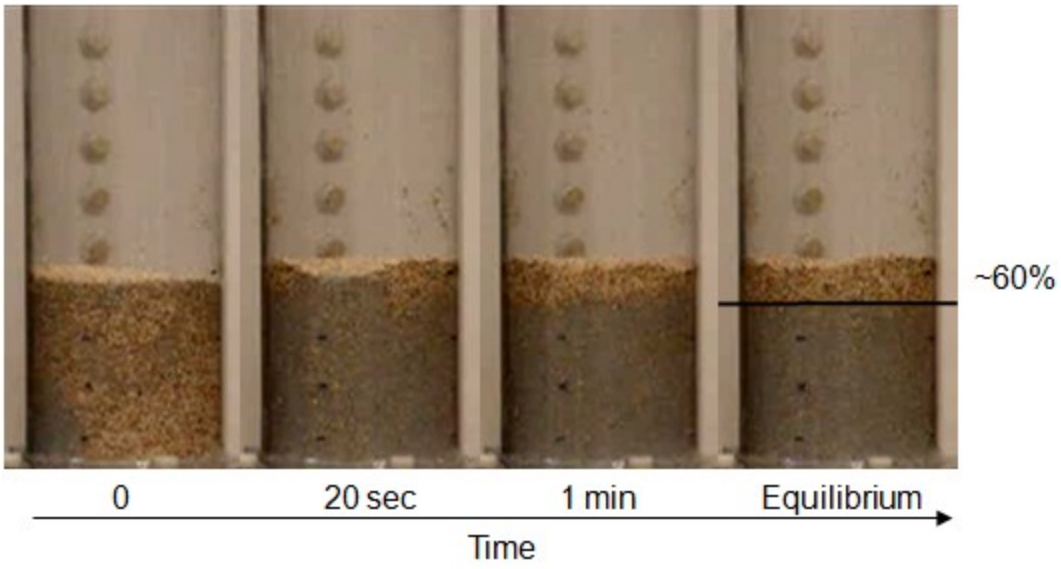

Figure 3.11: Results from visual observation of a bed of 25% 800-1000 μm GCC mixed with 75% 500-600 μm GB, initially well-mixed, fluidized with $U_g = 2\ U_{mf}$ humidified air.

3.6.2 Experiments with X-ray CT Scans

In order to verify or disprove the findings from experiments through visual inspection, experiments are completed with X-ray CT imaging, which allows studying the internal structure of the opaque fluidized bed. With the tools available, images are taken in fixed beds only. That is, for all mixing and segregation measurements in this study, the bed has been brought into the desired stage by fluidizing it at a specified flow rate for a given amount of time and then collapsing the bed by abruptly shutting off the fluidizing gas. With the bed collapsed, an X-ray CT scan was then taken to determine the material distribution. The initial bed conditions (zero seconds) are assumed to be "well-mixed".

Beds have been analyzed using various mixture compositions filled with 212-300 μm, 500-600 μm and 800-1000 μm GWS as the model biomass mixed with 500-600 μm GB as the inert bed material, in a ratio of 25%/75%, 50%/50% and 75%/25% by volume

for a total bed height of one column diameter. The beds have been fluidized with different superficial gas velocities of U_g = 1 U_{mf}, 2 U_{mf}, or 3 U_{mf}; where U_{mf} is the minimum fluidization velocity for 100% GB (U_{mf} = 21.3 cm/s). Table 3.3 provides an overview of all parameters of the completed X-ray CT scans.

Table 3.3: Parameters of experiments with X-ray CTs.

Parameter	Range
Model FBR	10.2 cm ID
Volume ratio [% GWS/% GB]	25/75, 50/50, 75/25
Fluidization time [s]	0, 20, 40, 60
U_g/U_{mf}	1, 2, 3
GWS particle size [µm]	212-300, 500-600, 800-1000
Gas stream humidification	yes, no

3.7 Data Analysis

The volume files must be processed through multiple steps to interpret the collected data. The reconstruction CT scans yield a 3D image of the internal structures on a CT scale of -1000 to 3000 [85]. This must be interpreted in terms of material distribution for further analysis. This section provides the background on the technique used to convert the CT images into volume fraction or material content maps for the systems explored in this study.

3.7.1 Beam Hardening

The biggest challenge with this X-ray technique is commonly known as beam hardening. It is caused by lower energy X-rays being more readily attenuated than higher energy X-rays. Ideally, a monochromatic X-ray beam is desired. Practically, X-

rays are almost always polyenergetic and therefore have a fraction of low energy X-rays with a different attenuation coefficient, μ. For any given object with constant density but varying thickness, this will cause the scan image to show higher density in the thicker areas verse a lower density towards areas where the object is thinner.

To illustrate this effect, Figure 3.12 shows a cut through the center slice of an X-ray CT image reconstructed without accounting for beam hardening. The image shows the 10.2 cm ID reactor filled with 500-600 μm GB. Since the reactor is cylindrically shaped, the X-rays passing through the center have to travel through more material than the X-rays passing through the edges. The attenuation can thus be expressed as a function of radius. The image in the original is on a gray scale; false coloring has been applied to enhance the visual effect.

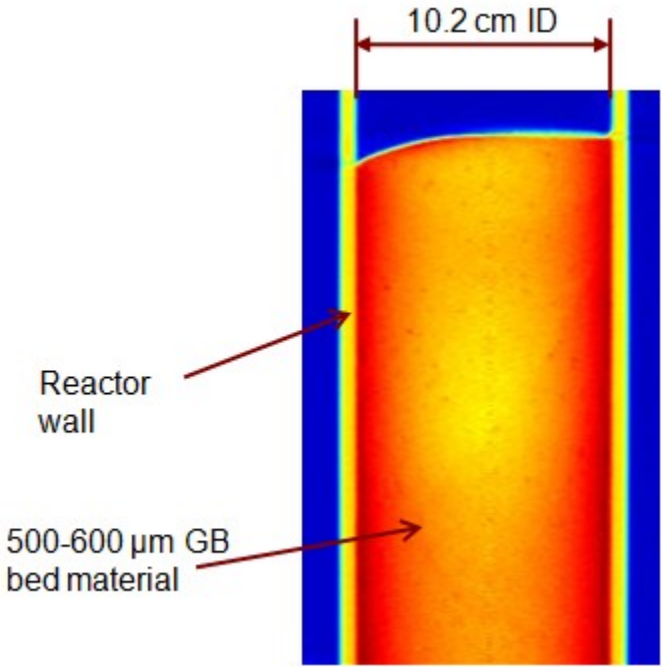

Figure 3.12: Center slice of an X-ray CT scan of a 10.2 cm ID static FBR filled with 500-600 μm GB to illustrate effects of beam hardening.

There are ways to counteract beam hardening. If the material is known, the variation of attenuation over change in thickness for a specific X-ray beam, controlled by the power settings, can be measured and the results corrected accordingly. However, the object in this study is composed by two different granular materials with unknown composition for any control volume. Therefore this method cannot be applied.

A method has been found and developed in this study to account for beam hardening and yield accurate scans with high resolution of the internal structure of the FBR. This is achieved by using reference scans of well-mixed static beds of known composition. A detailed description of this method is given in section 3.7.2.

3.7.2 Data Pre-Processing

To convert the CT scan files into volume fraction files that give the biomass content for each voxel, a set of reference scans are used. The reference scans are acquired for a known material ratio by volume assuming the bed is well mixed. Eleven reference scans are taken ranging from 100% GB to 100% GWS in 10% steps by volume. Table 3.4 shows an overview of the reference scans taken.

Table 3.4: Overview of reference scan composition.

Reference scan	Volume ratio
1	100% GB
2	10% GWS + 90% GB
3	20% GWS + 80% GB
4	30% GWS + 70% GB
5	40% GWS + 60% GB
6	50% GWS + 50% GB
7	60% GWS + 40% GB
8	70% GWS + 30% GB
9	80% GWS + 20% GB
10	90% GWS + 10% GB
11	100% GWS

As mentioned above, the variation of attenuation can be expressed as a function of radius. Therefore, for each reference scan representing a known material composition, the radial variation of the CT values, i.e., the voxel values after the reconstruction, is sought.

The mixed beds are first brought into a well-mixed stage. Then the scan is taken from the fixed bed and reconstructed. With custom developed software, the region inside the bed is identified and the voxel values arranged as a function of radius, i.e. all voxel values that are in the same annulus are listed in one category. The average is then taken for each annulus. The result is a curve that represents the average voxel values over the radius for a certain material composition determined by volume ratio of GWS to GB. Figure 3.13 gives an example of the results for mixtures with 500-600 μm GWS and 500-600 μm GB. Note similar reference scans must be obtained with either 212-300 μm or 800-1000 μm GWS and 500-600 μm GB.

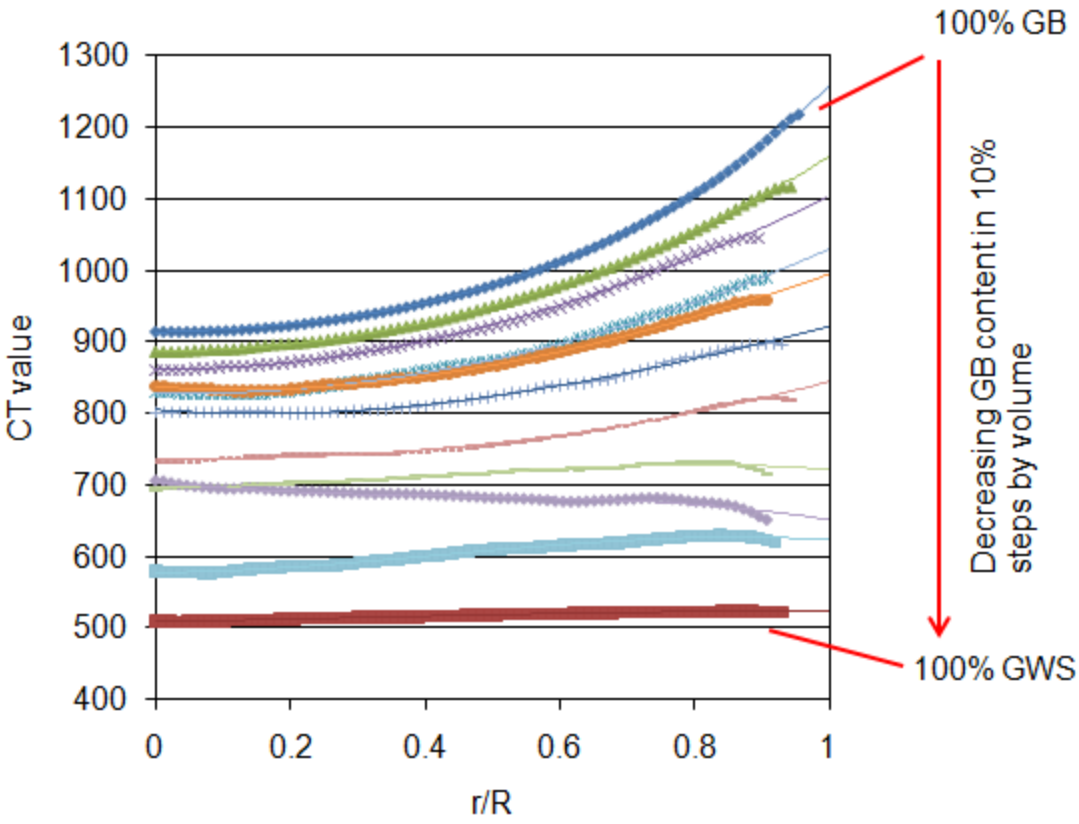

Figure 3.13: Reference scans for mixtures with 500-600 µm GWS in the 10.2 cm ID model FBR.

Figure 3.13 also demonstrates the dependence of attenuation on the density of the material. The top curve represents the CT values as a function of the radius for a bed of 100% 500-600 µm GB and shows that the CT values for these are just above 900 in the center and increasing towards the edge following a third order polynomial pattern with the highest value at the edge of around 1250. The bottom curve represents the CT values as a function of the radius for a bed of 100% 500-600 µm GWS. Since GWS has a significantly lower density it is also significantly less effected by beam hardening. Therefore the CT values are still the lowest in the center at just above 500 and the highest at the edge at around 520, but significantly flatter with only marginal difference from center to outside of the FBR.

To convert the images of the X-ray CT scans of any of the experiments, each voxel is individually interrogated and its position as a function of the radius is considered. A fluctuation of voxel values as a function of bed height has been considered as well, but experiments showed no evidence of such influence. Therefore the volume fraction of any voxel value within the bed is determined by its radial position and the CT value. To estimate the true volume fraction of an individual voxel, accounting for beam hardening as a function of radius, a linear interpolation between the reference curves in Figure 3.13 is used; this has been found to be computationally efficient while maintaining satisfactory accuracy.

The success of this method can be demonstrated by sample images. Figure 3.14 illustrates the center slice of a scan of a random mixture of inert bed material with 500-600 μm GWS in the 10.2 cm ID model FBR. It can be seen that the patterns in the original CT scan image (left) are also found in the converted material content image (middle). In the converted image only the region of interest is analyzed, i.e., only the bed itself, leaving out the reactor walls and flange region. In this figure, the white regions represent 100% GWS while the black regions in the region of interest correspond to 100% GB.

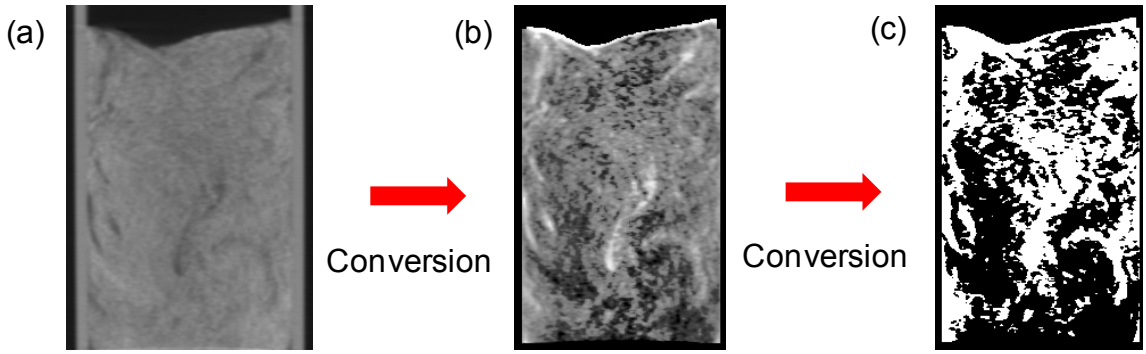

Figure 3.14: Center slice of a sample of a random mixture of inert bed material with 500-600 μm GWS in the 10.2 cm ID model FBR, (a) original CT scan image, (b) converted material content image, and (c) converted binary image.

Also illustrated in Figure 3.14, for further processing of the images, especially to extract features to characterize the particular bed, it is of interest to also have a binary image. Therefore, the material content image is further converted into a binary image, featuring voxel values that represent either 100% GWS or 100% GB. To convert the material content image into a binary image, the appropriate threshold must first be found. As an example, for a bed with 25% GWS, if the GWS is very evenly dispersed in the inert bed material, a threshold of 50% percent would yield a binary image with no GWS at all. Therefore an algorithm calculates the total amount of GWS in the particular bed and compares it with the known initial amount of GWS by volume. A trial-and-error iteration is used to correct the threshold value until the overall error is less than 5%.

Chapter 4 Visual Observations of Mixing in Multi-Component Fluidized Beds[1]

4.1 Abstract

Fluidized bed reactors are used in many industries because they generally have a uniform temperature distribution, low pressure drop, and high heat and mass transfer rates. Fluidized beds have been used in processes such as combustion, pyrolysis, and/or gasification of solid fuels such as biomass. There is usually a notable difference in the fluidization behavior between the solid fuel particle and the fluidized bed media (e.g., refractory sand) due to contrasting size, shape, and particle density; these differences can lead to poor solid-fuel distribution and diminished performance. The hydrodynamics in a fluidized bed drive gas-solid contact, and thus, have a significant influence on fluidized bed performance. Although fluidized bed hydrodynamics are key parameters in their operation, they are still poorly understood, particularly when the solid fuel component, like biomass, is significantly different from the fluidized bed media in particle size, density, sphericity, porosity, and/or other characteristics.

This study summarizes a series of visual observation experiments when a model biomass is mixed with inert fluidized bed material in a 3D laboratory scale cold-flow fluidized bed. The model biomass is composed of either ground corncob (GCC) or ground walnut shell (GWS) in three different size ranges (212-300 μm, 500-600 μm, and 800-1000 μm), while the inert bed material is 500-600 μm glass beads (GB). Different

[1]Based on: Keller, N.K.G., and Heindel, T.J., 2012. Visual Observations of Mixing in Multi-Component Fluidized Beds. International Journal of Chemical Reactor Engineering, under review.

mixture ratios and initial conditions have been explored. All bed combinations are fluidized at several flow velocities while particle segregation is observed and documented. Fluidized beds with two different diameters have been used to assess the effect of reactor diameter on particle mixing. It is shown that particle size and density can play a significant role in mixing, and that segregation can be enhanced by reducing particle electrostatic forces simply by humidifying the fluidizing gas stream.

Keywords: biomass processing, fluidized bed, hydrodynamics, mixing, segregation

4.2 Introduction

With expected shortages in fossil fuel supplies and environmental changes, biomass as an energy source has gained a lot of interest during the past decade due to its potential to greatly reduce greenhouse gas emissions and to serve as a permanent, renewable energy source. Many studies have been carried out on the potential of biomass as a renewable energy source as well as on the technologies to most efficiently convert biomass into useful energy forms [86-92]. Among these technologies, thermochemical processing of biomass appears to be one of the most promising. Thermochemical processing will most likely utilize either pyrolysis or gasification in a fluidized bed reactor because of its efficient mixing properties, low pressure drop, and high heat and mass transfer rates. The process efficiency is determined by the mixing and segregation behavior of the particles in the bed. However, since biomass particles have different physical properties (e.g., size, shape, and density) than the bed material (e.g., refractory sand), an investigation on the mixing and segregation behavior in a fluidized bed is necessary to efficiently utilize biomass within a fluidized bed.

Mixing and segregation of different kinds of particles in two- and three- dimensional fluidized beds has been investigated over the past three decades and cover aspects such as mixing/segregation mechanisms and patterns as well as other important factors of fluidized bed operation [2, 4, 32, 46, 62, 93-99]. The hydrodynamic behavior of binary fluidized beds is strongly influenced by the difference in physical properties of the respective particles, particularly size and density. Nienow et al. (1978) [32] pointed out the relationship between the superficial gas velocity and the mixing/segregation behavior in a coal gasifier. According to their study, segregation will occur at lower superficial gas velocities while mixing is solely due to rising bubbles.

The objective of the current study is to examine the mixing and segregation behavior of biomass particles in a fluidized bed composed of a model biomass (ground corncob or ground walnut shell) and bed material (glass beads) by means of visual observation. Emphasis has been placed on covering a multitude of different factors including the influence of superficial gas velocity, humidity of the fluidizing gas stream, type and size of biomass, and the fluidized bed diameter. It will be shown that particle size and density, as well as the humidity of the fluidizing gas stream, have a significant impact on the mixing and segregation behavior in a two-component fluidized bed.

4.3 Experimental Procedures

4.3.1 Fluidized bed reactors

To assess bed diameter effects, two different sized fluidized bed vessels have been used. Both are laboratory scale, model fluidized bed reactors with different inner diameter (ID) but otherwise exhibiting the same features. A 9.5 cm ID fluidized bed

reactor, referred to as “Small FBR”, and a 15.2 cm ID fluidized bed reactor, referred to as “Large FBR”.

4.3.1.1 9.5 cm ID model cold-flow fluidized bed reactor

For the first set of visual observations, a laboratory scale model fluidized bed reactor with 9.5 cm inner diameter (ID) was used that was made of clear acrylic plastic to allow visual inspection. As illustrated in Figure 4.1, the total height of the bed chamber and riser is 40 cm. During the experiments, a wire mesh screen mounted on top of the reactor prevents particles from elutriating. Air enters the plenum through the air inlet on the side of the plenum and is gradually expanded through the distributor, which is a tube with 16, 0.6 cm diameter holes. The air then passes through the aeration plate which contains 100, 1 mm diameter holes, each spaced 0.4 cm apart on a square grid, giving the aeration plate an open area ratio of 1.1%. To prevent small particles from dropping through the distributer plate or clogging it, an American standard 45 mesh screen with openings of 0.04 cm is attached to the plate. The top of the reactor is open to the atmosphere.

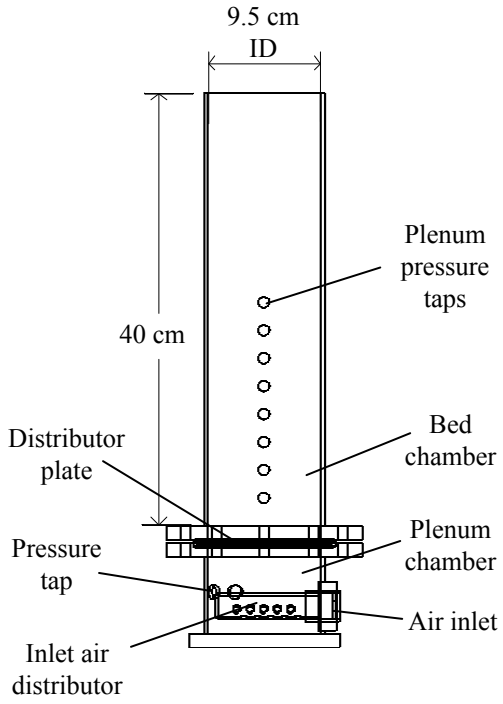

Figure 4.1: Small model fluidized bed reactor.

Gas enters the plenum through the inlet and pressure measurements are used to identify the minimum fluidization velocities for this research. Pressure is recorded with a Dwyer 0–34.5 kPa pressure transducer located in the plenum wall. The transducer has a maximum error of ±0.25% of the full scale reading (±86 Pa). The compressed air supply from the laboratory serves as the fluidizing gas for the beds. The air stream is controlled through a series of ball valves, pressure regulators, and four flow meters as outlined by Franka (2008) [16]. Flow meter error is less than ±2% of the full scale reading. The pressure transducer and flow meters are interfaced to a computer-based data acquisition system. Average pressure and gas flow rates are recorded to determine the minimum fluidization velocity as well as the superficial gas velocities of interest.

4.3.1.2 15.2 cm ID model cold-flow fluidized bed reactor

The second fluidized bed reactor used in this study has an inner diameter of 15.2 cm; other parameters are very similar to those of the smaller fluidized bed reactor. Figure 4.2 shows a schematic of the large FBR.

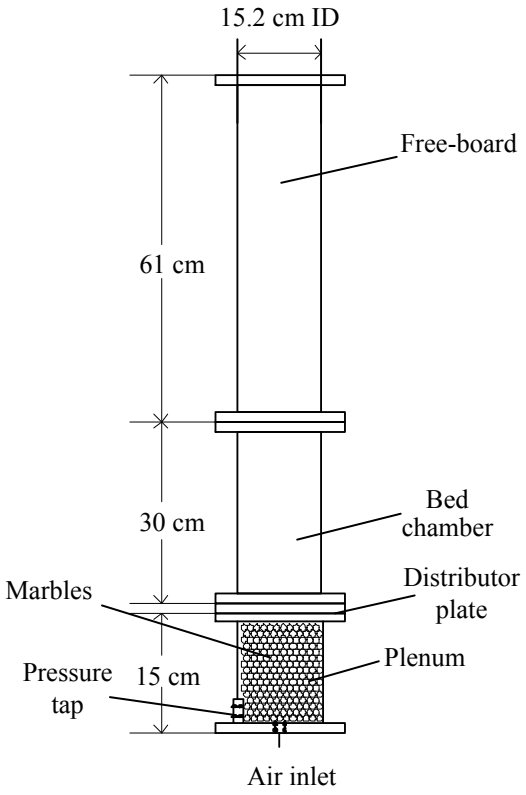

Figure 4.2: Large model fluidized bed reactor.

The air inlet is located at the bottom of the plenum, which is filled with marbles to evenly disperse the air over the bottom of the aeration plate. The aeration plate, mounted between the plenum and bed chamber, is made from stainless steel comprising 132, 1 mm diameter holes drilled in concentric circles, giving the aeration plate an open area ratio of 0.57%. To prevent particles from falling through the holes or plugging them, an American standard 45 mesh screen with openings of 0.04 cm is placed right above the distributor plate.

4.3.2 Material selection

The materials selected for this study cover a range of densities and particle sizes, are readily available, and mimic material that may be found in fluidized bed gasifiers. The inert bed material is often refractory sand because of its thermal properties and availability. For this study, glass beads (GB) have been selected as the inert bed material because they have very similar properties to that of sand, but are better characterized and more uniform in shape, which is beneficial for laboratory experiments.

The second granular material in the bed was ground corncob (GCC) or ground walnut shell (GWS). Both are very similar to the biomass particles typically used in gasifiers for biomass-to-fuel conversion. Close-ups of the GB, GCC, and GWS are shown in Figure 4.3. The photographs are taken with a magnification of factor of 10 and show particles in the range of 500-600 µm for each material.

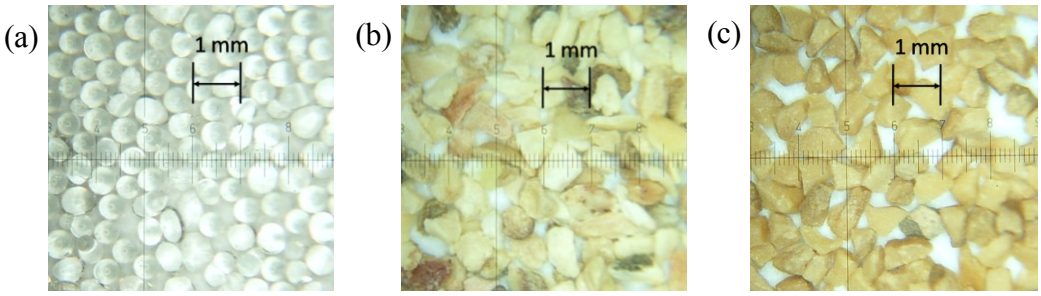

Figure 4.3: Close-ups of bed materials in the 500-600 µm particle size range, (a) GB, (b) GCC, and (c) GWS.

As shown in Figure 4.3a, the GB particles are smooth, solid, and almost spherical, and the particle size range appears to be fairly narrow. Figure 4.3b and 4.3c show that the GCC and GWS particles are not as smooth and round because they are a natural material and the manufacturing process is different; the GCC appear to be more “chunk-

like", "plate-like" or "stalk-like" whereas the GWS appear to be just "chunk-like" – it looks like gravel.

For all experiments, glass beads in the size range of 500-600 μm diameter are used as the inert bed material, while ground corncob or ground walnut shell in one of three size ranges (212-300 μm, 500-600 μm and 800-1000 μm) are selected as the second component. After sieving the particles multiple times with American standard sieves, it is assumed that the particles are normally distributed within the given size ranges. The particle size range and densities are listed in Table 4.1. Since this study focuses on the mixing and segregation of two granular type components, all particles are chosen so that they comply with Geldart type B for easy fluidization.

Table 4.1: Properties of bed materials.

Particle properties	Diameter [μm]	Individual particle density (average) [g/cm^3]	Individual particle mass [10^4 g]
Glass beads (GB)	500-600	2.60	1.70 - 2.90
Ground corncob (GCC)	212-300	1.00	0.05 - 0.14
	500-600		0.65 - 1.10
	800-1000		2.60 - 5.20
Ground walnut shell (GWS)	212-300	1.30	0.06 - 0.18
	500-600		0.85 - 1.50
	800-1000		3.50 - 6.80

4.3.3 Minimum fluidization and experimental conditions

The minimum fluidization velocity, U_{mf}, is one of the most important fundamental parameters related to fluidization hydrodynamics and is used to normalize flow conditions in this study. U_{mf} is experimentally determined for a bed of glass beads for

both model FBRs used in this study using the procedure outlined by Franka (2008) [16]; for this test, the bed was filled to a height of 1 column diameter with the 500-600 μm glass beads. On this basis, four different superficial gas velocities, relative to U_{mf}, have been applied to each bed as summarized in Table 4.2.

Table 4.2: Superficial gas velocity of experiments.

Minimum fluidization velocity of glass beads	9.5 cm ID bed	15.2 cm ID bed
$U_{mf,GB}$ [cm/s]	15.3	20.2
Superficial gas velocity applied [cm/s]		
1 x $U_{mf,GB}$	15.3	20.2
1.5 x $U_{mf,GB}$	23.0	30.3
2 x $U_{mf,GB}$	30.6	40.4
3 x $U_{mf,GB}$	45.9	60.6

Experiments have been conducted with varying particle size for the model biomass GCC and GWS particles. Each bed has a total static height of one column diameter (H/D = 1.0). Various volume ratios of model biomass to glass beads have been studied (25%/75%, 50%/50%, 75%/25%). To investigate the effect of initial condition, experiments have been conducted with model biomass on top of the GB, as illustrated in Figure 4.4 as a sample initial condition, as well as the other way around or with an initially well-mixed system.

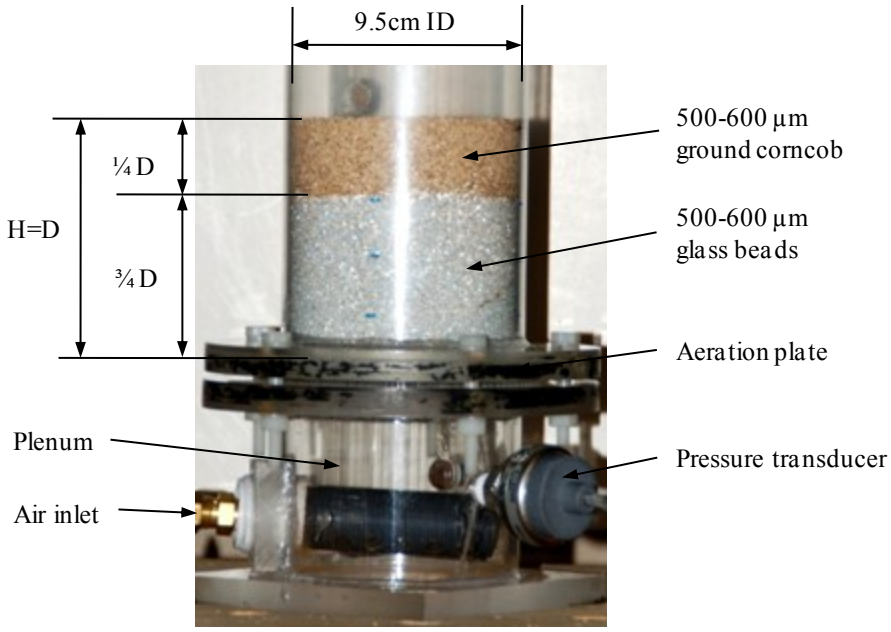

Figure 4.4: Sample initial condition with 500-600 µm glass beads (bottom material) and 500-600 µm ground corncob (top material) in the small FBR.

In addition to varying the model biomass particle size and superficial gas velocity, experiments were conducted with humidified air as well as with as-supplied compressed air (low humidity). It was assumed that the humidified air was nearly saturated and the as-supplied air was nearly dry, which, as shown below, has an impact on electrostatic charge build-up.

4.4 Results

Observations of the mixing and segregation results are recorded by means of still images of collapsed (fixed) fluidized beds. Multiple visualization tests at each condition have been completed and the results presented below are based on repeatable observations; hence, only selected still images are presented that represent typical results. The photographs have also been visually enhanced and modified for better illustration, and can therefore only be used for qualitative analysis. Several operating

parameters may influence bed segregation and mixing, including superficial gas velocity, biomass particle size and density, relative humidity of the gas stream, volume ratio of biomass to bed material, size of fluidized bed vessel, and initial bed conditions. The effects of these operating parameters are discussed below. The approximated level of the segregation interface has been marked by a red line in several images to assist in segregation and mixing assessment.

4.4.1 Effect of superficial gas velocity

Several tests have been performed to investigate the effect of superficial gas velocity on the mixing and segregation behavior of biomass. It has been found that higher fluidization gas velocities lead to better particle mixing. These tests were completed with 500-600 μm glass beads as the inert bed material and either 212-300 μm, 500-600 μm or 800-1000 μm ground corncob or ground walnut shell as the model biomass. Initial experiments were conducted with ground corncob as the model biomass and comprised 25% by volume of the bed for a total height of one column diameter in the small FBR; this model biomass was initially located on top of 75% by volume glass beads (Figure 4.4 shows a sample initial condition). The fluidizing gas was humidified. The reactor top was also covered with a screen to prevent particle elutriation at the higher superficial gas velocities. As the superficial gas velocity increased, the mixing rate generally increased, and this was observed for all material and initial conditions.

Figure 4.5 shows a time sequence of images from the initial condition to a long time in which the conditions do not change, where the fluidization time typically exceeds 5 minutes (identified as “Equilibrium”). The applied superficial gas velocity was $U_g = 2U_{mf}$ = 30.6 cm/s in the small FBR. For each image, the gas flow rate was abruptly stopped

by closing a ball valve and the bed was allowed to settle before the bed condition was recorded. The bed was then refluidized by slowly opening the ball valve (over a period of 2-3 seconds). The time period corresponds to the total fluidization time since the initial bed conditions (time equals 0 seconds in Figure 4.5).

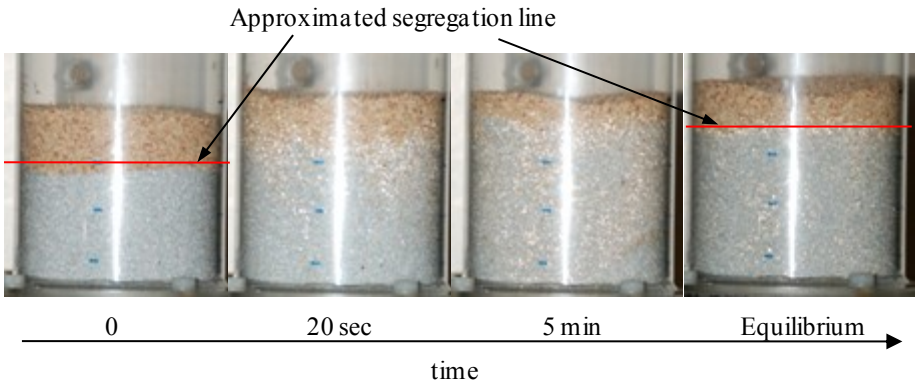

Figure 4.5: Mixing and segregation with $U_g = 2U_{mf} = 30.6$ cm/s; bed particles: 25% 800-1000 μm GCC initially on top of 75% 500-600 μm GB in the small FBR.

In general, approximately 10 to 20% of the ground corncob particles mix with the glass beads while the rest of the ground corncob remains segregated on top of the bed. This is demonstrated by the upward shift of the segregation line between fluidization times. The equilibrium condition changes depending on the superficial gas velocity. Lowering the superficial gas velocity enhances segregation, resulting in a condition that is closer to the initial condition. Increasing the superficial gas velocity, on the other hand, enhances particle mixing. For example, Figure 4.6 shows a time sequence for the same bed composition as in Figure 4.5 but with $U_g = 3U_{mf} = 45.9$ cm/s. As shown, increasing U_g increased the particle mixing and this effect was observed to be independent of particle size or other variables considered in this study.

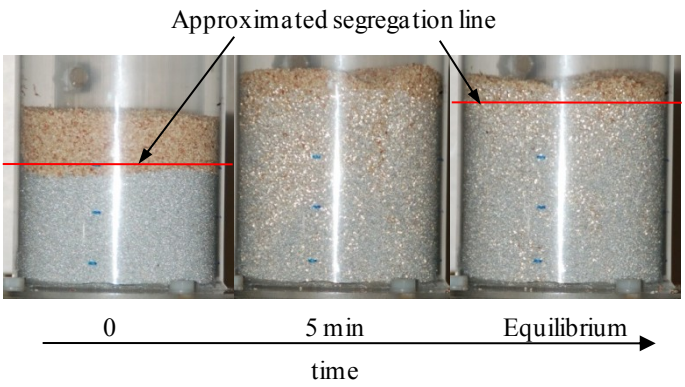

Figure 4.6: Mixing and segregation with $U_g = 3U_{mf} = 45.9$ cm/s; bed particles: 25% 800-1000 μm GCC initially on top of 75% 500-600 μm GB in the small FBR.

4.4.2 Effect of humidified gas stream

The effect of fluidization gas humidity was determined by performing experiments with and without humidifying the fluidization gas. The effects are illustrated with 500-600 μm ground corncob as the model biomass, fluidized with $U_g = 2U_{mf} = 30.6$ cm/s in the small FBR. The results show that a fluidization gas with a high humidity significantly lowers electrostatic charge buildup and promotes segregation. In contrast, fluidizing with low humidity or dry air yields a well-mixed bed, but one with also high electrostatic charge. Figure 4.7 shows the results from an experiment with 25% by volume of 500-600 μm corncob initially on the bottom and 75% by volume 500-600 μm glass beads on top when relatively dry compressed air is used to fluidize the bed. With time, more and more particles stick to the walls of the reactor due to electrostatic charge buildup. Also the bed materials appear to be well-mixed. From the initial condition, the bed completely turns over during the first 10 seconds of fluidizing, so that the ground corncob floats on top of the glass beads; it then becomes mixed in the bed, as shown in Figure 4.7.

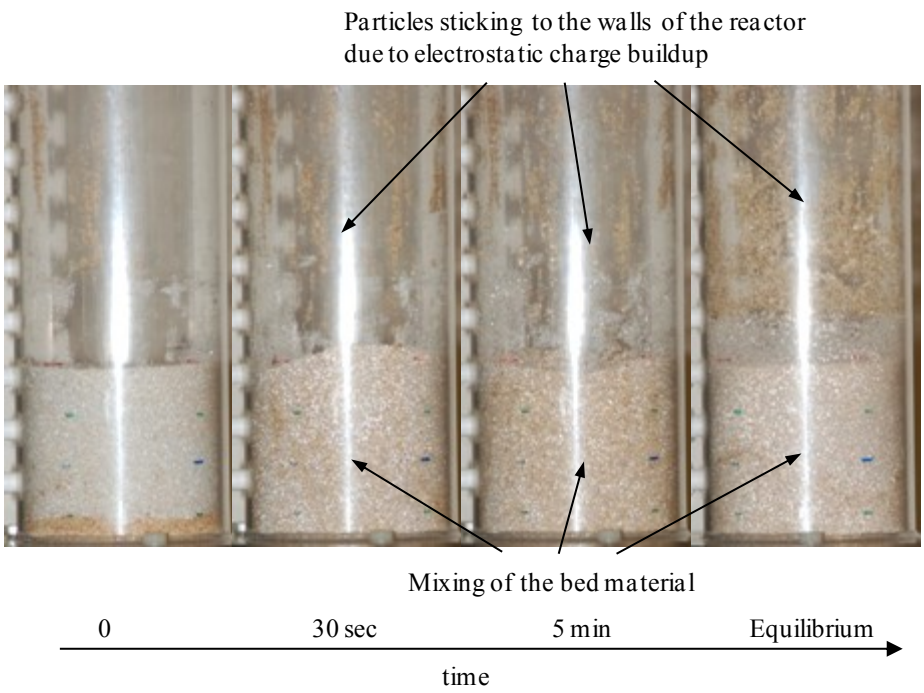

Figure 4.7: Particle mixing and segregation using unhumidified (dry) fluidization gas; $U_g = 2U_{mf}$ = 30.6 cm/s; bed particles: 25% 500-600 µm GCC initially on the bottom with 75% 500-600 µm GB on top in the small FBR.

In contrast, Figure 4.8 shows an experiment with similar bed composition but using a humidified gas stream and the ground corncob initially on top. Note that the change of colors in the pictures is due to improved camera settings (i.e., autoflash) during the experiment. Only a few particles stick to the reactor walls for this condition. Even more interesting, only a small amount of mixing is observed and the bed remains mostly segregated. Hence, a clear demarcation separates the two material phases. This trend was observed for all particle sizes and superficial gas velocities considered in this study. When the ground corncob was initially on the bottom in a well humidified gas stream, the bed completely turned over in about 10 seconds and then remained segregated.

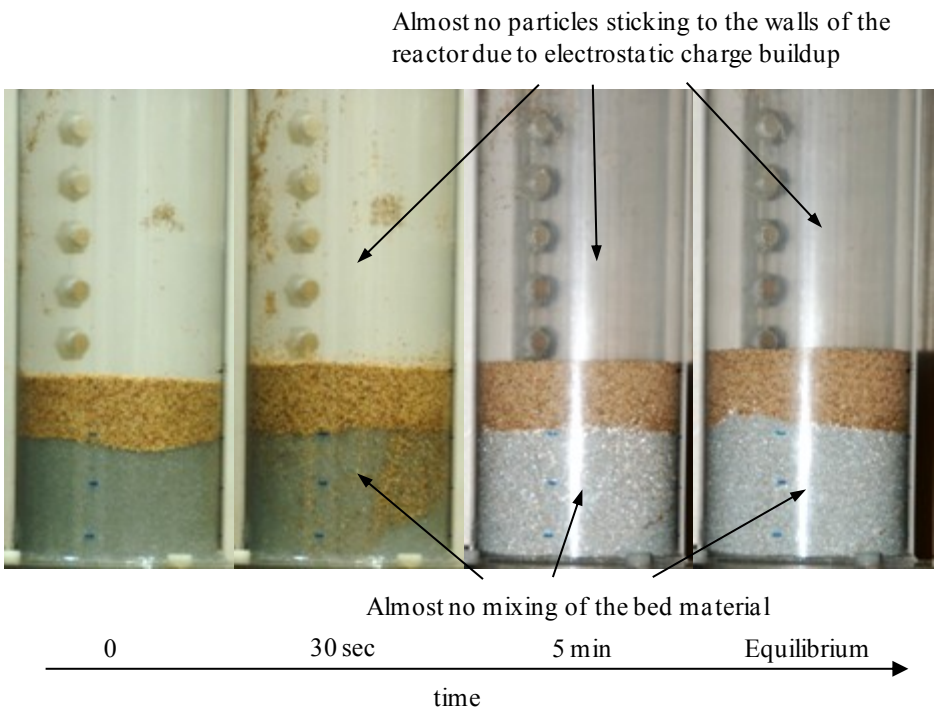

Figure 4.8: Particle mixing and segregation using humidified fluidization gas; U_g = $2U_{mf}$ = 30.6 cm/s; bed particles: 25% 500-600 µm GCC initially on the bottom with 75% 500-600 µm GB on top in the small FBR.

Guardiola et al. (1996) [100] noted that there exists a complex connection between the relative humidity of the fluidizing gas and the quality of fluidization in terms of bubbling and slugging. This effect was observed in the above experiments as well and resulting in the observed change in mixing quality.

4.4.3 Effects of biomass particle size

To demonstrate the effect of biomass particle size, a series of experiments have been completed with an initially well-mixed bed composition. In general, the smaller biomass particles typically segregate sooner than larger biomass particles. Also, the amount of segregated biomass varied with particle size. This coincides with earlier research work such as Huilin et al. (2003) [44] and Wu and Baeyens (1998) [47]. The smaller biomass particles seemed to segregate almost completely, whereas a

significant fraction of the larger biomass particles remained mixed with the inert bed material. To illustrate these results the following shows images from experiments with 25% by volume GCC particles in three different size ranges (212-300 μm, 500-600 μm and 800-1000 μm) initially well-mixed with 75% by volume 500-600 μm GB in the small FBR. The bed was then fluidized at $U_g = 2U_{mf} = 30.6$ cm/s and images of a collapsed bed were recorded at selected time intervals. Also, as shown above, humidification promotes particle segregation, therefore the fluidizing gas was equally humidified for all experiments. The results are illustrated in Figures 4.9-4.11. Since the amount of segregation for the different biomass particle sizes varied, an approximated segregation line is provided to indicate the interface between the phases at the equilibrium condition; a rough estimate (in percentage) of how much biomass is segregated out is also provided in the figures.

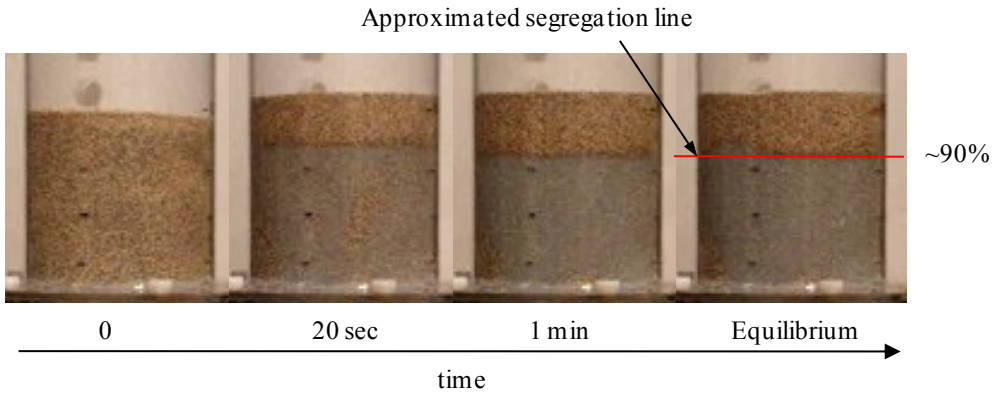

Figure 4.9: Particle segregation using 200-300 μm ground corncob in the small FBR.

Figure 4.9 shows that with very small biomass particles (212-300 μm), almost all the GCC segregates from the GB. More than half of the material accumulates on top of the glass beads after only 20 seconds. It is estimated that only about 10% of the biomass remains mixed with the bed material at equilibrium (~5 minutes). With 500-600 μm

biomass particles, the biomass does not segregate as fast. As shown in Figure 4.10, after 20 seconds only 40 – 50% of the material is floating on top of the glass beads. Approximately 15 – 20% of the biomass also remains mixed with the glass beads at equilibrium (~7 minutes). With very large biomass particles (800-1000 μm), the biomass segregates out very slowly. Figure 4.11 shows that only a small portion is floating on top of the glass beads after 20 seconds. Also, the biomass does not segregate uniformly and accumulates in bed pockets while other locations show very low biomass content (see Figure 4.11 after 20 sec). In equilibrium (~9 minutes) an estimated 40% of the biomass remains mixed.

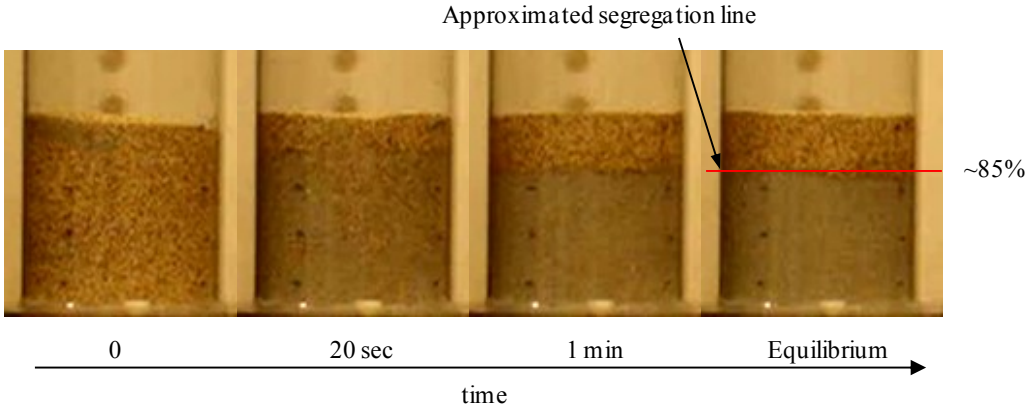

Figure 4.10: Particle segregation using 500-600 μm ground corncob in the small FBR.

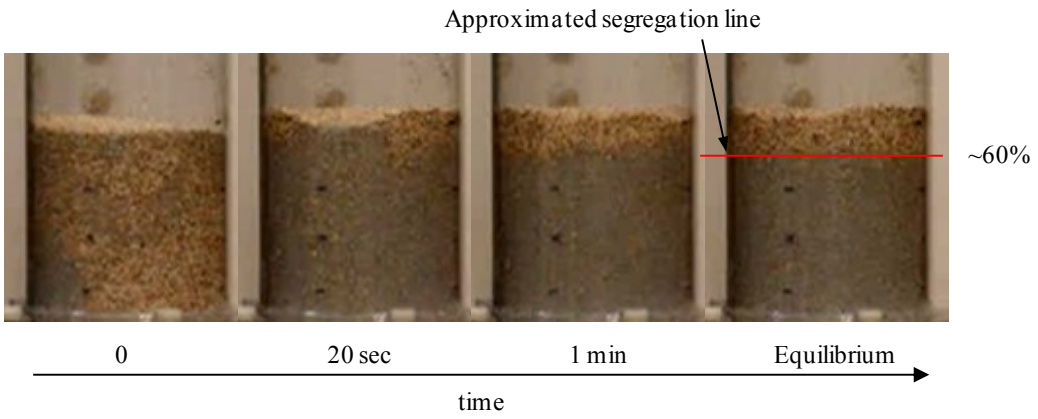

Figure 4.11: Particle segregation using 800-1000 μm ground corncob.

Figures 4.9-4.11 show that the less dense material, i.e. biomass, segregates from the glass beads and floats on top of the bed. Even the largest biomass particles, which have a mass larger than the individual glass beads, rise to the surface when the fluidizing gas is humidified (see particle mass in Table 4.1).

4.4.4 Effect of different particle species/density

The different trends based on superficial gas velocity, particle size, and humidified gas stream that have been observed using GCC as the model biomass, were also observed with GWS as the model biomass. There was a significant difference in the amount of segregation of GCC compared to GWS for all trends. The difference in species and thereby the difference in particle density of the model biomass appears to have a noticeable effect on the mixing and segregation behavior of the fluidized bed.

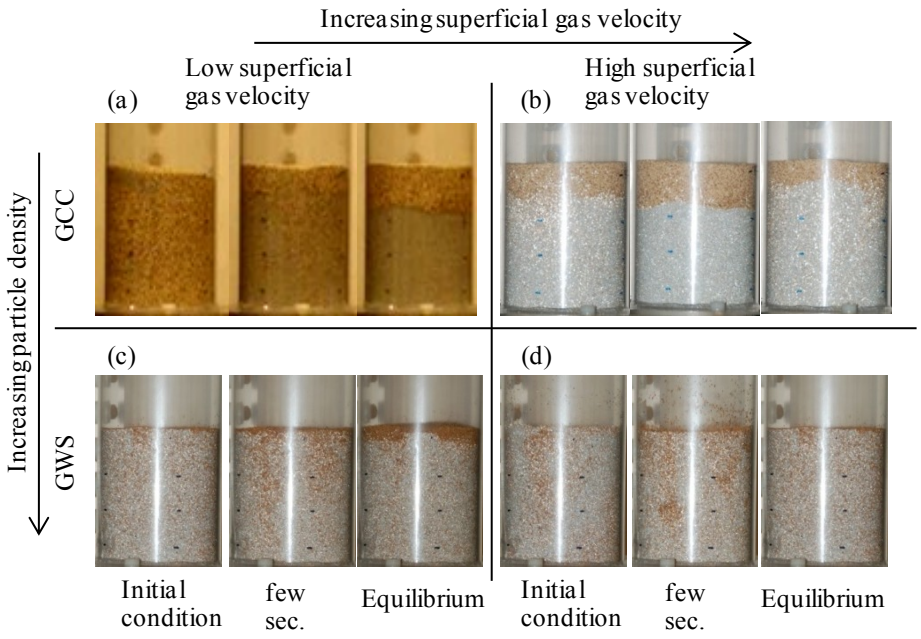

Figure 4.12: Photographs of experiments using the 9.5 cm ID model FBR with: (a) 25% 500-600 µm GCC fluidized at $U_g = 2U_{mf}$, (b) 25% 500-600 µm GCC fluidized at $U_g = 3U_{mf}$, (c) 25% 500-600 µm GWS fluidized at $U_g = 1.5U_{mf}$, and (d) 25% 500-600 µm GWS fluidized at $U_g = 2U_{mf}$, to illustrate the effect of particle species (particle density).

Figure 4.12 shows examples of different mixtures of GCC or GWS mixed with GB. Although the experimental conditions do not exactly match, it is evident that both model biomass types show similar behavior, i.e. the model biomass segregates at lower superficial gas velocities and mixes at higher superficial gas velocities. Also demonstrated in Figure 4.12 is the difference in the extent of segregation for the two different types of materials. Even though the lower superficial gas velocity for the GCC is $U_g = 2U_{mf}$ (Figure 4.12a) and therefore higher than the one for GWS, $U_g = 1.5U_{mf}$ (Figure 4.12c), the amount of segregation of the GCC is higher, which is the opposite of what would have been expected based on the superficial gas velocity. Also, Figure 4.12a and Figure 4.12d show segregation of GCC and GWS, respectively, for the same

superficial gas velocity of $U_g = 2U_{mf}$. In this case GCC segregated almost completely, while GWS appears to be in a fairly well-mixed stage.

As has been shown in the past [93, 101], this may be mostly attributed to the lower density of the GCC particles compared to the GWS particles. However, as explained earlier and shown in Figure 4.3, there is also a significant difference in the shape of the particles, with the GWS being more spherical while the GCC appears to be more “chunk-like”, “plate-like” or “stalk-like”. Also, during the data acquisition phase it was observed that the GCC appears to be much more affected by electrostatic charge buildup than the GWS. Since both these effects have not been studied extensively, it is not possible at this point to conclude whether or not these factors also influence the amount of segregation, and if so, to what level.

4.4.5 Reactor diameter effects

Experiments have also been completed to determine the effect of fluidized bed diameter on the mixing/segregation. The following illustrates results from experiments with GWS as the model biomass in three different particle size ranges (212-300 μm, 500-600 μm, 800-1000 μm) mixed with 500-600 μm GB as the inert bed material for the two different model reactors, the 9.5 cm ID FBR and the 15.2 cm ID FBR.

It was found that the GWS and GB mix significantly better in the larger vessel and that this effect occurs for all studied conditions. Figure 4.13 shows an example of this effect. There is basically not much difference between Figure 4.13c and Figure 4.13d, which are the photographs of the larger vessel for low and high superficial gas velocities. What appears to be segregated material in the upper region of the bed of

Figure 4.13d was only a thin layer of GWS sticking to the walls of the FBR due to electrostatic charge buildup. In Figure 4.13a, mixing in the smaller fluidized bed vessel shows that there is a significant amount of segregated GWS floating at the top. Based on these observations, it is concluded that it is easier to mix materials in a larger vessel.

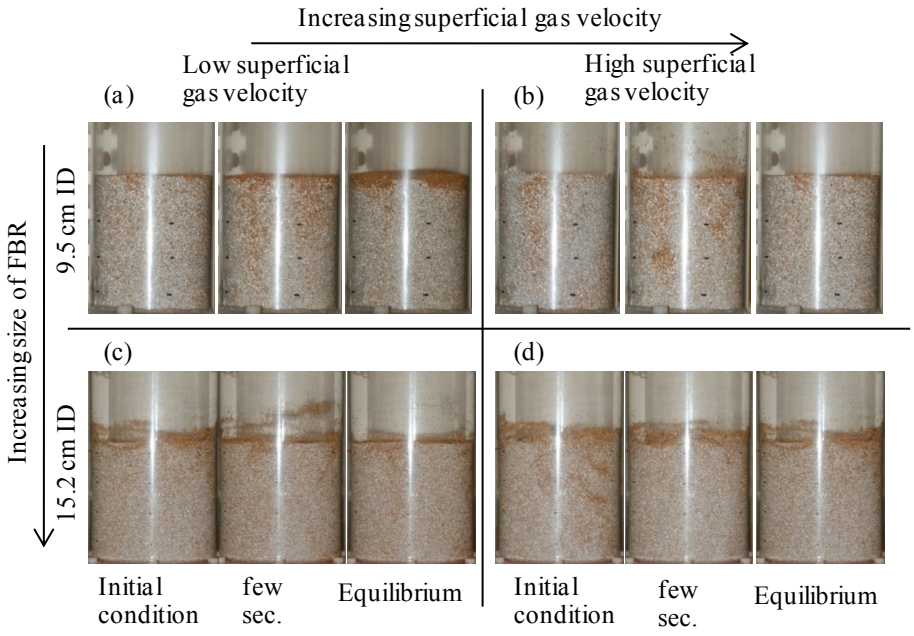

Figure 4.13: Photographs of experiments with 25% 500-600 μm GWS mixed with 75% 500-600 μm GB and fluidized at: (a) $U_g = 1.5U_{mf}$ in the 9.5 cm ID FBR, (b) $U_g = 2U_{mf}$ in the 9.5 cm ID FBR, (c) $U_g = 1.5U_{mf}$ in the 15.2 cm ID FBR, and (d) $U_g = 2U_{mf}$ in the 15.2 cm ID FBR, to illustrate the bed diameter effect. The bed materials are initially well-mixed.

4.4.6 Effect of initial conditions

Experiments have been completed with a variety of initial conditions of the particles in the bed; i.e., material A on top of material B, the other way around or an initially well-mixed bed. For all variables considered in this study, it was found that the initial condition did not have any significant impact on the equilibrium condition of the bed or on the time to reach that stage.

4.5 Conclusions

Mixing and segregation were observed in two-component cold-flow fluidized beds over a variety of test conditions. Mixing was enhanced as the superficial gas velocity increased. At superficial gas velocities at or just above the minimum fluidization velocity, the lower density particles (biomass) segregate. Humidifying the gas stream showed a significant effect on the electrostatic charge buildup as well as on the mixing of the biomass with the inert bed material. High humidity in the gas stream lowered the electrostatic charge buildup of the particles and promoted segregation of the biomass. The biomass particle size influenced the amount of biomass segregation as well as the segregation time. Smaller biomass particles segregated faster than larger ones. Smaller biomass particles also tended to segregate more evenly and leave fewer particles mixed with the inert bed material.

For the two different types of biomass particles considered in this study, GCC and GWS, the experiments showed that the lighter biomass particles (GCC) segregated more for all other conditions the same. The size of the fluidized bed vessel showed some effect on the mixing behavior of the bed particles. With comparable reactor designs, the particles mixed better in the larger fluidized bed vessel. For the conditions considered in the scope of this study, it appeared that the initial configuration of the particles in the bed did not have a significant impact on the equilibrium mixing condition or the fluidizing time to reach that stage.

Overall, these experiments were based on visual observations that only showed the outer surface of the bed. Therefore the observations are qualitative in nature and only

allow limited conclusions. Future work will use a unique, non-invasive X-ray computed tomography technique [18, 19] to provide more revealing information about the mixing mechanisms of biomass in fluidized bed reactors. This will give detailed information about the internal structure of the fluidized bed and thus also allow for a quantitative mixing and segregation analysis.

4.6 Acknowledgements

Support for portions of the work described in this paper from ConocoPhillips Company is acknowledged.

Chapter 5 Quantifying Mixing in 3D Multi-Component Particulate Systems[2]

5.1 Abstract

Particulate systems are fundamental to fluidized beds and the quality of mixing is key to their performance. To evaluate the quality of mixedness of particles in a fluidized bed, either through experiments or with CFD simulations, and to further compare various operating parameters, proper quantification methods are necessary. Two analysis tools are presented here that allow for quantitative assessment of the mixedness of a multi-component particulate system; they are a newly-defined Particle Segregation Number (PSN) and the Cube Analysis (CA). The study has been conducted using artificially created material distributions simulating a collapsed 3D cylindrical fluidized bed vessel. Particle distribution is denoted in terms of volume concentration per voxel (i.e., a 3D pixel). The results show that the PSN and CA measures are independent of particle size, material densities, or other fluidized bed parameters, which is not true for other available segregation measures, and can therefore be used over a wide range of operating conditions. Furthermore, it was found that using these methods allows for capturing even small changes in the overall bed segregation condition.

Keywords: biomass processing, fluidized bed, hydrodynamics, mixing, mixing quantification methods, segregation

[2]Based on: Keller, N.K.G., Bai, W., Fox, R.O., Heindel, T.J., 2012. Quantifying Mixing in 3D Multi-Component Particulate Systems. Chemical Engineering Science, under review.

5.2 Introduction

Fluidized bed reactors are used in many industrial processes such as drying, coating, and gasification. They offer many operating advantages such as efficient mixing properties, low pressure drop and high heat and mass transfer rates. Over the past three decades, a variety of research studies have been completed to assess efficient and economical operation of a fluidized bed, and to find fundamental connections between various operating parameters such as particle size and density, superficial gas velocity, bed dimensions, etc. [4, 44-46, 62, 63, 66, 77, 84, 93, 95-98, 102, 103]. One key parameter of fluidized bed operation, and an important aspect of research, is the quality of particle and fluid mixing inside the bed. It is particularly important to have proper analysis tools that describe the stage of particle mixedness in the bed when model validation studies are completed. One of the earliest introduced measures for the level of mixedness is the Mixing Index [66], which is an easy to use and convenient way to quantify particle mixedness. Another study introduced the Segregation Rate [2]. While both measures are a convenient way to quantify particle mixing in a fluidized bed, they can produce values outside a commonly acceptable range of 0-1, and the maximum value is a function of particle density and bed mixture volume or mass ratio. This makes it challenging when comparing mixing levels for different operating conditions.

This paper introduces two analysis tools that allow for quantification of mixing and segregation in particulate systems composed of two different particle types. The theory of the analysis tools is explained and examples are presented using artificially created, three dimensional particulate systems with varying mixture ratios by volume. These

particulate systems simulate collapsed fluidized beds (e.g., frozen beds). It is also shown that the mixing index is not sensitive enough to capture small variations in the particle mixing quality in the bed.

5.3 Procedures

5.3.1 Existing quality of mixedness measures

Two existing measures to quantify mixing of particles in a fluidized bed are the Mixing Index (MI) [66] and the Segregation Rate (SR) [2].

The mixing index is calculated on the basis of mass fractions of jetsam particles. It compares the mass fraction of jetsam particles found in the upper region of the bed with the overall mass fraction of jetsam particles in the whole bed. It assumes that the jetsam particles are evenly distributed in the upper region. Hence, the mixing index is calculated as:

$$\mathrm{MI} = \frac{x_U}{x_T} * 100\% \tag{5.1}$$

where x_U is the mass fraction of jetsam particles in the upper region of the bed and x_T is the overall mass fraction of jetsam particles in the bed. For MI = 0 the bed is completely segregated about a horizontal plane and for MI = 100% the bed is perfectly mixed. The restrictions for the mixing index are illustrated in Figure 5.1, namely the assumption of an even distribution of jetsam in the upper region of the bed, as illustrated in Figure 5.1b.

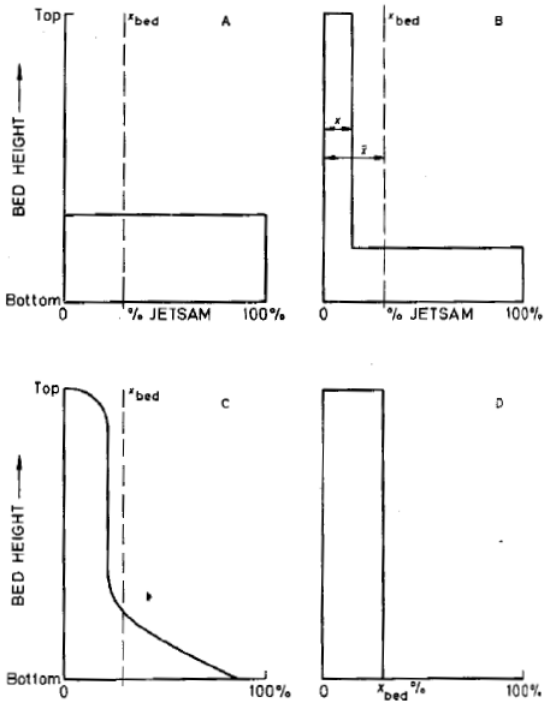

Figure 5.1: Mixing index for idealized segregation patterns [66]. (a) Complete horizontal segregation, (b) idealized segregation for low superficial gas velocities, (c) idealized segregation for high superficial gas velocities, and (d) perfectly mixed.

Similar to the PSN, the segregation rate [2] is calculated on the basis of average heights above the distributor of flotsam and jetsam particles. The calculation is as follows:

$$SR = \frac{S\text{-}1}{S_{max}\text{-}1} * 100\% \tag{5.2}$$

where S is the ratio of average heights of small to large particles, calculated as:

$$S = \frac{h_{small}}{h_{large}} \tag{5.3}$$

where h_{small} is the average height above the distributor of small particles, and h_{large} is the average height above the distributor of large particles. S_{max} contains the

maximum degree of segregation and is calculated in terms of the mixture composition as:

$$S_{max} = \frac{2\text{-}x_{small}}{1\text{-}x_{small}} \tag{5.4}$$

where x_{small} is the mass fraction of small particles. The measure SR represents a bed that is perfectly mixed at SR = 0 and completely segregated for SR = 100%.

The segregation rate was introduced by [2] as part of a work studying segregation of binary mixtures in a pseudo two-dimensional fluidized bed. The beds were composed of equi-density particles and the measure can only be applied to such. Nevertheless, because the images analyzed in this paper are artificial and denote volume fractions, the segregation rate has been included for completeness.

Since both the PSN and the SR show good mixing for 0% and complete segregation for 100%, and to aid in the understanding of the differences of the measures, the mixing index is used as its inverse. Therefore a new measure MI* is introduced, which is simply MI* = 1-MI, to make the mixing index range more compatible with the PSN and SR.

5.3.2 Particle Segregation Number (PSN)

To illustrate time resolved segregation data and the ability to compare particulate systems such as fluidized beds over a wide range of operating parameters, it is necessary to have an analysis tool that would represent any particular particle configuration inside the bed in terms of its “mixedness” as a single number and still be sensitive enough to small variations. Both the Mixing Index [66] and the Segregation Rate [2] offer this convenience. However, it was found that both approaches have

limitations when applied to systems that have varying particle densities and/or mixture volume ratios. Therefore the “Particle Segregation Number” (PSN) has been developed. It is calculated on the basis of the normalized average heights of the heavier material (jetsam) and the lighter material (flotsam). Thus, the particle segregation number is defined as:

$$PSN = 2^* \left[\frac{\overline{h_F}}{H} - \frac{\overline{h_J}}{H} \right] * 100\% \tag{5.5}$$

where H denotes the total static bed height. The parameters $\overline{h_F}$ and $\overline{h_J}$ denote the average heights above the distributor of flotsam and jetsam particles, respectively, and are calculated as:

$$\overline{h_F} = \frac{\sum h_{F,i,j}}{N_F} \tag{5.6}$$

$$\overline{h_J} = \frac{\sum h_{J,i,j}}{N_J} \tag{5.7}$$

where $h_{F,i,j}$ and $h_{J,i,j}$ are the height of individual flotsam and jetsam voxels, respectively, and N_F and N_J are the total number of voxels attributed to flotsam or jetsam content in a binary image. The binary image is obtained by converting the concentration image through an iterative process to maintain the overall flotsam content in the region of interest, thus identifying each voxel as either flotsam or jetsam. It was found that, independent of the material volume ratio, the difference in normalized average bed heights for a completely segregated bed will always be 0.5, while for a perfectly mixed bed the difference will always be 0. Hence, the factor of 2 in Eqn. (5.5) results in the PSN describing any bed condition between 0 and 100%. If PSN = 0, the

bed is ideally mixed; for PSN = 100%, the bed is completely segregated. This is a simple and convenient way to express the condition of any particulate system in terms of the level of “mixedness”.

5.3.3 Cube Analysis (CA)

Because the PSN represents the mixedness of any bed in one single number, it cannot identify if a two-component particulate system has developed pockets of high concentration of one or the other component, which is imaginable because it cannot be excluded based on existing knowledge about mixtures of particulate systems. Also, as will be shown later, to express the mixedness in one single number, a lot of information is ignored and can potentially lead to a false conclusion about the condition of the bed. Therefore, a second quantification method has been utilized to help understand concentration profiles within a two-component particulate system with respect to the formation of high concentration pockets; we term this the “cube analysis” (CA) [104].

The CA algorithm calculates the average concentration of neighboring voxels for all cubes with the side length a_C within the bed region. This analysis is done for cubes with varying side length, from $a_C = 1$, for one voxel per cube only, up to a maximum of n voxels per side length. The results are then sorted and displayed in a histogram. If the particulate system contains pockets of high concentration, it would be visible in the histogram by a peak for cubes with a certain side length. This will also indicate the size of the pocket. The CA is then used as an additional tool for any one-number representation of particulate mixedness and to verify the condition.

5.3.4 Artificial bed images

To demonstrate the performance of the different analysis tools, the calculations have been embedded in algorithms and applied to a variety of particulate systems that simulate collapsed fluidized beds with known segregation conditions. The data that are used for these sample calculations represent 3D images of particulate systems with a cylindrical cross section, but could be applied to any binary particulate system where two distinct particles can be identified. For ease of illustration, only the center slice out of those 3D images will be presented in this paper. Because of an ongoing experimental evaluation of particle mixing in a model fluidized bed reactor using X-ray computed tomography scans [105], the artificial images are created so that the simulated collapsed bed reflects those found in the experiment.

To prove the usefulness of the PSN and CA and to demonstrate their superiority above the MI and SR when applied to two-component particulate systems, a variety of fluidized bed images have been created. The first set corresponds to beds with a very distinct segregation pattern. Figure 5.2 shows the center slice through the three-dimensional images. The beds are perfectly separated in three variations, horizontally, angled and along a vertical axis, and all have a mixture ratio of 50% by volume of jetsam and flotsam. Hence, the white regions are 100% flotsam while the black regions contain 0% flotsam.

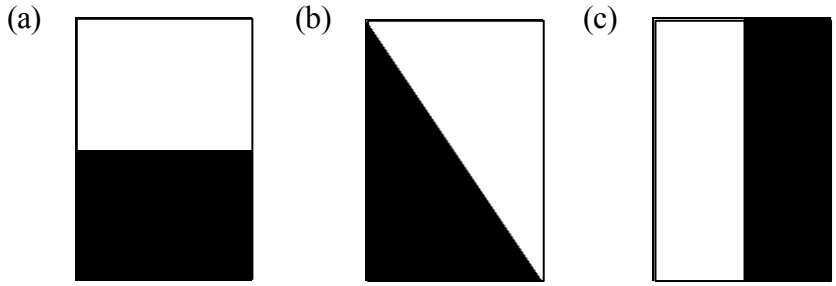

Figure 5.2: Cross-sectional image of artificial beds with 50/50 mixture volume ratio, segregated (a) along horizontal axis, (b) angled, and (c) along vertical axis.

The second set of simulated images to compare the quantification methods is created with clusters of high concentration of the flotsam in the particulate system by randomly distributing spherical clusters throughout the bed region. Material is distributed so that the overall content is 25%, 50% or 75% by volume flotsam. To provide a more realistic approach, the beds also have a background noise of 10% flotsam on average, with a maximum of 20%. The clusters represent flotsam contents between 80% and 100%, with an average of 90%. All percentages refer to the content by volume of flotsam and hence imply that the surplus is balanced by jetsam. For example, a voxel or larger region showing 20% flotsam implies that there is also 80% jetsam in that region. To simulate segregating beds, a series of beds have been created in which the cluster size and location are varied. To change the cluster size, a series has been created in which the cluster diameter increases in steps of ten, starting with a diameter of 20 voxels up to a diameter of 60 voxels. The location is influenced by changing the average height of the clusters from H/D = 0.5to H/D = 0.85. The average radial location is also varied from r/R = 0.5 to r/R = 0.85. Figure 5.3 illustrates a center slice (x-slice) of a bed with 25% by volume of flotsam with 20 voxel diameter clusters with an average cluster height and radial location of H/D =0.65 and r/R = 0.75, respectively. The images

are then analyzed using the above explained methods and the results are presented below.

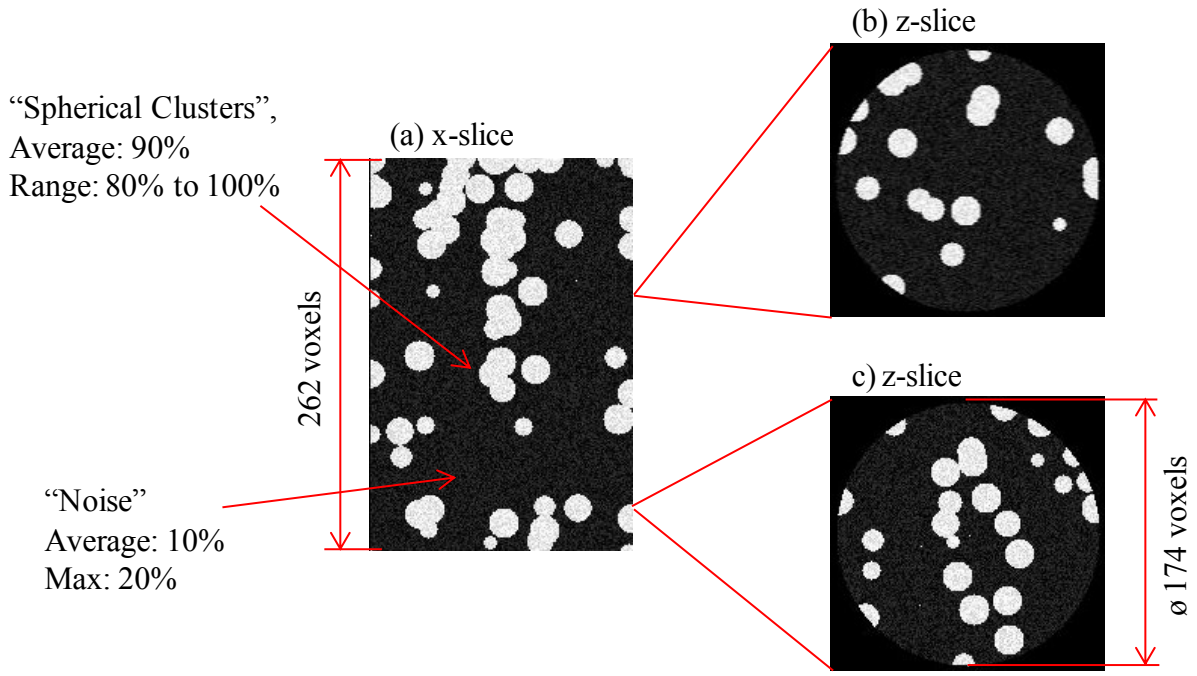

Figure 5.3: Sample image for clustered images with 25% by volume flotsam, cluster diameter = 20 voxels, and average height and radial location of H/D = 0.65 and r/R = 0.75, respectively, for (a) vertical center slice, (b) and (c) vertical cross-sections at random locations as indicated.

5.4 Results and discussion

The two analysis tools, PSN and CA, are discussed and compared to existing measures, using a variety of artificially created material distributions of a cylindrical two-component particulate system. The simulated collapsed fluidized beds represent particle compositions of three different mixture volume ratios (25/75, 50/50 and 75/25 by volume) and two different types of particles, referred to as jetsam and flotsam.

5.4.1 Comparing PSN and MI

To represent the mixedness of any two-component particulate system in one single number, but yet still be able to distinguish between different conditions, even if the variation in material distribution is small, requires a sensitive analysis tool. Applying the MI* to three dimensional images as explained above, it was found that even though the trend of segregating material towards the top and with increasing cluster size existed, the MI* only registered small variations. To illustrate this effect, the MI* and the PSN have been applied to a series of images that represent systems containing spherical clusters with increasing diameter and clusters that have been placed with a probability shifting towards the top of the bed. All beds have a background noise of 10% flotsam on average with a maximum of 20%, the clusters have flotsam content with a minimum of 80% by volume and an average of 90%. The average heights above the distributor of the spherical clusters for the corresponding conditions are listed in Table 5.1, and the average radial position of the clusters is r/R = 0.75 for all conditions. Figure 5.4 shows the center slice of each of these conditions. Note that the actual image is three-dimensional and the total number of clusters visible in any one slice can vary from one condition to the next. Also, the different diameter clusters shown in Figure 5.4 result from the slice plane cutting through an off-center cluster of the given diameter.

Table 5.1: Bed conditions.

Condition	A	B	C	D
Average height of clusters above distributor [H/D]	0.5	0.65	0.75	0.85

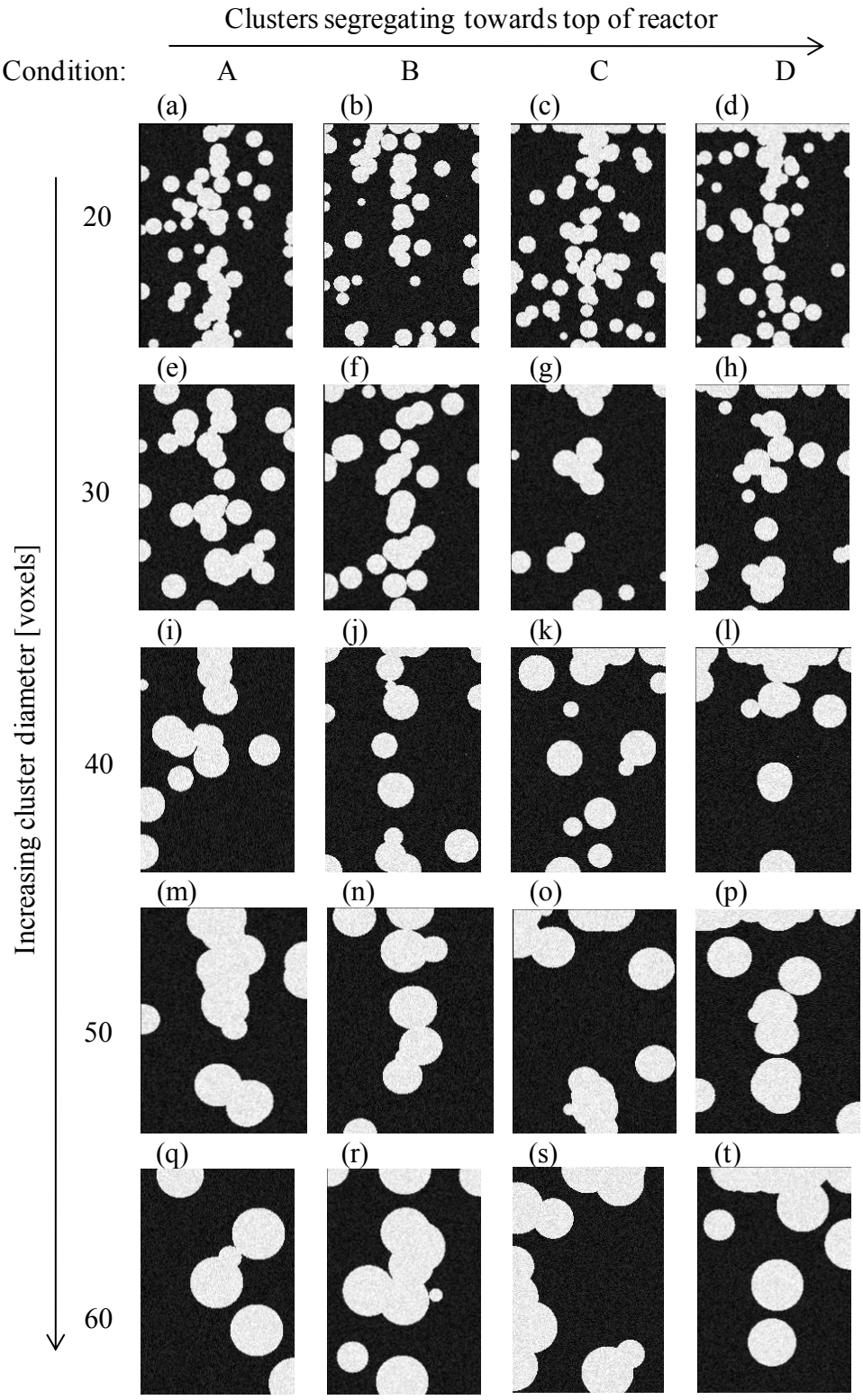

Figure 5.4: Sample series of images showing center slice through 3D images with 25% by volume flotsam, and radial location of r/R = 0.75.

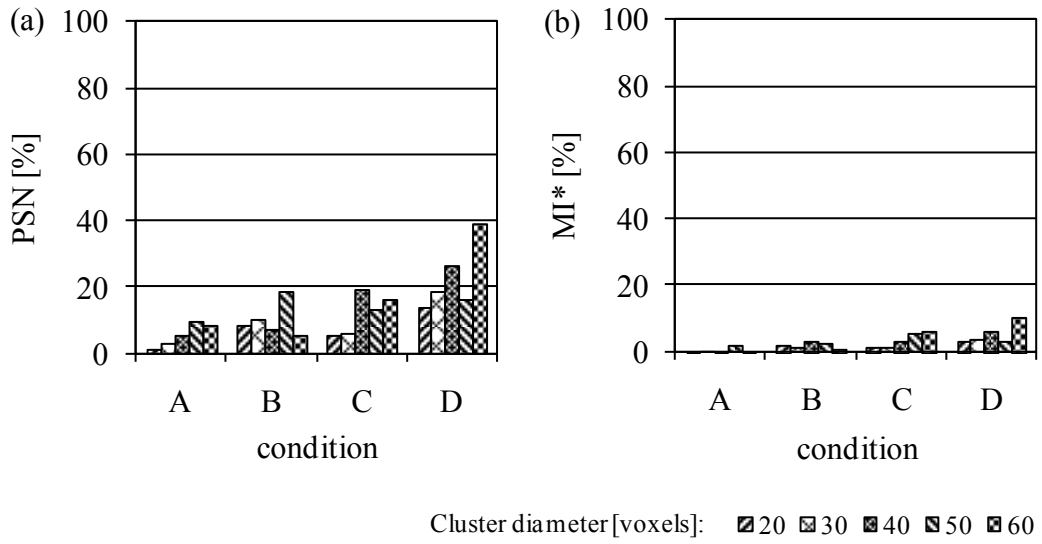

Figure 5.5: PSN and MI* showing results for artificial beds with 25% by volume flotsam, 75% by volume jetsam bed material for different conditions.

As Figure 5.5 demonstrates, the PSN better reflects the differences in bed mixing quality, because on the same scale, the results are more dispersed, acknowledging the fact that there are indeed differences in the material distributions. From condition A to condition D, it is expected that the quantification tool should register increased segregation because the clusters of particles are placed more and more towards the top of the bed. Both the PSN and MI* do reflect this, but the PSN classifies the beds as more segregated than the MI*. For example, condition D has cluster diameters of 60 voxels, the PSN shows that the bed is 40% segregated, while the MI* still shows good mixing with a segregation measure of 10%. With increasing cluster diameter for each condition, the beds also trend towards more segregated conditions. Both measures reflect this trend, but again the MI* shows minimal change in the overall bed condition and also segregation measures that suggest the beds are fairly well-mixed.

Another example to demonstrate the higher sensitivity to changes in the bed composition is illustrated in Figure 5.6, which shows the results for beds with varying mixture volume ratio. All beds have a background noise of 10% on average flotsam with a maximum of 20% and the clusters are again on average 90% flotsam with a minimum of 80%. The average height of the clusters above the bed base is H/D = 0.85, the average radial position of the clusters is r/R = 0.75 and constant for all mixture ratios. Again, the PSN shows that it better differentiates between the various bed conditions than the MI*. Distributing the flotsam in the bed through clusters as described leads to a better material distribution or better mixedness (lower PSN or MI*) as the mixture volume ratio increases. The PSN shows that at a low flotsam volume content the beds are segregated up to 40% and the mixing quality increases as the mixture volume ratio increases. The MI* reflects a similar trend, but the maximum mixing percentage is only about 10% for all conditions.

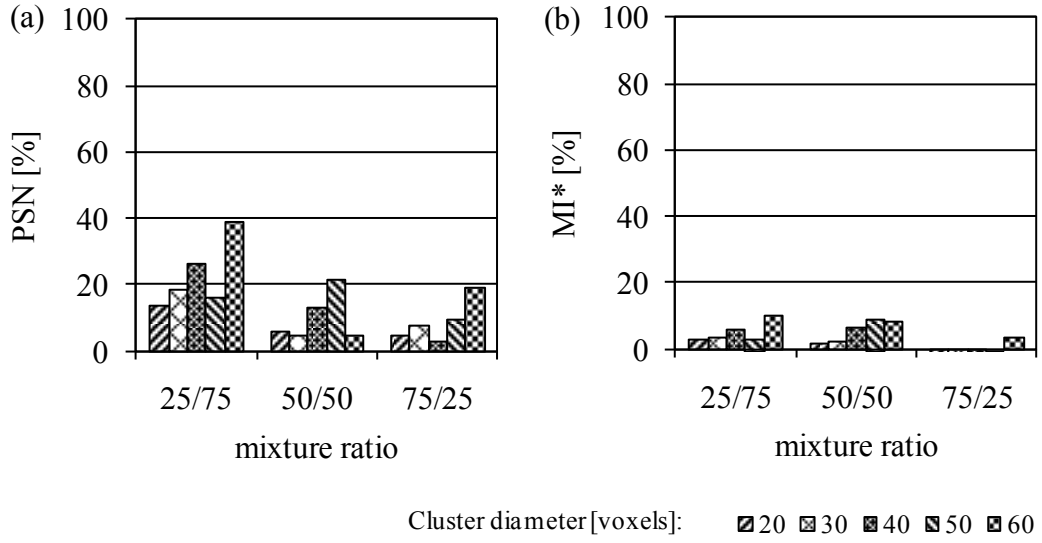

Figure 5.6: PSN and MI* showing results for the artificial beds with varying mixture ratio.

5.4.2 Comparing PSN and SR

Since the PSN and SR are both calculated based on the average heights above the distributor of flotsam and jetsam material, they show similar values and sensitivity when applied to a series of images as done in the previous section. However, the SR measure is based on flotsam mass fractions and thus, limits its usefulness to equi-density systems. The artificial images produced for this study are in the style of real images acquired with X-ray computed tomography of multi-component collapsed fluidized beds that are not equi-density systems. The flotsam and jetsam particles simulated in this study represent ground walnut shell (GWS) as flotsam material with a particle density of ρ_{GWS} = 1.3 g/cm^3 and glass beads (GB) as jetsam material with a particle density of ρ_{GB} = 2.6 g/cm^3. To illustrate the outcome of the SR on non equi-density systems, Figure 5.7 compares the PSN and SR using a series of images with the above mentioned condition representing beds with distinct segregation profiles, i.e., horizontally segregated, angled, and vertically segregated. Assuming optimal packing densities, the bulk densities of flotsam and jetsam were experimentally determined for GWS as the flotsam and GB as the jetsam and are $\rho_{flotsam}$ = 0.66 g/cm^3 and ρ_{jetsam} = 1.55 g/cm^3. For the angled and vertical particulate systems, both methods give very similar results. However, for the horizontally segregated bed, representing a particulate system in which all flotsam material has segregated out to the top leaving pure jetsam on the bottom, the calculation for the SR results in a value far above 100%. It was determined that the SR actually only comes out to be 100% for a fully segregated bed when all the particles have the same density. Since many experimental conditions will

include particles with different densities, the SR was found not to be a sufficient measure of mixedness.

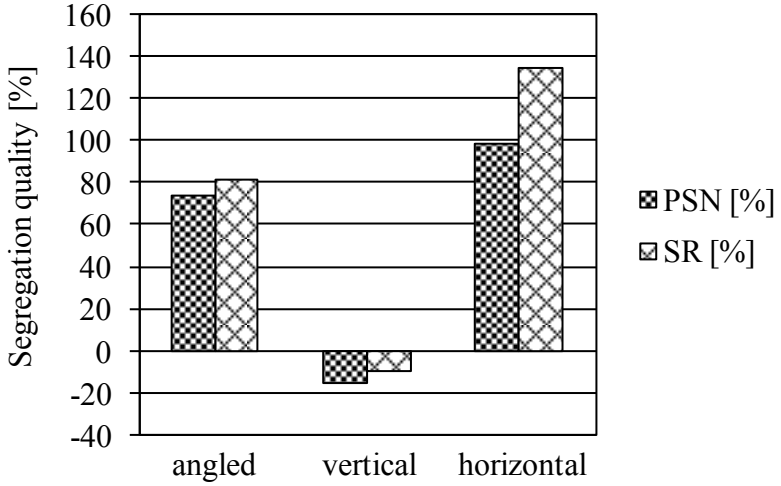

Figure 5.7: Results for PSN and SR applied to segregated beds with distinct profiles. Note that it was assumed that the respective bulk densities were $\rho_{flotsam}$ = 0.66 g/cm^3 and ρ_{jetsam} = 1.55 g/cm^3.

5.4.3 Using the CA in addition to the PSN

As shown in Figure 5.7, for three artificial beds which are all actually completely segregated and therefore should all show analysis results for the PSN and SR of 100%, a one number representation leaves out a lot of information and can by itself be a misrepresentation of the true condition inside the bed. Therefore, the CA has been utilized to aid in the segregation/mixing interpretation. Figure 5.8 illustrates the results of the segregated beds with distinct patterns when the CA is used to quantify the level of mixedness. The single number representation PSN only detects the horizontally segregated bed as being segregated, while the angled bed is found to be somewhat segregated and the vertically segregated bed is close to being perfectly mixed. Including the CA in the analysis shows that all beds are completely segregated, with ~50% of the cubes having 0% flotsam and ~50% of the cubes having 100% flotsam.

Even with increasing the cube size used in the analysis the material content registered almost exclusively 0 and 100% in each cube, showing that the beds must be segregated. The cubes that show some mixing (i.e., not 0 or 100%) are the result of the analysis cube including the flotsam-jetsam interface.

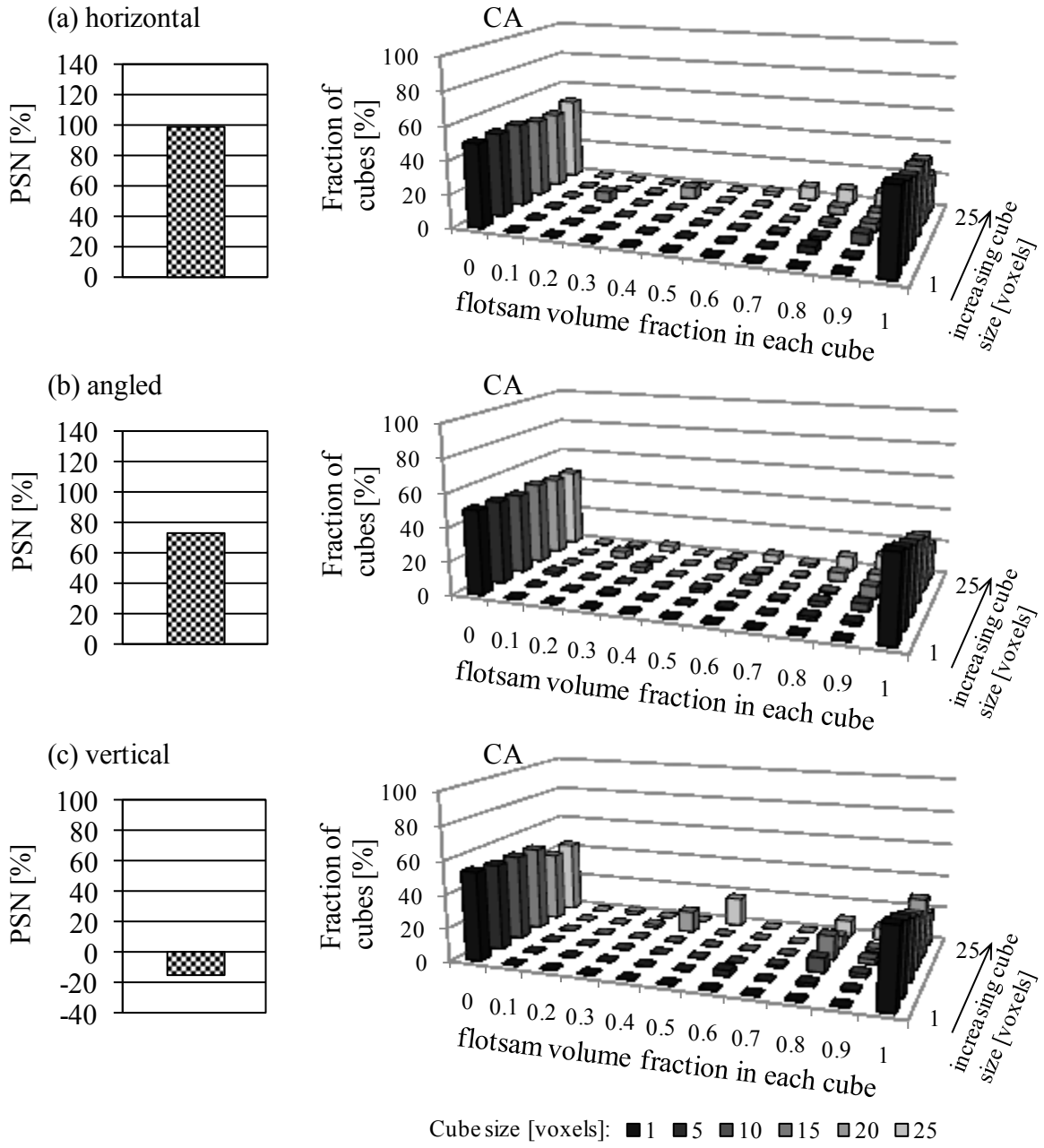

Figure 5.8: Combined results of the PSN and CA for beds with a distinct segregation pattern; (a) horizontal, (b) angled, and (c) vertical distribution.

Another way to use the CA is to interpret it as a local segregation indicator. Applying the PSN and CA to the clustered bed images shows that for some conditions the PSN indicates a globally somewhat well-mixed condition with a PSN between 0% and 10%,

while the CA reveals that there is local segregation (see Figures 5.9 – 5.11). This conclusion can be drawn by comparing the results for different cube sizes. While the small cubes (cubes with side length 1 and 5 voxels) show almost exclusively very high (100%) or very low (0%) flotsam content, larger cubes indicate a content that corresponds to the overall volume fraction of the flotsam content in the bed (e.g., 25%, 50%, or 75%). Figures 5.9 – 5.11 show a series of results for beds with 25%, 50% and 75% flotsam material content, respectively, using cluster sizes of 20 and 40 voxels diameter. For these beds, the average heights above the distributor of the spherical clusters is H/D = 0.5, the average radial position of the clusters is r/R = 0.85 and constant for all mixture ratios. Note that as the cube size used in this analysis increases, the cube volume fraction transitions from a bipolar distribution of 0 and 1 to a cube volume fraction distribution centered around the specified overall bed volume fraction.

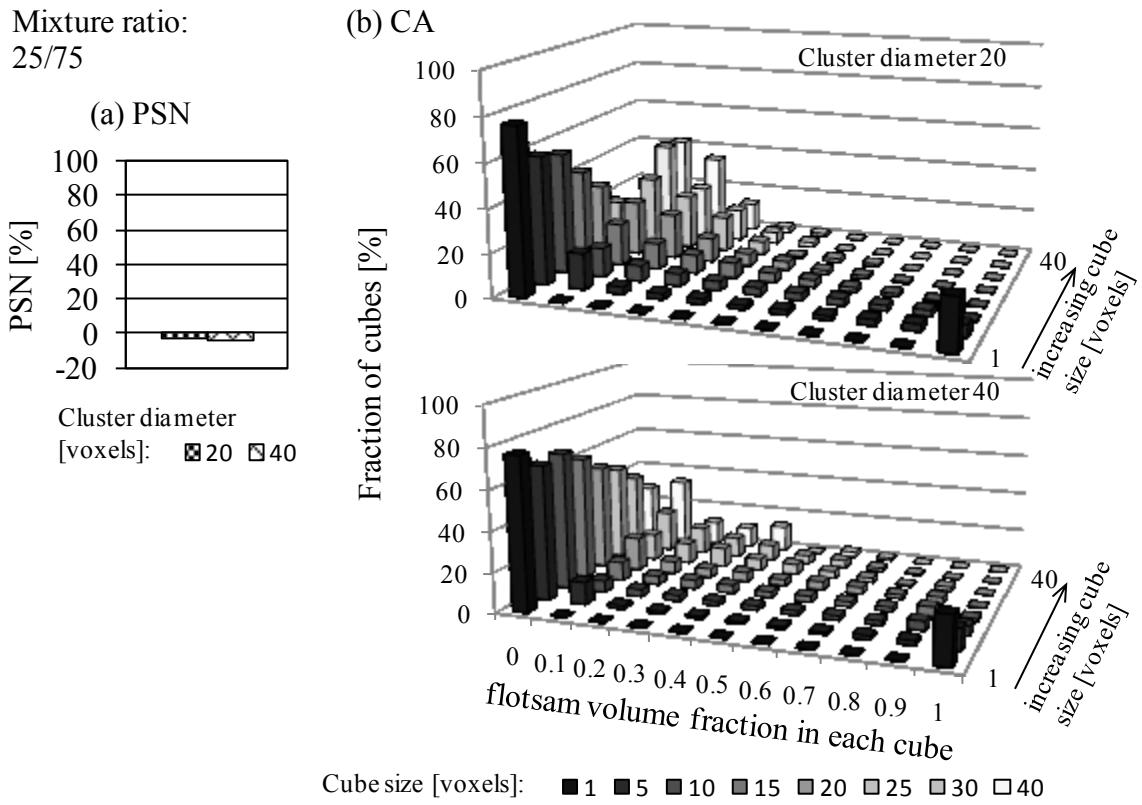

Figure 5.9: Analysis results using the PSN and CA for clustered beds with a flotsam to jetsam mixture ratio of 25%/75% by volume, and the clusters distributed in the bed with an average height of H/D = 0.5 and an average radial position of r/R = 0.85.

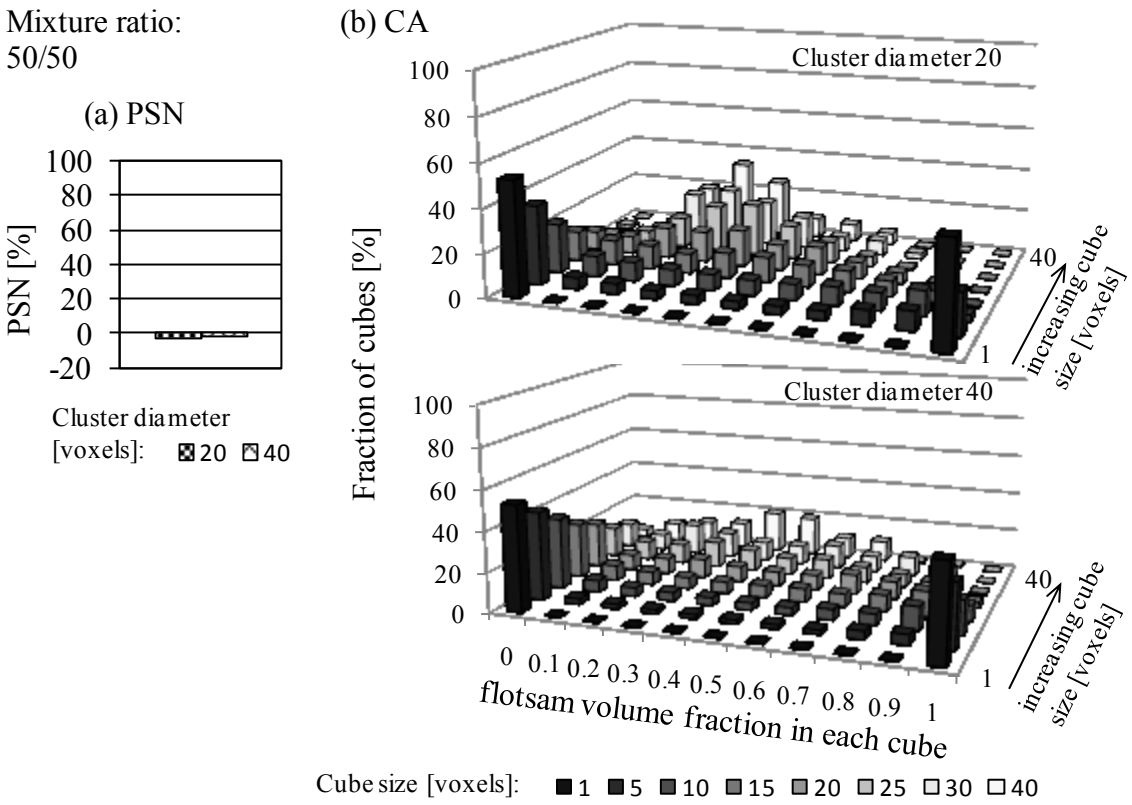

Figure 5.10: Analysis results using the PSN and CA for clustered beds with a flotsam to jetsam mixture ratio of 50%/50% by volume, and the clusters distributed in the bed with an average height of H/D = 0.5 and an average radial position of r/R = 0.85.

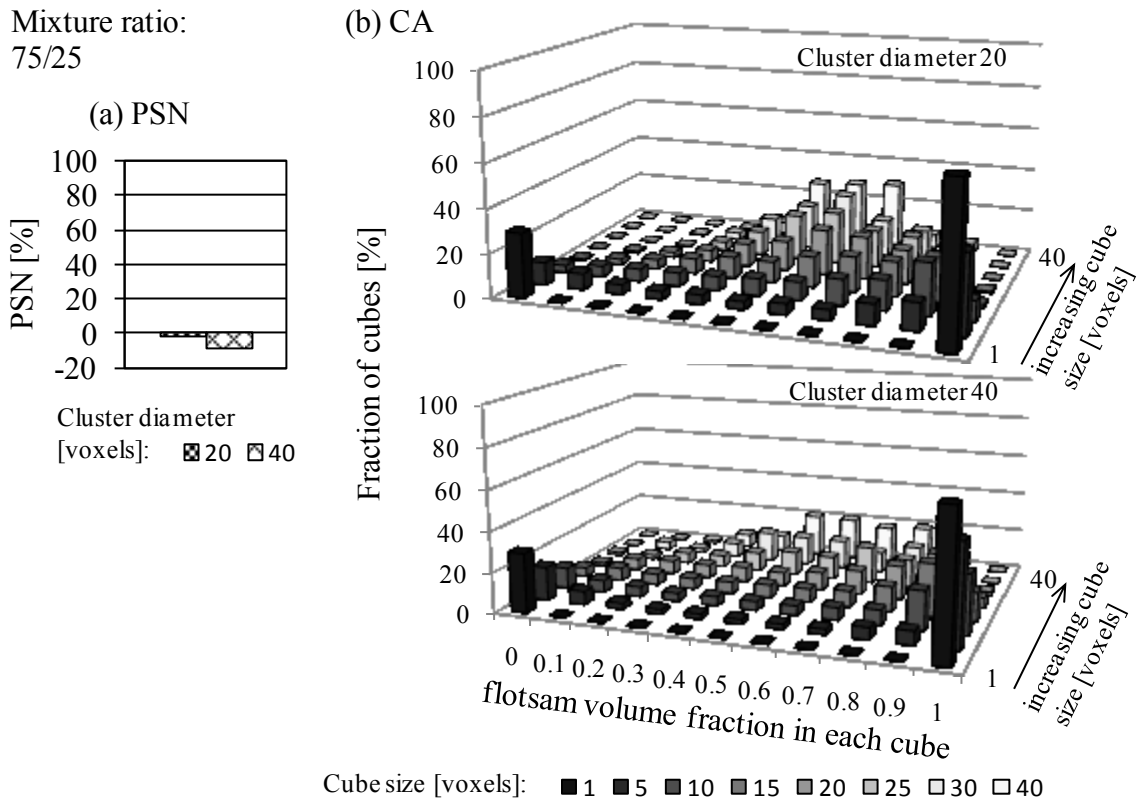

Figure 5.11: Analysis results using the PSN and CA for clustered beds with a flotsam to jetsam mixture ratio of 75%/25% by volume, and the clusters distributed in the bed with an average height of H/D = 0.5 and an average radial position of r/R = 0.85.

Figures 5.9 through 5.11 demonstrate that even though the PSN indicates the beds may be globally well-mixed, the CA limits the local mixedness to a certain cube size. In Figure 5.9 for the bed with cluster diameters of 20 voxels, the CA shows good mixedness for cube sizes greater than 20 voxels. For the bed with larger clusters (40 voxel diameter), the CA shows good mixing is measured when the cube analysis size is 40 voxels. Similarly, Figures 5.10 and 5.11 indicate a similar trend. While the PSN shows that the bed is globally well-mixed, the local mixing condition is limited and corresponds to the size of the clusters.

Finally, Figure 5.12 compares the results between a perfectly mixed and a completely segregated bed with a flotsam mixture of 50%/50% by volume for both conditions. The CA for the segregated bed in Figure 5.12b shows the same results as in Figure 5.8 because the bed is also completely segregated – a bipolar distribution of 0% and 100% flotsam in the various cube sizes. The CA for the mixed bed in Figure 5.12b shows that the bed is well-mixed for all cube sizes greater than 1 voxel because for any cube size, the flotsam material concentration is at 50% by volume, which corresponds to the overall flotsam material content. Since the CA is applied to binary images, an analysis cube size of 1 voxel will always show only 0 and 100% content; however it can be used as an indicator for the overall bed content.

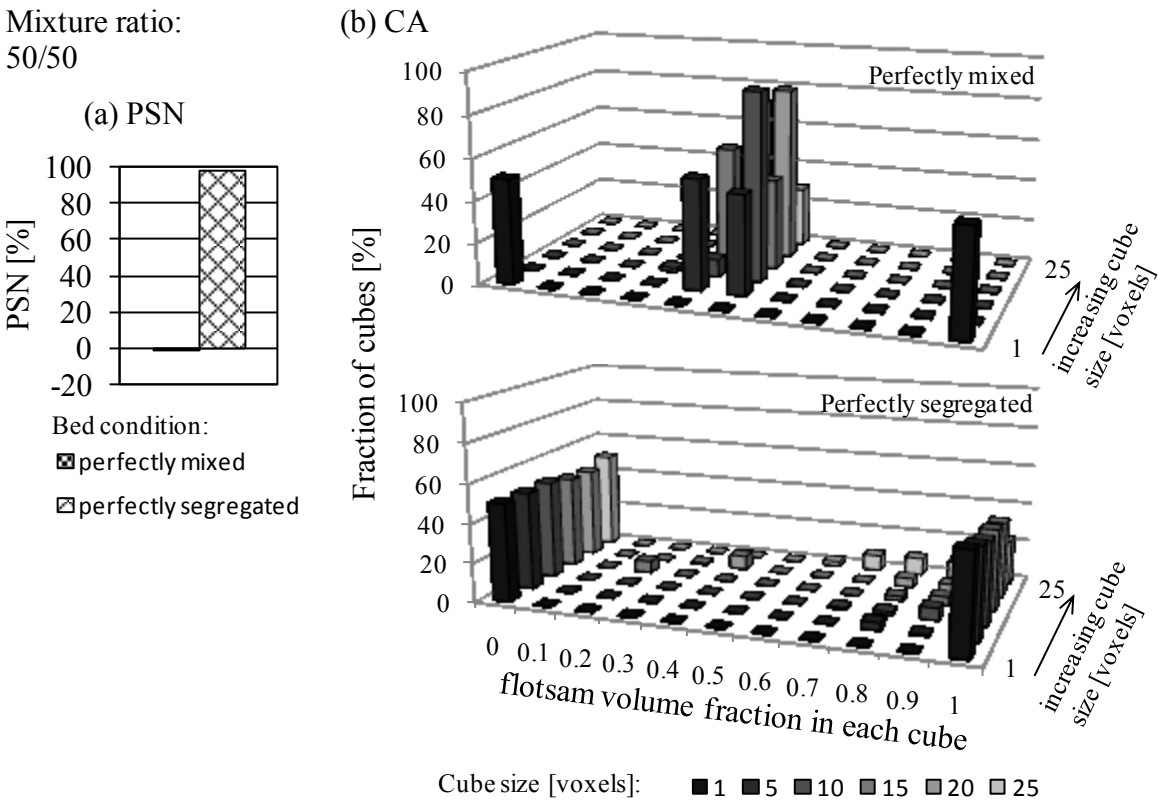

Figure 5.12: Analysis results using the PSN and CA for beds with a flotsam mixture ratio of 50%/50% by volume in perfectly mixed and completely horizontally segregated condition.

5.5 Conclusions

The PSN and CA are two analysis tools that can be helpful in determining the quality of mixing of a binary particulate system. To apply these measures knowledge of the internal structure of the system is necessary. It is useful to use both analysis tools to quantify the level of mixedness when operating parameters change the internal structure of the particulate system. It was shown that both measures are superior to prior introduced measures because of their sensitivity to small changes in the bed structure and the wide range of operating parameters to which they can be applied. They can be used together to reveal how well the system is mixed on a global and local

level. It was also demonstrated that a single segregation number can be misleading, but using the PSN in addition to the CA provides the best information on mixing quality in a particulate system.

5.6 Acknowledgements

Support for portions of the work described in this paper from ConocoPhillips Company is acknowledged.

Chapter 6 Mixing and Segregation in 3D Multi-Component Two-Phase Fluidized Beds using X-ray Computed Tomography[3]

6.1 Abstract

To operate a fluidized bed reactor most efficiently, one needs to have a good understanding of the hydrodynamics inside the bed as well as a good understanding of the mixing and segregation patterns that occur if the bed is multi-component. Many studies have been carried out in an attempt to address these issues, and the findings have contributed to make a variety of processes more efficient. However, since fluidized beds are an opaque medium, it remains difficult to experimentally investigate hydrodynamics and mixing/segregation patterns without significant trade-offs. This study discusses experimental efforts aimed at understanding mixing and segregation in multi-component cold-flow 3D fluidized bed reactors using X-ray computed tomography (CT). Using analysis tools for quantifying the bed "mixedness" and level of segregation in a collapsed fluidized bed, it is shown that the fluidization gas flow rate, particle size, mixture ratio, and humidity of the fluidizing gas stream influence the level of segregation of the fluidized bed.

Keywords: bioprocessing, fluidization, mixing, mixing quantification methods, particulate processes, segregation

[3]Based on: Keller, N.K.G., and Heindel, T.J., 2012. Mixing and Segregation in 3D Multi-Component Two-Phase Fluidized Beds using X-ray Computed Tomography. Chemical Engineering Science, under review.

6.2 Introduction

Fluidized beds have been used in industry since the early 20th century for fuel production and other applications. They feature many positive characteristics such as low pressure drop, uniform temperature distribution, and high heat and mass transfer rates that make them useful in industrial applications. Fluidized beds are commonly used for drying processes or chemical conversion processes through heat addition and/or a catalytic reactions. In rare cases they are also used for segregation processes. In all applications, the efficiency of the process is determined by the relative contact area between the different media. Therefore, the more even the material is dispersed, the more efficient the process. Although they have been widely used, fluidized beds as a whole are still poorly understood because of the complexity of the fluid-solid and solid-solid interactions. Extensive research in areas such as the hydrodynamics and mixing/segregation patterns are necessary to efficiently utilize fluidized beds, which is the focus of this study.

Academic approaches to better understand fluidized bed operation have been found to date as far back as 1955 [1]. Since then, many studies have been carried out with varying objectives and applications. However, since fluidized beds are an opaque medium, trade-offs are made to allow for the measurement of various parameters. In general, measurements can be divided into invasive and non-invasive measurement techniques. Invasive measurement techniques can give insight into a variety of parameters inside the bed when operated, but, due to their nature, have the potential of altering the bed behavior. Non-invasive measurement techniques have the advantage of not interfering with the fluidized bed, but have often been found to yield unsatisfying

results or required other trade-offs that alter the size, shape, or operating parameters of fluidized beds typically found in industry. As an example, several researchers use optical means to record experimental data, but, in order to make the fluidized bed transparent, they focused on very thin 2D fluidized beds [2-6]. In this case, valuable information can be gathered with the trade-off of highly increased wall effects and lower particle-particle interactions.

Studies have also been conducted using computational fluid dynamics (CFD) models for fluidized beds [3, 7, 9-13, 72, 106, 107]. However, since experimental data are very limited, the accuracy of these models is too.

To further improve the usage of fluidized beds in industrial applications and assist the computational development of these facilities, detailed experimental data from 3D fluidized beds gathered through measurements that do not alter their behavior are necessary. Therefore, this study uses noninvasive X-ray CT imaging to experimentally study mixing and segregation in multi-component 3D fluidized beds. The method has been built upon the successful completion of earlier studies aimed at the hydrodynamics of single component beds using the same measurement techniques [14, 21, 23, 108]. The effects of a variety of operating parameters, such as particle size, superficial gas velocity, and mixture ratio, on the mixing condition will be discussed.

6.3 Experimental procedures

6.3.1 Fluidized bed reactor

As illustrated in Figure 6.1, the cold-flow fluidized bed used to acquire the experimental data in this study is composed of a 10.2 cm inner diameter acrylic tube,

and includes a plenum, bed chamber, and riser or free-board region. The distributor, mounted between the plenum and bed chamber, is made of an acrylic plate containing 63 1 mm diameter holes drilled in concentric circles, giving the aeration plate an open area ratio of 0.62%. To prevent particles from falling through the holes or plugging them, a fine mesh screen is placed right above the distributor plate. Air enters the plenum through the inlet in the bottom of the plenum, which is filled with marbles to evenly disperse the air over the bottom of the aeration plate.

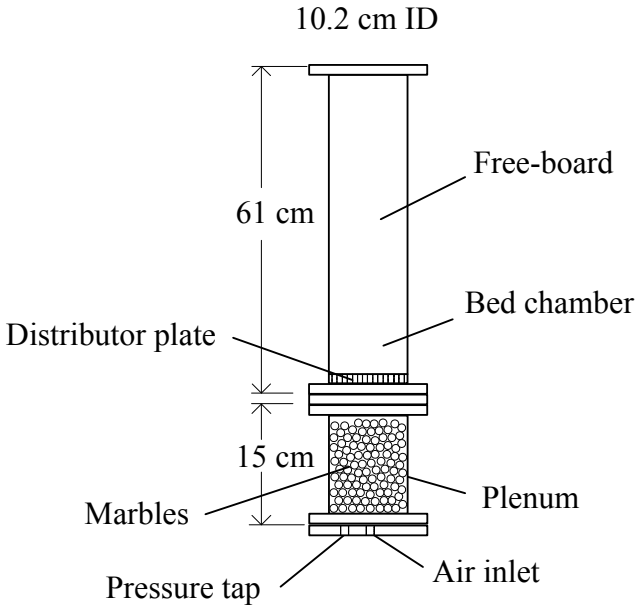

Figure 6.1: Schematic of model fluidized bed reactor.

6.3.2 Material selection

The materials selected for this study cover a range of particle sizes, are readily available, and mimic material that may be found in fluidized bed gasifiers. The inert bed material is often refractory sand because of its thermal properties and availability. For this study, glass beads (GB) have been selected as the inert bed material because they have very similar properties to that of sand, but are better characterized and more

uniform in shape, which is beneficial for laboratory experiments and for CFD comparisons [109].

The second granular material in the bed was ground walnut shell (GWS), which is very similar to the biomass particles typically used in gasifiers for biomass-to-fuel conversion. Close-ups of the GB and GWS are shown in Figure 6.2. The photographs are taken with a magnification factor of 10 and show particles in the range of 500-600 µm for both materials.

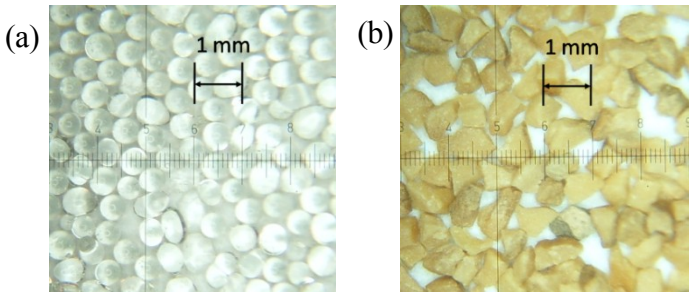

Figure 6.2: Close-ups of bed materials in the 500-600 µm particle size range, (a) GB, and (b) GWS.

As shown in Figure 6.2a, the GB particles are smooth, solid, and almost spherical, and the particle size range appears to be fairly narrow. Figure 6.2b shows that the GWS particles are not as smooth and round because they are a natural material and the manufacturing process is different; the GWS appear to be mostly “chunk-like” – it looks like gravel.

Glass beads in the size range of 500-600 µm diameter are used as the inert bed material for all experiments, while ground walnut shell in one of three size ranges (212-300 µm, 500-600 µm, and 800-1000 µm) are selected as the second component. After sieving the particles multiple times with American standard sieves, it is assumed that

the particles are normally distributed within the given size ranges. The particle size range, densities, and particle masses are listed in Table 6.1. Since this study focuses on the mixing and segregation of two granular type components, all particles are chosen so that they comply with Geldart type B systems for easy fluidization.

Table 6.1: Properties of bed materials.

Particle properties	Diameter [μm]	Individual particle density (average) [g/cm^3]	Individual particle mass [10^4 g]
Glass beads (GB)	500-600	2.60	1.70 - 2.90
Ground walnut shell (GWS)	212-300	1.30	0.06 - 0.18
	500-600		0.85 - 1.50
	800-1000		3.50 - 6.80

6.3.3 Minimum fluidization and experimental conditions

The minimum fluidization velocity, U_{mf}, is one of the most important fundamental parameters related to fluidization hydrodynamics and is used to normalize flow conditions in this study. U_{mf} is experimentally determined for a bed of glass beads for the model FBR used in this study using the procedure outlined by Franka (2008) [16]; for this test, the bed was filled to a height of 1 column diameter with the 500-600 μm glass beads. On this basis, three different superficial gas velocities, relative to U_{mf}, have been applied to each bed as summarized in Table 6.2.

Table 6.2: Superficial gas velocity of experiments.

Minimum fluidization velocity of glass beads	10.2 cm ID bed
$U_{mf,GB}$ [cm/s]	21.3
Superficial gas velocity applied [cm/s]	
1 x $U_{mf,GB}$	21.3
2 x $U_{mf,GB}$	42.6
3 x $U_{mf,GB}$	63.9

6.3.4 X-ray imaging facility

X-ray flow visualization of multiphase flows has recently been reviewed [51], and the facility used in this study has been detailed elsewhere [14] so only a brief description is provided here.

As Figure 6.3 illustrates, two LORAD LPX200 X-ray sources are mounted perpendicular to each other on a 1 m inner diameter gear ring that can rotate 360°. The sources allow adjusting of the voltage (10–200 kV) and current (0.1–10 mA) up to a total power output of 900 W for each source. Low energy radiation is suppressed by a combination of 1 mm thick copper and aluminum filters. Mounted opposite of the X-ray sources are X-ray imaging devices, either two image intensifier/CCD camera pairs or a cesium-iodide scintillator screen.

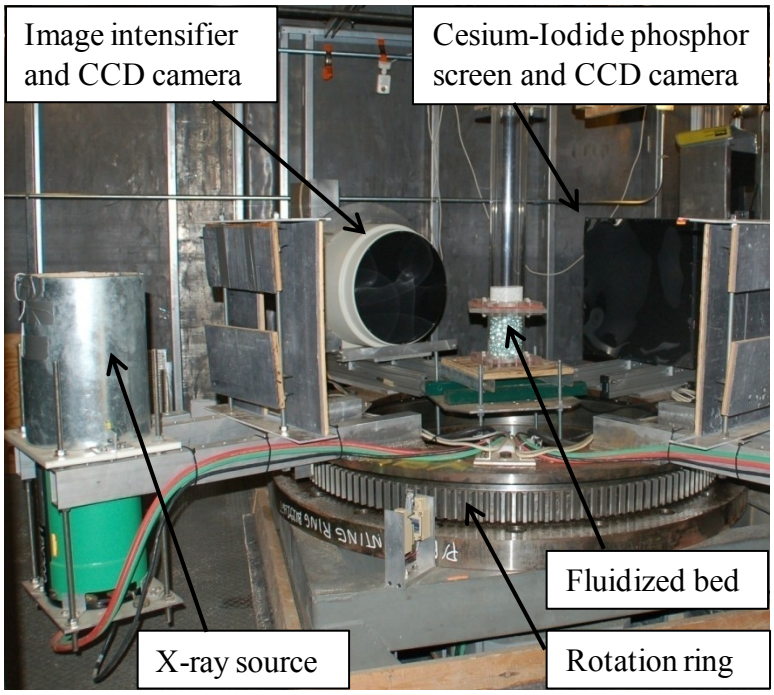

Figure 6.3: Picture of X-ray imaging facility.

In this study, a 44×44 cm cesium-iodide scintillator screen is used as the detector and transforms radiation into visible light. The image is captured by an Apogee Alta U9 system with a 50 mm Nikon lens. This system has 3072×2048 pixels with binning capabilities and is thermoelectrically cooled to allow for long exposure times.

6.3.5 Computed tomography scans

To acquire CT data, the scanner rotates around the object of interest, taking a series of 2D projections at different angles which are later back-projected using a reconstruction algorithm and custom computer programs [14, 51]. This procedure yields a digital 3D image for further analysis. The local variation of voxel intensity, where a voxel is a 3D pixel, in this 3D array corresponds to the attenuation variation of the X-ray beam as it passes through the object, which in turn is a function of density, material thickness, and attenuation coefficient. This is later used to derive the material distribution inside the reactor.

The reconstructed 3D images of the object can be sliced to show internal structure of the mixture as shown in Figure 6.4. Because the voxels hold intensity data, the slice images are in gray scale; however, images can be given a false color to improve contrast. All images reported in this study will only show x-slices although others can be easily produced. The reported CT values are averaged over concentric annuli or averaged over horizontal slices.

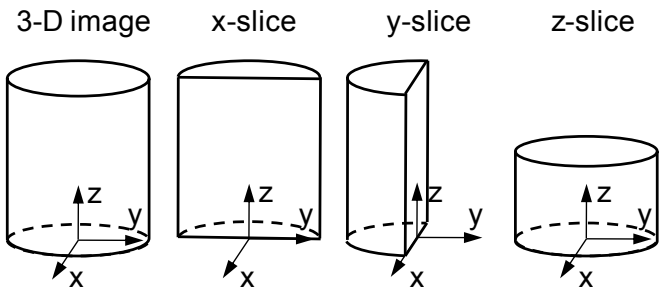

Figure 6.4: CT imaging planes.

6.3.6 Beam hardening correction

The most commonly encountered artifact in X-ray CT imaging is beam hardening. It is caused by lower energy X-rays being more readily attenuated than higher energy X-rays. It is a function of material density, material thickness, and attenuation coefficient [51]. It causes the edges to appear lighter and the center to appear darker in the reconstructed image. Hence, for a cylindrical object of uniform density, an uncorrected CT value would vary with radius. Figure 6.5 shows the effects of beam hardening for a full bed of glass beads (top curve) and a full bed of ground walnut shell (bottom curve). The higher density glass beads are more affected by beam hardening, while the lower density ground walnut shell show almost no effect. The CT values are the average for concentric annuli with one pixel thickness. The effects of beam hardening complicates the analysis when determining mixing and segregation between glass beads and ground walnut shell.

Usually, beam hardening can be accounted for by applying a correction algorithm for known material density. However, since this study deals with mixing and segregation of two components inside the bed, the density of any control volume will vary with time and

location. Therefore, a primary objective of the analysis and development method has been to properly account for beam hardening.

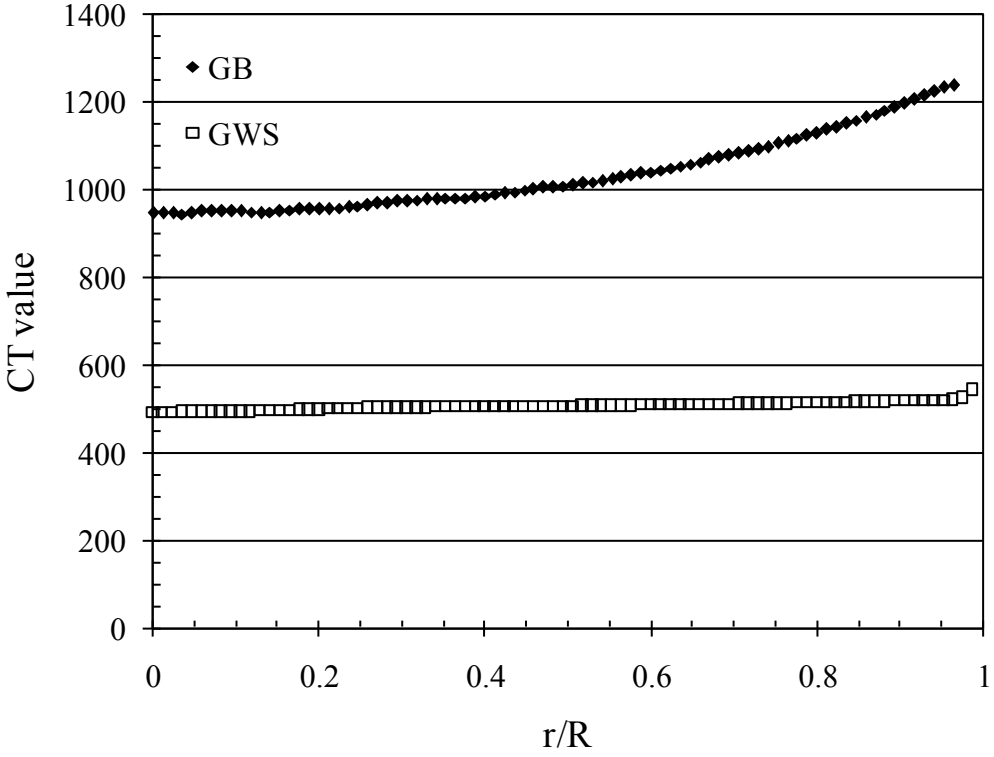

Figure 6.5: Average CT values for concentric annuli in a bed of either 100% glass beads (GB) or 100% ground walnut shell (GWS).

The experimental data have been acquired with collapsed (static) fluidized beds after a given fluidization time. All images were taken with the X-ray source settings 150 keV and 3.5 mA. The X-ray beam was filtered with one 1 mm thick aluminum filter and one 1 mm thick copper filter. Images were acquired for every degree, totaling 360 images, with the camera set at 4×4 binning. The system was configured to yield a voxel size, where a voxel is a 3D pixel, of roughly 580 μm on a side.

To calibrate voxel intensity to mixture composition, a series of CT scans were performed with different composition ratios of well-mixed systems. Eleven different bed

compositions were scanned for each GWS particle size range, ranging from pure glass beads to pure ground walnut shell, with a uniformly incremented volume ratio. Table 6.3 summarizes these experiments.

Table 6.3: Overview of calibration experiments for each GWS size range.

Reference scan	Volume ratio
1	100% GB
2	10% GWS + 90% GB
3	20% GWS + 80% GB
4	30% GWS + 70% GB
5	40% GWS + 60% GB
6	50% GWS + 50% GB
7	60% GWS + 40% GB
8	70% GWS + 30% GB
9	80% GWS + 20% GB
10	90% GWS + 10% GB
11	100% GWS

A sample of the CT values are shown in Figure 6.5 for the 500-600 μm GB and 500-600 μm GWS system. As shown in Figure 6.5, the CT values are a function of bed radius, but not a function of bed height; this is shown in Figure 6.6 where the horizontal average CT value is plotted as a function of bed height for three different bed compositions. The error bars in Figure 6.6 represent one standard deviation from the averaged values. In general, the average CT value is uniform through the entire bed height. The small variations in the 25% GWS - 75% GB system are attributed to small nonuniformities in the local mixture composition.

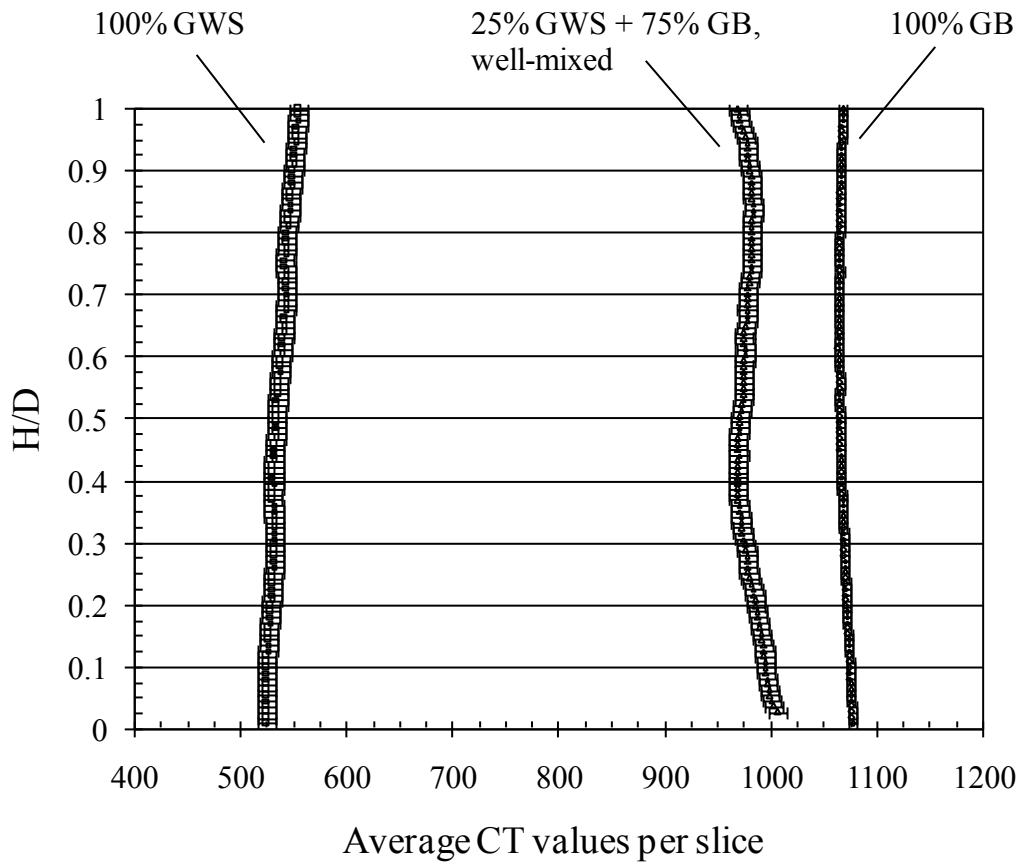

Figure 6.6: Variation of average CT values as a function of bed height for the 500-600 µm GB and 500-600 µm GWS system.

Assuming a homogeneous particle distribution, CT values for the eleven well-mixed systems were averaged over concentric radii and plotted as a function of radius. These data were used to generate a matrix that correlates the voxel CT value to the biomass volume fraction as a function of bed radius. This calibration is possible because the variation over the bed height is minimal (Figure 6.6) and beam hardening uniformly affects the values within the annulus. Figure 6.7 shows a summary of the acquired calibration data for the various bed compositions. Each curve represents the CT value averaged for concentric annuli of one voxel thickness for various mixture volume ratios in 10% steps. The nonlinearity of the respective curves result from beam hardening.

The top curve represents a bed of pure GB, showing the largest impact of beam hardening due to the high density of the material. This causes higher CT values towards the edge of the bed and lower CT values in the center. The nearly flat curve on the bottom represents a bed of pure GWS, which has negligible beam hardening. The curves in between are for the different volume ratios between GB and GWS. Note that image saturation near the wall, where the X-ray path length through the bed is a minimum, results in increased noise in the data in this region; these data are omitted from the calibration.

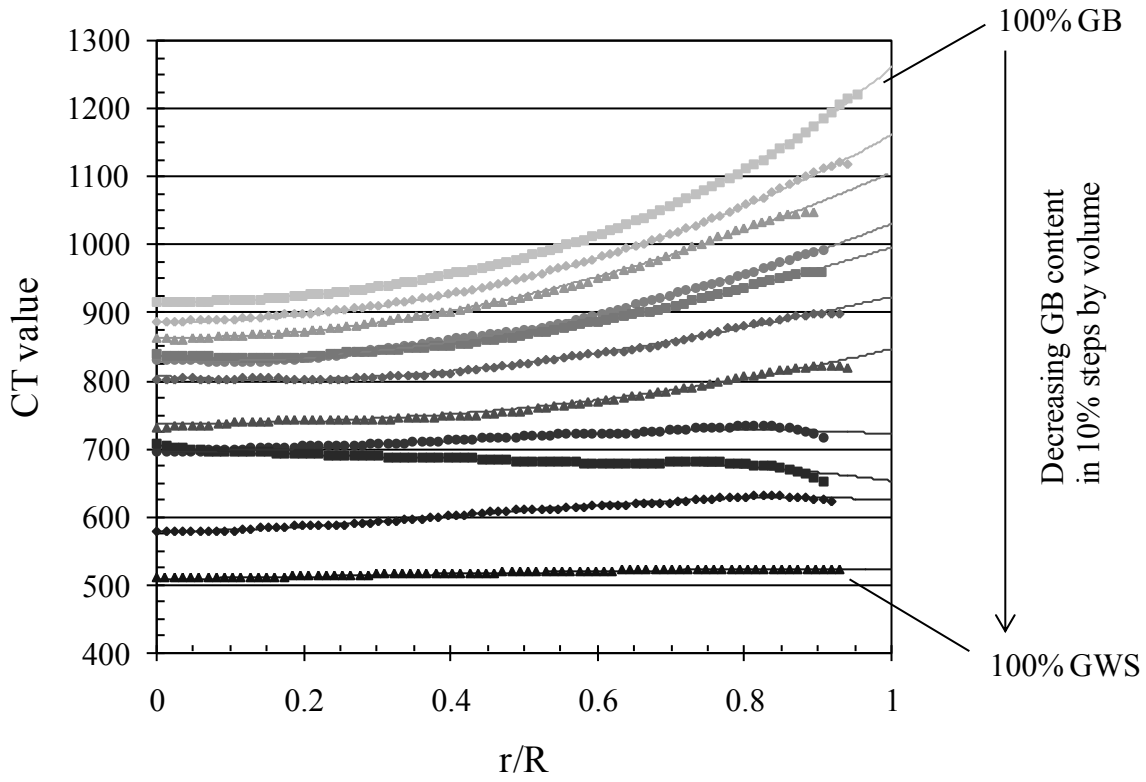

Figure 6.7: CT values as function of radius and mixture ratio for mixtures of 500-600 μm glass beads and 500-600 μm ground walnut shell.

Third order polynomial curve-fits have been generated from each curve in Figure 6.7. The curves have been extrapolated all the way to the bed wall. These curve-fits

were used to generate a bed composition matrix for the respective CT value as a function of bed radius. The composition matrix is then used as a “look-up table” to correlate the experimental local voxel CT value at a particular radius to the local voxel biomass composition on a volume basis. Hence, the 3D data are transformed from local CT value to local concentration of the second component within the entire 3D volume.

Figure 6.7 also demonstrates the attenuation dependence on the density of the material. The top curve represents the CT values as a function of the radius for a bed of 100% 500-600 μm GB and shows that the CT values for these are just above 900 in the center and increase towards the edge following the third order polynomial pattern with the highest value at the edge of around 1250. The bottom curve represents the CT values as a function of the radius for a bed of 100% 500-600 μm GWS. Since GWS has a significantly lower density, it is much less affected by beam hardening. Therefore, the CT values are still the lowest in the center at just above 500 and nearly constant as a function of radius. A similar calibration procedure was used for mixtures of 500-600 μm GB and 212-300 μm GWS, as well as for mixtures of 500-600 μm GB and 800-1000 μm GWS.

The success of this method can be demonstrated by sample images. Figure 6.8 illustrates the center slice of a scan of a random mixture of inert bed material with 50% by volume 500-600 μm GWS in the 10.2 cm ID collapsed static fluidized bed. It can be seen that the patterns in the original CT scan image (Figure 6.8a) are also found in the converted material content image (Figure 6.8b). In the converted image only the region of interest is analyzed, i.e., only the bed itself, leaving out the reactor walls and flange region. In Figure 6.8b, the white regions represent 100% GWS while the black regions

in the region of interest correspond to 100% GB, and the gray scale varies linearly with GWS volume fraction content. Note that summing the voxel volume fractions in the entire bed yields the known total volume of the biomass particles within 5% of the actual volume.

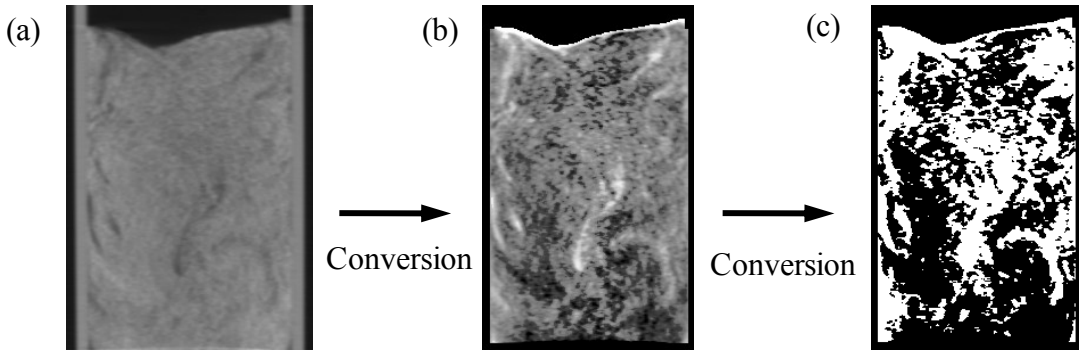

Figure 6.8: Center slice of a sample of a random mixture of inert bed material with 50% by volume 500-600 μm GWS, (a) original CT scan image, (b) converted material content image, and (c) converted binary image.

A converted binary image is also illustrated in Figure 6.8c; this image is used for further processing, especially to extract features to characterize the particular bed as explained in the following section. To convert the material content image into a binary image, the appropriate threshold must first be found. As an example, for a bed with 25% GWS, if the GWS is very evenly dispersed in the inert bed material, a threshold of 50% percent would yield a binary image with no GWS at all. Therefore, an algorithm calculates the total amount of GWS in the particular bed and compares it with the known initial amount of GWS by volume. A trial-and-error iteration is used to correct the threshold value until the overall error in the binary image is less than 5% of the total volume.

6.4 Analysis techniques

6.4.1 Particle Segregation Number (PSN)

To illustrate time resolved segregation data and the ability to compare fluidized beds over a wide range of operating parameters, it is necessary to have an analysis tool that would represent any particular particle configuration inside the bed in terms of its "mixedness" as a single number and still be sensitive enough to small variations. Both the Mixing Index [66] and the Segregation Rate [2] offer this convenience. However, it was found that both approaches have limitations for the use with systems that have varying particle densities and/or mixture ratios [110]. Therefore the "Particle Segregation Number" (PSN) has been developed. It is calculated on the basis of the normalized average heights of the inert bed material and the second granular material. Thus, the particle segregation number is defined as:

$$\mathrm{PSN} = 2*\left[\frac{\overline{h_F}}{H} - \frac{\overline{h_J}}{H}\right]*100\% \tag{6.1}$$

where H denotes the total static bed height. The parameters $\overline{h_F}$ and $\overline{h_J}$ denote the average heights above the distributor of flotsam (GWS) and jetsam (GB) particles [62], respectively, and are calculated as:

$$\overline{h_F} = \frac{\sum h_{F,i,j}}{N_F} \tag{6.2}$$

$$\overline{h_J} = \frac{\sum h_{J,i,j}}{N_J} \tag{6.3}$$

where $h_{F,i,j}$ and $h_{J,i,j}$ are the height of individual flotsam and jetsam voxels, respectively, and N_F and N_J are the total number of voxels attributed to flotsam or jetsam content in a binary image. The binary image is obtained by converting the concentration image through an iterative process to maintain the overall flotsam content in the region of interest, thus identifying each voxel as either flotsam or jetsam. It was found that, independent of the material volume ratio, the difference in normalized average bed heights for a completely horizontally segregated bed will always be 0.5, while for a perfectly mixed bed the difference will always be 0. Hence, the factor of 2 in Eqn. (6.1) results in the PSN describing any bed condition between 0 and 100%. If PSN = 0, the bed is ideally mixed; for PSN = 100%, the bed is completely horizontally segregated. This is a simple and convenient way to express the condition of any particulate system in terms of the level of “mixedness”.

6.4.2 Cube Analysis (CA)

Because the PSN represents the level of mixedness of any bed with a single number, it cannot identify if a two-component fluidized bed developed pockets of high concentration of one or the other component, which is imaginable because it cannot be excluded based on existing knowledge about fluidized beds. Also, as will be shown later, to express the mixedness with a single number leaves a lot of information out and can potentially lead to a false conclusion about the condition of the bed. Therefore, a method has been developed to help understand concentration profiles within a two-component fluidized bed with respect to the formation of high concentration pockets; we term this the “cube analysis” (CA) [104].

The CA algorithm calculates the average concentration of neighboring voxels for all cubes with the side length a_C within the bed region. This analysis is done for cubes with varying side length, from a_C = 1, for one voxel per cube only, up to 50 voxels side length. The results are then sorted to be displayed in a histogram. If the fluidized bed contains pockets of high concentration, it would be visible in the histogram by a peak for cubes with a certain side length. This will also indicate the size of the pocket. The CA is then used as an additional tool for characterizing the fluidized bed level of mixedness.

Both the PSN and CA have been explained in detail and their usefulness demonstrated by [110].

6.5 Results and discussion

6.5.1 Repeatability of experiments

To show that the experimental procedures are repeatable, a series of experiments with 50% by volume 500-600 μm GWS and 50% by volume 500-600 μm GB was completed and then repeated four times for flow conditions of U_g = 1, 2, and 3 U_{mf} with dry air to yield a set of five experiments for each condition. These results are then analyzed and used to calculate the deviation associated with the PSN.

Figure 6.9 shows the results for each set of experiments for the different flow velocities, (a) U_g = 1 U_{mf}, (b) U_g = 2 U_{mf}, and (c) U_g = 3 U_{mf}. In each experiment, a well-mixed bed was fluidized for 20 seconds and then abruptly collapsed. An X-ray CT was then performed and the bed was again fluidized for 20 seconds and then abruptly collapsed for another X-ray CT. This was repeated until a total fluidization time of 60 seconds elapsed. The uncertainty for the measurement is calculated as the standard

deviation from the five individual tests and marked by the error bars in the graphs, with a maximum uncertainty for all experiments being ± 9%. Typically error values are less than this and on the order of ± 6%.

Figure 6.9 shows that the experimental procedures are repeatable. There is a significant dependence of the level of segregation on the superficial gas velocity. Lower superficial gas velocity (Figure 6.9a) causes the bed to segregate while higher superficial gas velocity (Figure 6.9b and c) maintains a mixed bed. Increasing the superficial gas velocity from $U_g = 2\ U_{mf}$ to $U_g = 3\ U_{mf}$ also doesn't yield much additional mixing, while increasing from $U_g = 1\ U_{mf}$ to $U_g = 2\ U_{mf}$ yields much better mixing. All conditions examined for this part of the study also show that the bed reaches a steady state condition fairly quickly, within 40 seconds or less of fluidizing.

Although fluidized bed hydrodynamics are very complex and many factors influence the results, the experiments show good repeatability and the results for the PSN are in an acceptable tight range. The results for the CA confirm the findings as well. Figure 6.10 illustrates the results in terms of CA for experiments completed with 50% 500-600 μm GWS and 50% 500-600 μm GB for $U_g = 1\ U_{mf}$ and repeated 4 times. At t = 0, the histogram peak around 0.5, indicating a mixed bed with 50% by volume GWS. As time progresses, the distributions become bi-modal with peaks approaching 0 (100% GB) and 1 (100% GWS), indicating the bed becomes segregated. The results confirm that the experimental procedures and both analysis methods are repeatable. A similar analysis using the CA has been conducted on the other two sets of experiments ($U_g = 2\ U_{mf}$ and $U_g = 3\ U_{mf}$) and those also show good repeatability. Only the results for $U_g = 1\ U_{mf}$ are presented here as they showed the most variation.

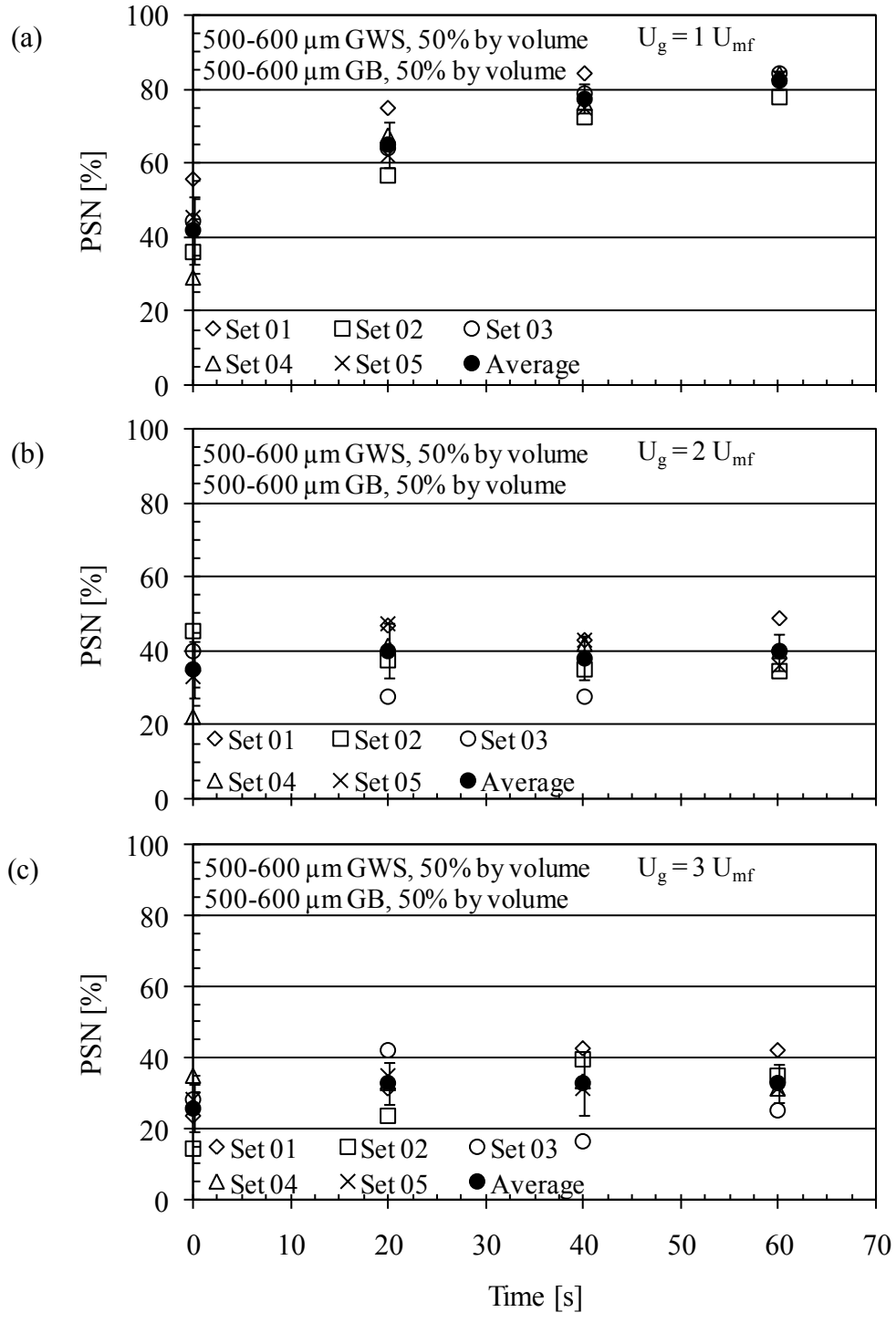

Figure 6.9: PSN results of experiments with 50% 500-600 µm GWS mixed with 50% 500-600 µm GB, (a) $U_g = 1\ U_{mf}$, (b) $U_g = 2\ U_{mf}$, and (c) $U_g = 3\ U_{mf}$.

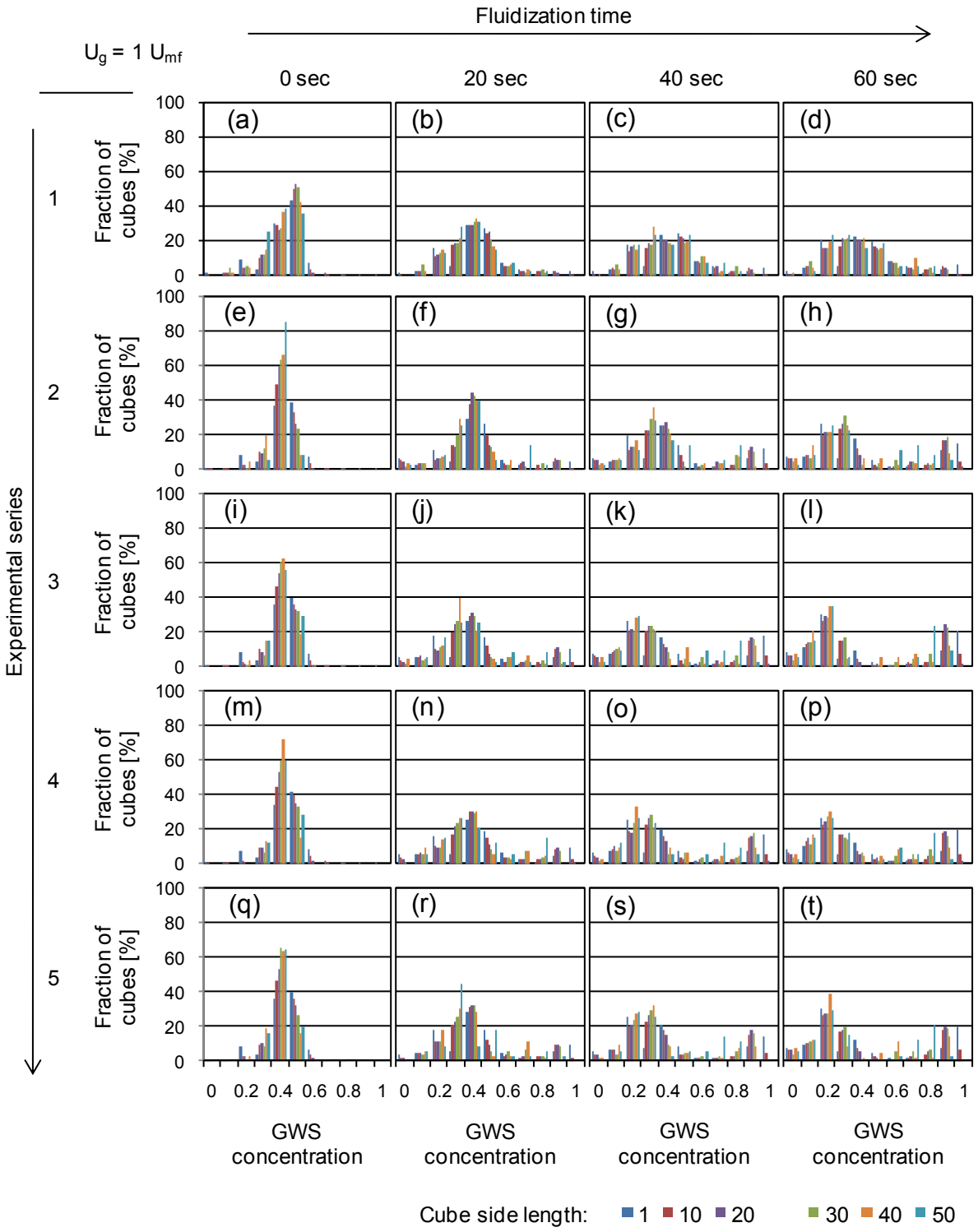

Figure 6.10: CA results of experiments with 50% 500-600 µm GWS mixed with 50% 500-600 µm GB, fluidized at U_g = 1 U_{mf}. All experiments were completed 5 times.

6.5.2 Effect of superficial gas velocity

To understand the effect of superficial gas velocity on the mixing/segregation behavior, experiments with three different superficial gas velocities (U_g = 1, 2, and 3 U_{mf}; U_{mf} being the minimum fluidization velocity for a full bed of GB for one diameter bed height) have been conducted for all mixture ratios and particle size ranges of GWS. Figure 6.11 shows PSN results for: (a) a bed of 25% 500-600 μm GWS with 75% 500-600 μm GB, fluidized for 20 second intervals at U_g = 1, 2, and 3 U_{mf}; and (b) a bed of 50% 800-1000 μm GWS with 50% 500-600 μm GB, fluidized for 20 second intervals at U_g = 1, 2, and 3 U_{mf}. These conditions are examples to demonstrate the above mentioned effects.

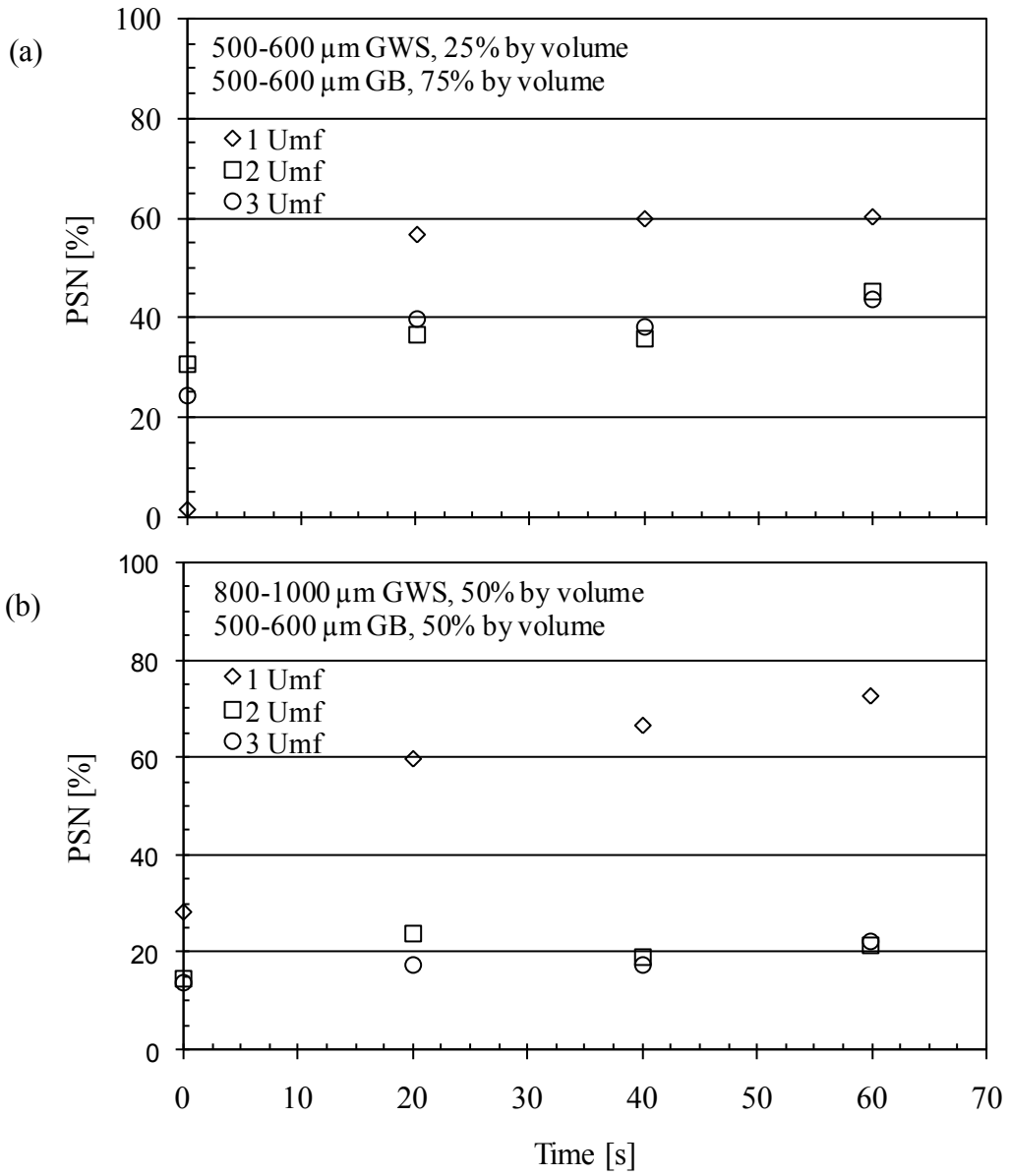

Figure 6.11: PSN results for: (a) 25% 500-600 µm GWS with 75% 500-600 µm GB, and (b) 50% 800-1000 µm GWS with 50% 500-600 µm GB, both fluidized for 20 second intervals at U_g = 1, 2, and 3 U_{mf}.

The experiments show that a superficial gas velocity of just above the minimum fluidization velocity causes the bed material to segregate. Lighter particles (GWS, flotsam) will flow to the top, heavier particles (GB, jetsam) will sink to the bottom. Higher gas flow rates promote mixing, i.e., as the gas flow rate is increased, segregation

becomes less. There is a small but measurable difference in the quality of the mixing, or the level of “mixedness”, between U_g = 2 U_{mf} and U_g = 3 U_{mf}. The higher gas flow rate enhances mixing, resulting in a lower PSN. While at U_g = 1 U_{mf}, the fluidized bed segregates with a PSN approaching 100% for some conditions [105]. Better mixing is achieved with a gas flow rate of U_g = 2 U_{mf} when compared to U_g = 1 U_{mf}, with the lowest PSN observed for U_g = 2 U_{mf} being 10% [105]. When U_g = 3 U_{mf}, only slightly better mixing is observed with a minimum PSN of 8% [105]. It is hypothesized that even higher superficial gas velocities would further enhance mixing. These conclusions were found to be independent of other factors, i.e., it is true for all particle sizes considered, all mixture ratios, humidified or dry fluidizing gas. It also coincides with observations from other research studies [46, 62, 103], and confirms the utility of the PSN.

Figure 6.12 uses the CA analysis to show the effect of fluidization velocity for 50% 500-600 μm GWS mixed with 50% 500-600 μm GB and fluidized with dry air for 60 seconds from an initially well-mixed state. In Figure 6.12a, the material is very segregated when fluidized for 60 seconds at U_g = 1 U_{mf} . When U_g = 2 or 3 U_{mf}, the beds are better mixed as indicated by the volume fraction distribution for the cube sizes greater than 1 voxel.

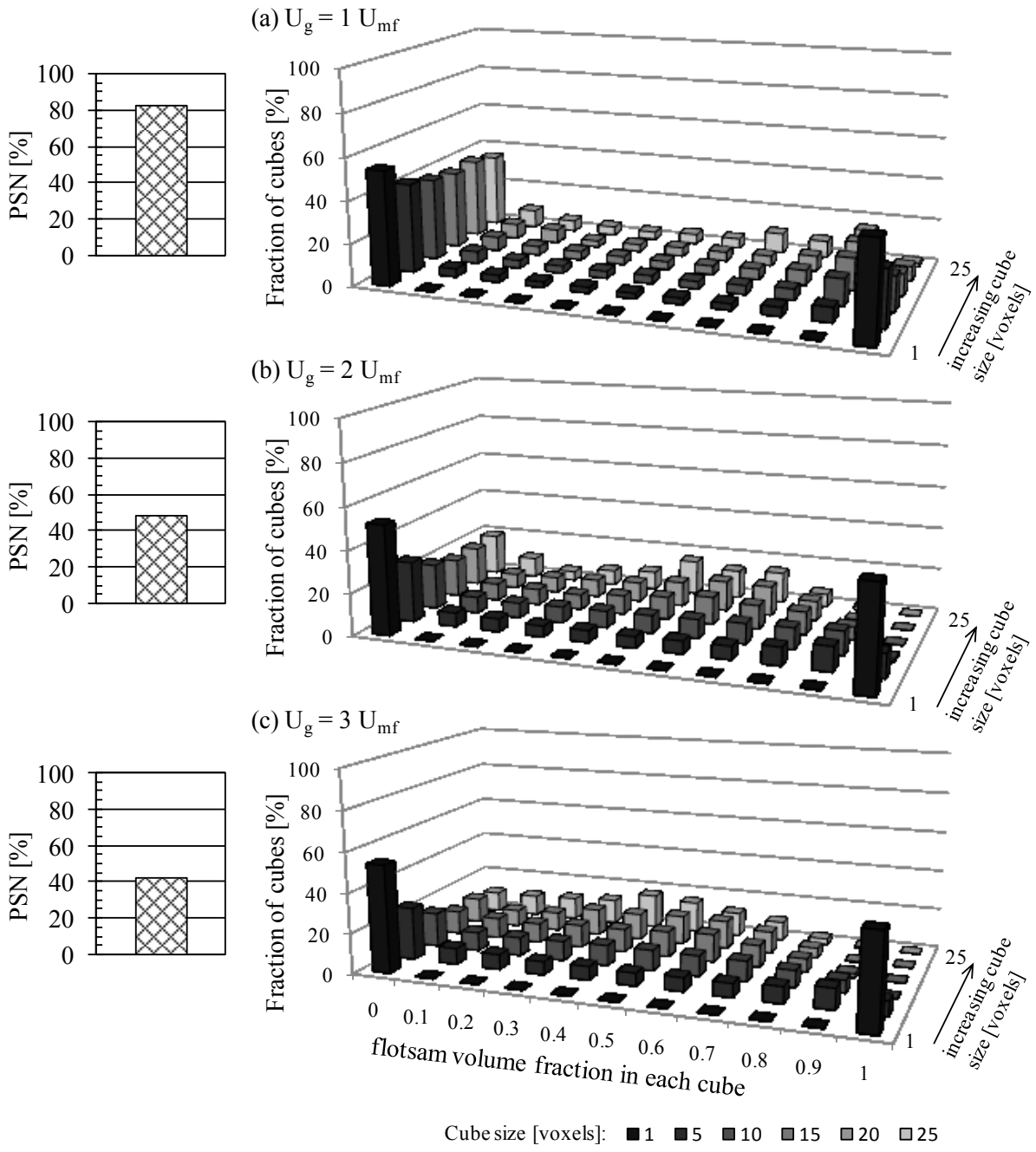

Figure 6.12: CA and PSN results of experiments with 50% 500-600 µm GWS mixed with 50% 500-600 µm GB after 60 seconds of fluidizing from an initially well-mixed state with dry air.

6.5.3 Effect of particle size

Experiments have been completed with three different GWS particle size ranges while the particle size range for the inert GB material remained the same. The particle

size ranges for GWS are 212-300 μm, 500-600 μm, and 800-1000 μm, and the particle size range for GB remains fixed at 500-600 μm. Note that GWS is less dense than GB. The particle size ranges were chosen so that the model biomass particles have (a) the same size as the inert material, (b) a significantly smaller size, and (c) a significantly larger size.

It was found that as the particle size for GWS is increased, the particles tend to remain mixed. Figure 6.13 illustrate examples for different mixture ratios and superficial gas velocities. The results match those found in the literature [2, 44-47, 62, 66, 101, 103, 111-113]. The graphs in Figure 6.13 also illustrate that the observed effect is independent of superficial gas velocity or mixture ratio. A reasonable explanation for this effect is given by the total mass ratio of individual particles. As an approximation, if the particles are considered spherical and solid the mass of individual particles can be determined and are summarized in Table 6.1. For mixtures with small GWS particles, the mass difference between flotsam and jetsam particles is quite significant and the light GWS particles are displaced by the heavier GB particles. As the GWS particle size is increased, the mass difference becomes less and the buoyancy forces equal out, resulting in the GWS particles remaining mixed.

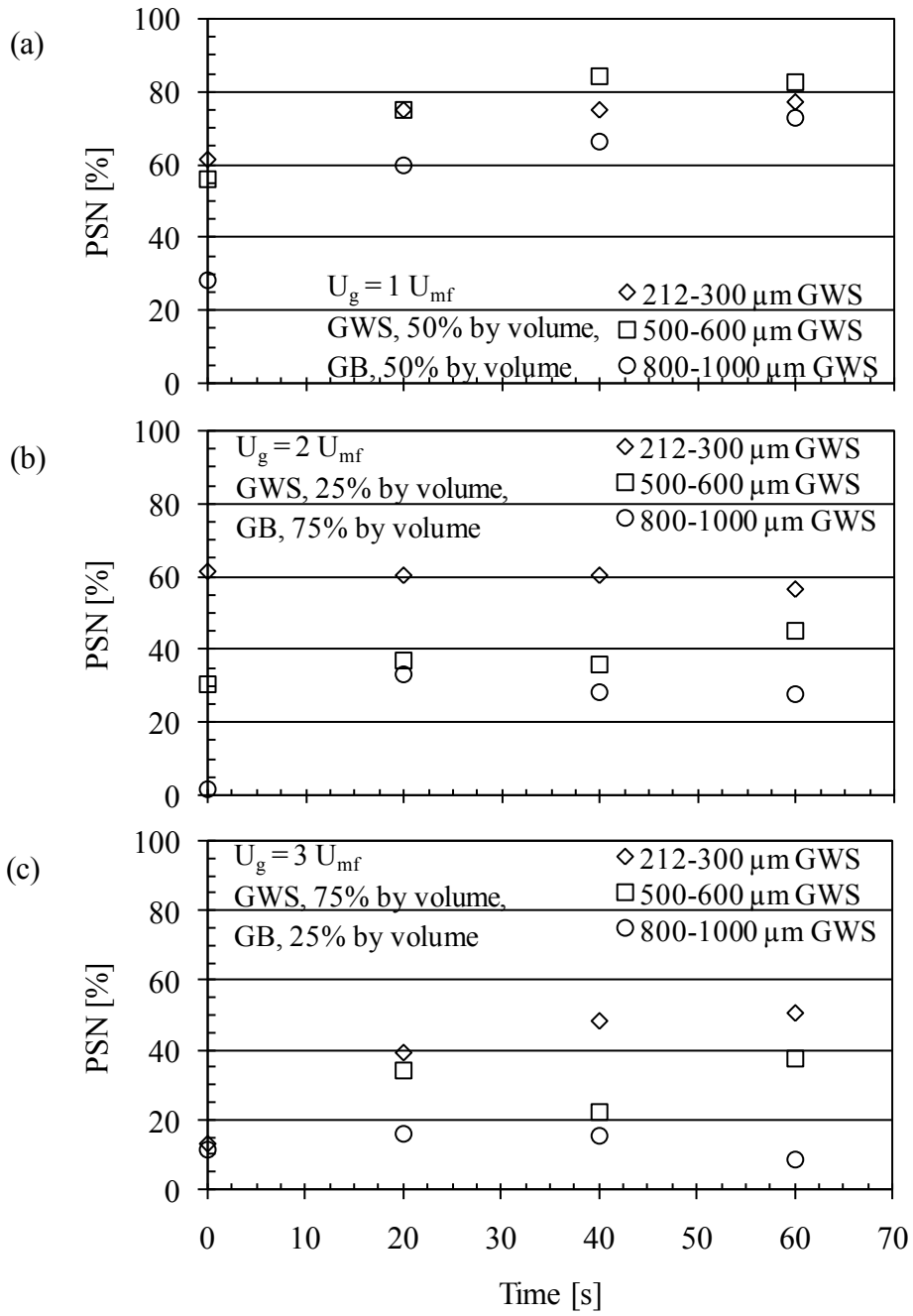

Figure 6.13: PSN of (a) 50% GWS with 50% 500-600 µm GB and fluidized at U_g = 1 U_{mf}, (b) 25% GWS with 75% 500-600 µm GB fluidized at U_g = 2 U_{mf}, and (c) 75% GWS with 25% 500-600 µm GB fluidized at U_g = 3 U_{mf}.

6.5.4 Effect of mixture volume ratio

To determine the effect of the mixture composition on the mixing/segregation behavior, three different mixtures of GWS and GB (percent by volume V_{GWS}/V_{GB} = 25/75, 50/50, and 75/25) are considered for all three particle size ranges of GWS. The superficial gas velocity is set to either U_g = 1, 2, or 3 U_{mf}; U_{mf} being the minimum fluidization velocity for a full bed of glass beads.

The experiments show, that as the portion of less dense particles, i.e. the GWS, is increased, mixing is enhanced. Even for very high GWS content (75% of the bed by volume) the PSN shows very good mixing relative to a lower volume content. Figure 6.14 shows two examples for different mixture ratios, (a) for 212-300 μm GWS particles, and (b) 800-1000 μm GWS particles. The beds do not change significantly after 20 seconds of fluidizing. After 20 seconds, the PSN for different conditions varies within ±10% while the specific value is a function of the GWS particle size range and the superficial gas velocity. In all cases, the higher biomass content promotes mixing. However, with respect to other parameters, a 75% content by volume of biomass may not be desirable for efficient operation of a fluidized bed gasifier.

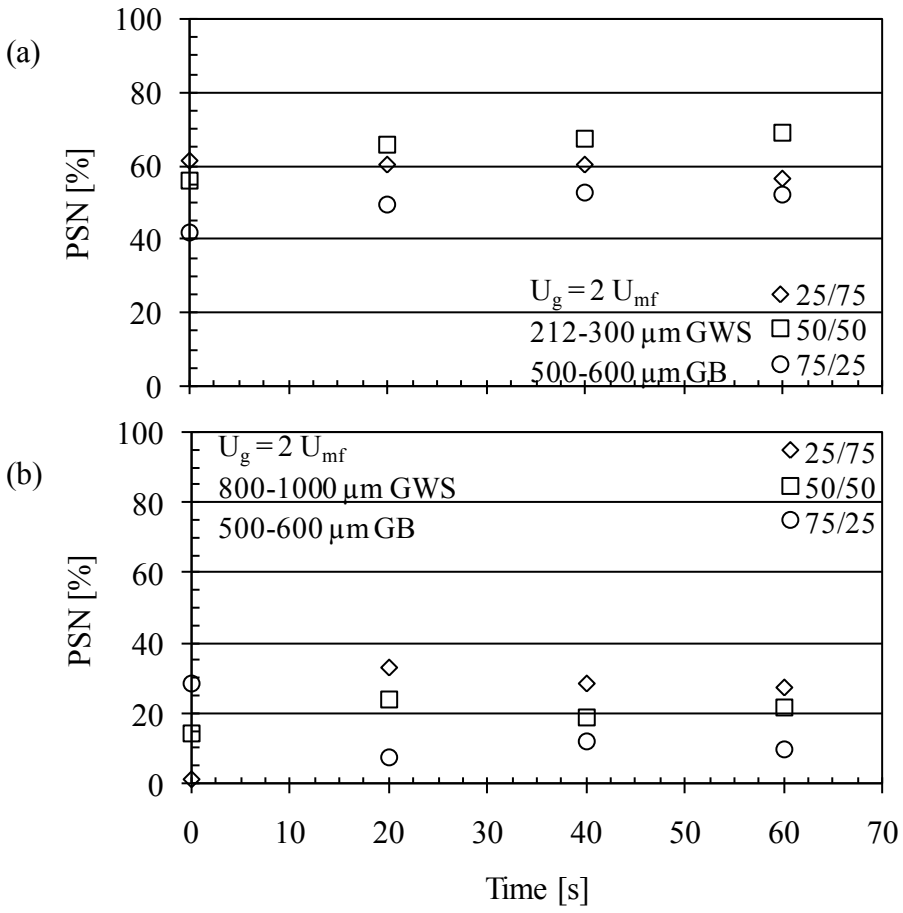

Figure 6.14: PSN for mixture ratios GWS/GB of 25/75, 50/50, and 75/25, fluidized in 20 second intervals at $U_g = 2\ U_{mf}$ with (a) 212-300 µm GWS and (b) 800-1000 µm GWS.

6.5.5 Effect of gas stream humidification

During an initial data acquisition phase using videos to record mixing observations [105], it appeared that humidifying the gas stream can have a significant impact on the mixing/segregation behavior of the bed. Specifically, due to lower static electricity buildup of the particles, the examined beds seemed to segregate more with humidified air compared to dry air. The preliminary experiments only allowed a visual inspection of the particles directly at the reactor wall. Therefore it was sought with CT scans to reveal more information about the internal structure and confirm or disprove earlier findings.

To compare the effect of humidified air, experiments were conducted for dry and humidified fluidization air at three different superficial gas velocities (U_g = 1, 2, and 3 U_{mf}) for mixtures of 25%, 50%, and 75% by volume GWS, for three different GWS particle size ranges. The experiments have been analyzed and the results are presented in terms of the PSN, because only the overall mixedness is of interest in this case.

In terms of PSN, it has been found that of 27 different experimental conditions [105], 8 show that the humidified air causes higher segregation. Of those 8, 6 are with high GWS content (75%) for all particle size ranges, while the other 2 are experiments with 50% GWS content. Figure 6.15 shows two examples of these experiments ((a) 50% 212-300 μm GWS, fluidized at U_g = 1 U_{mf}, and (b) 75% 800-1000 μm GWS, fluidized at U_g = 2 U_{mf}) with dry vs. humidified air, where the humidified air has a higher PSN, indicating higher level of segregation.

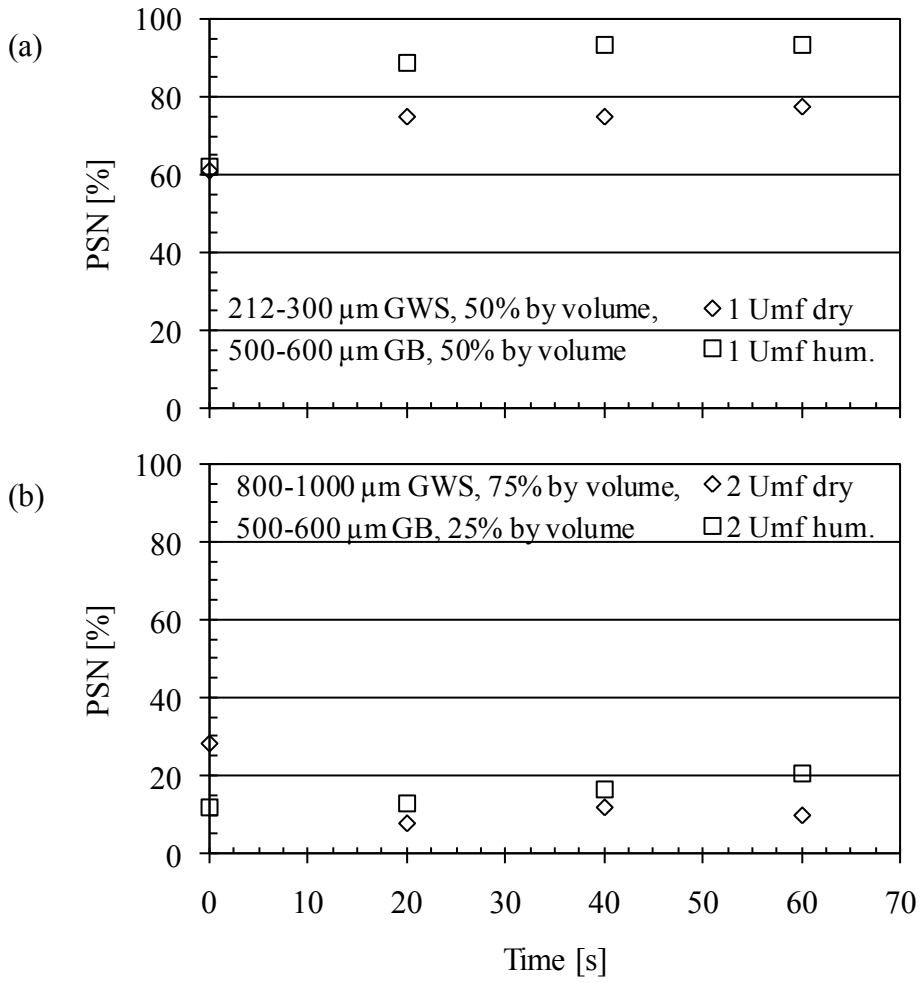

Figure 6.15: PSN for experiments with a) 50% 212-300 µm GWS fluidized with U_g = 1 U_{mf} and b) 75% 800-1000 µm GWS fluidized with U_g = 2 U_{mf}.

As shown in Figure 6.15, the difference in the PSN for humidified vs. dry air is relatively small. Considering that the uncertainty for the PSN can be as high as ±10%, the measured difference between dry vs. humidified air may not be significant. But throughout this study it has also been visually observed [105] that the particles in the fluidized bed can be subject to a significant electrostatic charge buildup and stick to the reactor's plastic walls, and the humidified air significantly reduced this buildup. With these observations and assuming that an electrostatic charge in the fluidized bed may hinder particle segregation, it is reasonable to expect evidence in the experimental data

that humidified air would cause segregation. As shown by [105], the GWS was less prone to charge buildup than another biomass material like ground corn cob. Therefore, the cases that are most likely to show the electrostatic effect would be those with high GWS content and/or low superficial gas velocity, which is exactly what the study shows.

Thus, it is concluded that a humidified gas stream can have an impact on the segregation, especially with particles that are very likely to generate high electrostatic charge buildup. It was found that the humidity does lower the electrostatic charge buildup of the particles in the reactor, which was observed by the amount of particles sticking to the reactor wall, but the differences within a 3D bed are less significant.

6.6 Conclusions

A new and innovative way to study mixing and segregation of particles in a collapsed fluidized bed reactor using X-ray computed tomography has been introduced and the validity and repeatability of the concept has been shown. This allows for non-invasive measurement of 3D particle distribution inside the bed and valuable information about the mixing and segregation behavior can be obtained. The advantage of this approach is that wall-effects can be neglected, particle-particle interaction is not hindered, and flow conditions are 3D, which is observed in industry.

In addition, two analysis tools, the PSN and CA, have been developed, which are useful for characterizing the conditions of a two-component fluidized bed. Experiments have been completed for a variety of parameters important to fluidized bed operation. These are superficial gas velocity, humidification of gas stream, particle size of the model biomass component, and mixture ratio of model biomass to inert bed material.

The data reveal that the two components reach a steady state condition fairly quickly (within 20 to 40 seconds). From all parameters included in this study, the superficial gas velocity had the biggest impact on how well the bed was mixed. Low superficial gas velocity, i.e. just above the minimum superficial gas velocity, causes significant segregation. The level of segregation may depend on other factors, which have also been included in this study. High superficial gas velocity, i.e. a superficial gas velocity in the bubbling regime, mixes the two components. The level of mixedness depends, among other factors, on the magnitude of the superficial gas velocity. Increasing the superficial gas velocity increases the mixedness of the bed. This interrelationship is not linear and so the gained mixedness decreases for equal increases in the superficial gas velocity. The particle size of the model biomass or the particle size to mass ratio impacts mixing. If the lighter particles are bigger than the heavier inert material, they tend to remain mixed; hence light and small particles do not mix well with relatively big and heavy particles, but big and light particles mix well with relatively small and heavy particles. Increasing the ratio of GWS/GB improves particle mixing. A humidified gas stream was found to lower the electrostatic charge buildup of the particles. It is assumed that the electrostatic charge promotes mixing. The extend of this effect depends on other parameters, the particle species or density being the most influential.

6.7 Acknowledgements

Support for portions of the work described in this paper from the Phillips 66 Company is acknowledged.

Chapter 7 Conclusions and Future Work

This section provides an overview of the main conclusions and the academic contributions of this work. In the second part, suggestions are made for continued work based on the experience and understanding gained throughout this project.

7.1 Conclusions

Experiments have been completed for the following parameters important to fluidized bed operation:

- Superficial gas velocity
- Humidification of gas stream
- Particle size of model biomass component
- Mixture ratio of model biomass to inert bed material
- Model biomass species (particle density)
- Vessel size
- Initial condition (mixed, segregated, etc.)

The following conclusions are drawn on multi-component gas-solid fluidized beds.

The two components reach a steady-state condition fairly quickly. Depending on other parameters included in this study, the fluidization time to reach steady state varied between 20 to 60 seconds. This seems to be regardless of all other factors considered.

From all parameters included in this study, the superficial gas velocity has the largest impact on bed mixedness. Low superficial gas velocity, i.e. just above the

minimum superficial gas velocity, causes significant segregation for all conditions considered. The level of segregation highly depends on other factors, which have also been included in this study. High superficial gas velocity, i.e. a superficial gas velocity in the bubbling regime, mixes the two components. The level of mixedness depends, among other factors, on how high the superficial gas velocity is. Increasing the superficial gas velocity increases the mixedness of the bed. This interrelationship is not linear and so for the same increase in superficial gas velocity, the fluidized bed may not show the same improvement in mixedness.

The particle size of the model biomass has an impact on the mixedness of the fluidized bed in a way that, if the lighter particles are bigger, they tend to stay in solution better, while light and small particles with big and heavy particles don't mix well. The effect that bigger particles segregate out on the top, commonly known as the "Brazil Nut Effect" has not been observed in this study, which is due to the significant difference in density of the particles.

It was observed that increasing the mixture ratio of GWS/GB causes the particles to be better mixed on a global scale. This was found for mixtures of 75% GWS with 25% GB, which currently has no practical industrial application.

Comparing the visual results for different sized vessels showed that a bigger vessel promotes mixing, while in the smaller FBR the particles were more easily segregated.

The humidification of the gas stream has also been visually identified to having a significant impact on the mixing/segregation behavior of the fluidized bed. A humidified gas stream was found to significantly lower the electrostatic charge buildup of the

particles. Assuming that it is actually the electrostatic charge that influences the particle mixing, the humidification only has an indirect impact. This effect is independent of other factors, while its extent depends on other parameters, with the particle species or density being the most influential.

The different model biomass particle species that have been studied showed significantly different levels of segregation. Lighter particles segregate out more readily than heavier particles. It was also shown that the particles not only varied in particle density but also in particle shape and porosity. The particle density is assumed to be the most influential particle characteristic, but other factors that have not been included in this study may also have an impact on the mixing/segregation behavior of a particular particle species.

In terms of the initial conditions considered, the results did not show any effect on the condition of the fluidized bed after fluidization. Even for a completely segregated bed, with flotsam material on top of the jetsam particles, the equilibrium stage was reached quickly.

In addition, two new analysis tools have been developed for particulate systems, the PSN and CA, which are useful for characterizing the condition of a two-component fluidized bed.

The preliminary visual observations were useful in determining the parameters of fluidized bed operation that are most influential. All results of the visual observations are in Appendix D. The subsequent X-ray CT scans in the 10.2 cm ID FBR allowed for analyzing bed conditions in more detail and to actually quantify the segregation for

different conditions. To reach this goal, extensive analysis tools were developed, the most significant was quantifying beam hardening in a binary system with an unknown local mass distribution.

7.2 Suggestions for Future Work

Based on the findings throughout this study, the following are suggestions for continuous improvement and development of fluidized bed reactors used for processing biomass.

Since it was found that the two different species of model biomass can show significantly different levels of segregation for otherwise similar conditions, a study should be conducted to identify the cause of these differences. The model biomass used in this study was chosen so that companion simulations could also be completed. It was found that the different model biomass species not only have different densities, but also differ in shape for the same particle size range. This indicates that the biomass preparation process before it is fed into the FBR is important, or different classes of biomass need to be identified to adjust fluidized bed operation accordingly. The parameters that should be investigated in detail include particle density, shape and size distribution. Most experiments revealed that a larger particle size range promoted mixing. Larger particle size though is contrary to what would be expected for optimizing the gasification process. Therefore, it is hypothesized that an optimum exists for each biomass material that balances superficial gas velocity, particle size, and the kinetics of the gasification process for any particular fluidized bed setup. Experiments that address these issues should also be considered.

References

[1] Grohse, E. W., "Analysis of Gas-Fluidized Solid Systems by X-ray Absorption", *AIChE Journal,* 1: 358-365 (1955).

[2] Goldschmidt, M. J. V., Link, J. M., Mellema, S., and Kuipers, J. A. M., "Digital Image Analysis Measurements of Bed Expansion and Segregation Dynamics in Dense Gas-Fluidised Beds", *Powder Technology,* 138: 135-159 (2003).

[3] Halvorsen, B. M., and Arvoh, B., "Minimum Fluidization Velocity, Bubble Behaviour and Pressure Drop in Fluidized Beds with a Range of Particle Sizes", *WIT Transactions on Engineering Sciences*, 63: 227-238 (2009).

[4] Rice, R. W., and Brainovich, J. F. J., "Mixing/Segregation in Two- and Three-Dimensional Fluidized Beds: Binary Systems of Equidensity Spherical Particles", *AIChE Journal,* 32: 7-16 (1986).

[5] Bokkers, G. A., van Sint Annaland, M., and Kuipers, J. A. M., "Mixing and Segregation in a Bidisperse Gas-Solid Fluidised Bed: A Numerical and Experimental Study", *Powder Technology,* 140: 176-186 (2004).

[6] Zhang, Y., Jin, B., W., Z., Ren, B., and Xiao, R., "DEM Simulation of Particle Mixing in Flat-Bottom Spout-Fluid Bed", *Chemical Engineering Research and Design,* 88: 757-771 (2010).

[7] Deng, Z., Xiao, R., Jin, B., Huang, H., Shen, L., Song, Q., and Li, Q., "Computational Fluid Dynamics Modeling of Coal Gasification in a Pressurized Spout-Fluid Bed", *Energy Fuels,* 22: 1560-1569 (2008).

[8] Deza, M., Battaglia, F., and Heindel, T. J., "Approximating a Three Dimensional Fluidized Bed with Two Dimensional Simulations", *Proceedings of the 2008 ASME International Mechanical Engineering Congress and Exposition*, (2008).

[9] Dounit, S., Hemati, M., and Andreux, R., "Modelling and Experimental Validation of a Fluidized-Bed Reactor Freeboard Region: Application to Natural Gas Combustion", *Chemical Engineering Journal,* 140: 457-465 (2008).

[10] Fiorentino, M., Marzocchella, A., and Salatino, P., "Segregation of Fuel Particles and Volatile Matter During Devolatilization in a Fluidized Bed Reactor - I. Model Development", *Chemical Engineering Science,* 52: 1893-1908 (1997).

[11] Gibilaro, L. G., and Rowe, P. N., "A Model for a Segregating Gas Fluidised Bed", *Chemical Engineering Science,* 29: 1403-1412 (1974).

[12] Sundaresan, S., "Modeling the Hydrodynamics of Multiphase Flow Reactors: Current Status and Challenges", *AIChE Journal,* 46: 1102-1105 (2000).

[13] van Sint Annaland, M., Bokkers, G. A., Goldschmidt, M. J. V., Olaofe, O. O., van der Hoef, M. A., and Kuipers, J. A. M., "Development of a Multi-Fluid Model for Poly-Disperse Dense Gas-Solid Fluidised Beds, Part I: Model Derivation and Numerical Implementation", *Chemical Engineering Science,* 64: 4222-4236 (2009).

[14] Heindel, T. J., Gray, J. N., and Jensen, T. C., "An X-ray System for Visualizing Fluid Flows", *Flow Measurement and Instrumentation,* 19: 67-78 (2008).

[15] Heindel, T. J., Hubers, J. L., Jensen, T. C., Gray, J. N., and Striegel, A. C., "Using X-rays for Multiphase Flow Visualization", *2005 ASME Fluids Engineering Division Summer Meeting*, 2005: 2095-2103 (2005).

[16] Franka, N. P., "Visualizing Fluidized Beds with X-rays", *Department of Mechanical Engineering, Iowa State University,* M.S. Thesis: (2008).

[17] Franka, N. P., Drake, J. B., and Heindel, T. J., "Minimum Fluidization Velocity and Gas Holdup in Fluidized Beds with Side Port Air Injection", *2008 Proceedings of the ASME Fluids Engineering Division Summer Conference*, 1: 51-61 (2009).

[18] Franka, N. P., and Heindel, T. J., "Local Time-Averaged Gas Holdup in a Fluidized Bed with Side Air Injection Using X-ray Computed Tomography", *Powder Technology,* 193: 69-78 (2009).

[19] Franka, N. P., Heindel, T. J., and Battaglia, F., "Visualizing Cold-Flow Fluidized Beds with X-rays", *Proceedings of the 2007 ASME International Mechanical Engineering Congress and Exposition,* (2007).

[20] Drake, J. B., and Heindel, T. J., "Repeatability of Gas Holdup in a Fluidized Bed Using X-ray Computed Tomography", *Proceedings of the ASME Fluids Engineering Division Summer Conference 2009*, 1: 1721-1731 (2009).

[21] Drake, J. B., and Heindel, T. J., "Local time-average gas holdup comparisons in cold flow fluidized beds with side-air injection", *Chemical Engineering Science,* 68: 157-165 (2012).

[22] Grace, J. R., Leckner, B., Zhu, J., and Cheng, Y., "Fluidized Beds", *Multiphase Flow Handbook,* 5-1 to 5-93 (2006).

[23] Escudero, D., and Heindel, T. J., "Bed Height and Material Density Effects on Fluidized Bed Hydrodynamics", *Chemical Engineering Science,* 66: 3648-3655 (2011).

[24] Rowe, P. N., and Nienow, A. W., "Minimum Fluidisation Velocity of Multi-Component Particle Mixtures", *Chemical Engineering Science,* 30: 1365-1369 (1975).

[25] Lippens, B. C., and Mulder, J., "Prediction of the Minimum Fluidization Velocity", *Powder Technology,* 75: 67-78 (1993).

[26] Xu, C. C., and Zhu, J., "Prediction of the Minimum Fluidization Velocity for Fine Particles of Various Degrees of Cohesiveness", *Chemical Engineering Communications,* 196: 499-517 (2009).

[27] Christensen, D., Nijenhuis, J., vanOmmen, J. R., and Coppens, M. O., "Influence of Distributed Secondary Gas Injection on the Performance of a Bubbling Fluidized-Bed Reactor", *Industrial & Engineering Chemistry Research,* 47: 3601-3618 (2008).

[28] Dong, S., Cao, C., Si, C., and Guo, Q., "Effect of Perforated Ratios of Distributor on the Fluidization Characteristics in a Gas-Solid Fluidized Bed", *Industrial and Engineering Chemistry Research,* 48: 517-527 (2009).

[29] Fan, X., Parker, D. J., Yang, Z., Seville, J. P. K., and Baeyens, J., "The Effect of Bed Materials on the Solid/Bubble Motion in a Fluidised Bed", *Chemical Engineering Science,* 63: 943-950 (2008).

[30] Macchi, A., Bi, H., Grace, J. R., McKnight, C. A., and Hackman, L., "Effect of gas Density on the Hydrodynamics of Bubble Columns and Three-Phase Fluidized Beds", *Canadian Journal of Chemical Engineering,* 81: 846-852 (2003).

[31] Rowe, P. N., and Yacono, C. X. R., "The Bubbling Behaviour of Fine Powders When Fluidised", *Chemical Engineering Science,* 31: 1179-1192 (1976).

[32] Nienow, A. W., Rowe, P. N., and Chiba, T., "Mixing and Segregation of a Small Proportion of Large Particles in Gas Fluidized Beds of Considerably Smaller Ones", *AIChE Symp Ser,* 74: 45-53 (1978).

[33] Rowe, P. N., Santoro, L., and Yates, J. G., "Division of Gas Between Bubble and Interstitial Phases in Fluidised Beds of Fine Powders", *Chemical Engineering Science,* 33: 133-140 (1978).

[34] Chyang, C.-S., Lieu, K., and Hong, S.-S., "The Effect of Distributor Design on Gas Dispersion in a Bubbling Fluidized Bed", *Journal of the Chinese Institute of Chemical Engineers,* 39: 685-692 (2008).

[35] Dong, S., Si, C., Cao, C., and Guo, Q., "Effect of Perforated Ratio of Distributor on the Fluidization Characteristics in a Gas-Solid Fluidized Bed", *Huaxue*

Fanying Gongcheng Yu Gongyi/Chemical Reaction Engineering and Technology, 24: 433-439 (2008).

[36] Kaewklum, R., and Kuprianov, V. I., "Experimental Studies on a Novel Swirling Fluidized-Bed Combustor Using an Annular Spiral Air Distributor", *Fuel,* 89: 43-52 (2010).

[37] Paiva, J. M., Pinho, C., and Figueiredo, R., "Influence of the Distributor Plate and Operating Conditions on the Fluidization Quality of a Gas Fluidized Bed", *Chemical Engineering Communications,* 196: 342-361 (2009).

[38] Vakhshouri, K., and Grace, J. R., "Effects of the Plenum Chamber Volume and Distributor Geometry on Fluidized Bed Hydrodynamics", *Particuology,* 8: 2-12 (2010).

[39] Wormsbecker, M., Pugsley, T., Van Ommen, J. R., Nijenhuis, J., and Mudde, R., "Effect of Distributor Design on the Bottom Zone Hydrodynamics in a Fluidized Bed Dryer Using 1-D X-ray Densitometry Imaging", *Industrial and Engineering Chemistry Research,* 48: 7004-7015 (2009).

[40] Yan, A., Huang, W., and Zhu, J., "The Influence of Distributor Structure on the Solids Distribution and Flow Development in Circulating Fluidized Beds", *Canadian Journal of Chemical Engineering,* 86: 1023-1031 (2008).

[41] Gilbertson, M. A., and Eames, I., "The Influence of Particle Size on the Flow of Fluidised Powders", *Powder Technology,* 131: 197-205 (2003).

[42] Tortora, P. R., Ceccio, S. L., O'Hern, T. J., Trujillo, S. M., and Torczynski, J. R., "Quantitative measurement of solids distribution in gas-solid riser flows using electrical impedance tomography and gamma densitometry tomography", *International Journal of Multiphase Flow,* 32: 972-995 (2006).

[43] Geldart, D., "Types of Gas Fluidization", *Powder Technology,* 7: 285-292 (1973).

[44] Huilin, L., Yurong, H., Gidaspow, D., Lidan, Y., and Yukun, Q., "Size Segregation of Binary Mixture of Solids in Bubbling Fluidized Beds", *Powder Technology,* 134: 86-97 (2003).

[45] Olivieri, G., Marzocchella, A., and Salatino, P., "Segregation of Fluidized Binary Mixtures of Granular Solids", *AIChE Journal,* 50: 3095-3106 (2004).

[46] Wirsum, M., Fett, F., Iwanowa, N., and Lukjanow, G., "Particle Mixing in Bubbling Fluidized Beds of Binary Particle Systems", *Powder Technology,* 120: 63-69 (2001).

[47] Wu, S. Y., and Baeyens, J., "Segregation by Size Difference in Gas Fluidized Beds", *Powder Technology,* 98: 139-150 (1998).

[48] Gauthier, D., Zerguerras, S., and Flamant, G., "Influence of the Particle Size Distribution of Powders on the Velocities of Minimum and Complete Fluidization", *Chemical Engineering Journal,* 74: 181-196 (1999).

[49] Prasser, H. M., Misawa, M., and Tiseanu, I., "Comparison Between Wire-Mesh Sensor and Ultra-Fast X-ray Tomograph for an Air-Water Flow in a Vertical Pipe", *Flow Measurement and Instrumentation,* 16: 73-83 (2005).

[50] Boyer, C., Duquenne, A.-M., and Wild, G., "Measuring Techniques in Gas-Liquid and Gas-Liquid-Solid Reactors", *Chemical Engineering Science,* 57: 3185-3215 (2002).

[51] Heindel, T. J., "A Review of X-Ray Flow Visualization With Applications to Multiphase Flows", *Journal of Fluids Engineering - Transactions of the ASME,* 133: 074001 (2011).

[52] Chaouki, J., Larachi, F., and Dudukovic, M. P., "Noninvasive Tomographic and Velocimetric Monitoring of Multiphase Flows", *Industrial & Engineering Chemistry Research,* 36: 4476-4503 (1997).

[53] Drake, J. B., Franka, N. P., and Heindel, T. J., "Developing X-ray Particle Tracking Velocimetry for Applications in Fluidized Beds", *ASME International Mechanical Engineering Congress and Exposition, Proceedings*, 10: 379-386 (2009).

[54] Drake, J. B., Tang, L., and Heindel, T. J., "X-ray Particle Tracking Velocimetry in Fluidized Beds", *Proceedings of the ASME Fluids Engineering Division Summer Conference 2009*, 1: 1733-1742 (2009).

[55] Herman, G. T., "Image Reconstruction from Projections", *Real-Time Imaging,* 1: 3-3 (1995).

[56] Iatrou, M., De Man, B., Khare, K., and Benson, T. M., "A 3D Study Comparing Filtered Backprojection, Weighted Least Squares, and Penalized Weighted Least Squares for CT Reconstruction", *Nuclear Science Symposium Conference Record, 2007. NSS '07. IEEE*, 4: 2639-2643 (2007).

[57] Herman, G. T., and Davidi, R., "Image Reconstruction from a Small Number of Projections", *Inverse Problems,* 24: (2008).

[58] Lin, X., Luo, S., Wang, L., He, S., and Chen, G., "An Experimental Study on DBP and Hilbert Filtering Method for Tomography Reconstruction", *Proceedings -*

2010 3rd International Congress on Image and Signal Processing, CISP 2010, 6: 2737-2741 (2010).

[59] Wu, C., Cheng, Y., Ding, Y., Wei, F., and Jin, Y., "A Novel X-ray Computed Tomography Method for Fast Measurement of Multiphase Flow", *Chemical Engineering Science,* 62: 4325-4335 (2007).

[60] Shepp, L. A., and Logan Jr, B. F., "Fourier Reconstruction of a Head Section", *IEEE Transactions on Nuclear Science,* NS-21: 21-43 (1974).

[61] Sutherland, J. P., and Wong, K. Y., "Some Segregation Effects in Packed-Fluidized Beds", *Canadian Journal of Chemical Engineering,* 42: 163-167 (1964).

[62] Rowe, P. N., and Nienow, A. W., "Particle Mixing and Segregation in Gas Fluidised Beds. A Review", *Powder Technology,* 15: 141-147 (1976).

[63] Nienow, A. W., Rowe, P. N., and Cheung, L. Y. L., "A Quantitative Analysis of the Mixing of Two Segregating Powders of Different Density in a Gas-Fluidised Bed", *Powder Technology,* 20: 89-97 (1978).

[64] Baeyens, J., and Geldart, D., "Particle Mixing in a Gas Fluidized Bed", *Proceedings of the International Symposium of Fluidization and its Applications,* 182-195 (1974).

[65] García-Ochoa, F., Romero, A., Villar, J. C., and Bello, A., "A Study of Segregation in a Gas-Solid Fluidized Bed: Particles of Different Density", *Powder Technology,* 58: 169-174 (1989).

[66] Rowe, P. N., Nienow, A. W., and Agbim, A. J., "A Preliminary Quantitative Study of Particle Segregation in Gas Fluidised Beds - Binary Systems of Near Spherical Particles", *Transactions of the Institution of Chemical Engineers,* 50: 324-333 (1972).

[67] Almuttahar, A., and Taghipour, F., "Computational Fluid Dynamics of a Circulating Fluidized Bed under Various Fluidization Conditions", *Chemical Engineering Science,* 63: 1696-1709 (2008).

[68] Beetstra, R., van der Hoef, M. A., and Kuipers, J. A. M., "Numerical Study of Segregation Using a New Drag Force Correlation for Polydisperse Systems Derived from Lattice-Boltzmann Simulations", *Chemical Engineering Science,* 62: 246-255 (2007).

[69] Cheng, Y., and Zhu, J., "Hydrodynamics and Scale-Up of Liquid-Solid Circulating Fluidized Beds: Similitude Method vs. CFD", *Chemical Engineering Science,* 63: 3201-3211 (2008).

[70] Deza, M., Battaglia, F., and Heindel, T. J., "Computational Modeling of Biomass in a Fluidized Bed Gasifier", *Proceedings of the 2007 ASME International Mechanical Engineering Congress and Exposition*, (2007).

[71] Deza, M., Battaglia, F., and Heindel, T. J., "A Validation Study for the Hydrodynamics of Biomass in a Fluidized Bed", *Proceedings of the 2008 ASME Fluids Engineering Division Summer Meeting*, (2008).

[72] Deza, M., Franka, N. P., Heindel, T. J., and Battaglia, F., "CFD Modeling and X-ray Imaging of Biomass in a Fluidized Bed", *Journal of Fluids Engineering - Transactions of the ASME,* 131: 111303 (2009).

[73] Feng, Y. Q., Xu, B. H., Zhang, S. J., Yu, A. B., and Zulli, P., "Discrete Particle Simulation of Gas Fluidization of Particle Mixtures", *AIChE Journal,* 50: 1713-1728 (2004).

[74] Fuentes, M., Scenna, N. J., Aguirre, P. A., and Mussati, M. C., "Hydrodynamic Aspects in Anaerobic Fluidized Bed Reactor Modeling", *Chemical Engineering and Processing: Process Intensification,* 47: 1530-1540 (2008).

[75] Hadavand, A., Jalali, A. A., and Famouri, P., "An Innovative Bed Temperature-Oriented Modeling and Robust Control of a Circulating Fluidized Bed Combustor", *Chemical Engineering Journal,* 140: 497-508 (2008).

[76] Hoomans, B. P. B., Kuipers, J. A. M., and Van Swaaij, W. P. M., "Granular Dynamics Simulation of Segregation Phenomena in Bubbling Gas-Fluidised Beds", *Powder Technology,* 109: 41-48 (2000).

[77] Huilin, L., Yunhua, Z., Ding, J., Gidaspow, D., and Wei, L., "Investigation of Mixing/Segregation of Mixture Particles in Gas-Solid Fluidized Beds", *Chemical Engineering Science,* 62: 301-317 (2007).

[78] Huilin, L., Yurong, H., and Gidaspow, D., "Hydrodynamic Modelling of Binary Mixture in a Gas Bubbling Fluidized Bed Using the Kinetic Theory of Granular Flow", *Chemical Engineering Science,* 58: 1197-1205 (2003).

[79] Joshi, J. B., and Ranade, V. V., "Computational Fluid Dynamics for Designing Process Equipment: Expectations, Current Status, and Path Forward", *Industrial and Engineering Chemistry Research,* 42: 1115-1128 (2003).

[80] Min, J., Drake, J. B., Heindel, T. J., and Fox, R. O., "Experimental Validation of CFD Simulations of a Lab-Scale Fluidized-Bed Reactor With and Without Side-Gas Injection", *AIChE Journal,* 56: 1434-1446 (2009).

[81] Patel, B. K., Ramirez, W. F., and Galvin, K. P., "A Generalized Segregation and Dispersion Model for Liquid-Fluidized Beds", *Chemical Engineering Science,* 63: 1415-1427 (2008).

[82] Prasser, H. M., "Novel Experimental Measuring Techniques Required to Provide Data for CFD Validation", *Nuclear Engineering and Design,* 238: 744-770 (2008).

[83] Toye, D., Marchot, P., Crine, M., and L'Homme, G., "Modelling of Multiphase Flow in Packed Beds by Computer-Assisted X-ray Tomography", *Measurement Science and Technology,* 7: 436-443 (1996).

[84] van Sint Annaland, M., Bokkers, G. A., Goldschmidt, M. J. V., Olaofe, O. O., van der Hoef, M. A., and Kuipers, J. A. M., "Development of a Multi-Fluid Model for Poly-Disperse Dense Gas-Solid Fluidised Beds, Part II: Segregation in Binary Particle Mixtures", *Chemical Engineering Science,* 64: 4237-4246 (2009).

[85] Kak, A. C., and Slaney, M., "Principles of Computerized Tomographic Imaging", (1988).

[86] Balat, M., "Biomass Energy and Biochemical Conversion Processing for Fuels and Chemicals", *Energy Sources, Part A: Recovery, Utilization, and Environmental Effects,* 28: 517 - 525 (2006).

[87] Balat, M., Acici, N., and Ersoy, G., "Trends in the Use of Biomass as an Energy Source", *Energy Sources, Part B: Economics, Planning, and Policy,* 1: 367 - 378 (2006).

[88] Brown, R. C., "Biorenewable Resources", Iowa State Press (2003).

[89] Demirbas, A., "Biomass Resource Facilities and Biomass Conversion Processing for Fuels and Chemicals", *Energy Conversion and Management,* 42: 1357-1378 (2001).

[90] Kaygusuz, K., "Hydropower and Biomass as Renewable Energy Sources in Turkey", *Energy Sources, Part A: Recovery, Utilization, and Environmental Effects,* 23: 775 - 799 (2001).

[91] Kelly-Yong, T. L., Lee, K. T., Mohamed, A. R., and Bhatia, S., "Potential of Hydrogen from Oil Palm Biomass as a Source of Renewable Energy Worldwide", *Energy Policy,* 35: 5692-5701 (2007).

[92] Searcy, E., Flynn, P., Ghafoori, E., and Kumar, A., "The Relative Cost of Biomass Energy Transport", *Applied Biochemistry and Biotechnology,* 137-140: 639-652 (2007).

[93] Formisani, B., Girimonte, R., and Vivacqua, V., "Fluidization of Mixtures of Two Solids Differing in Density or Size", *AIChE Journal,* 57: 2325-2333 (2010).

[94] Das, M., Meikap, B. C., and Saha, R. K., "Characteristics of Axial and Radial Segregation of Single and Mixed Particle System Based on Terminal Settling Velocity in the Riser of a Circulating Fluidized Bed", *Chemical Engineering Journal,* 145: 32-43 (2008).

[95] Shen, L., Xiao, J., Niklasson, F., and Johnsson, F., "Biomass Mixing in a Fluidized Bed Biomass Gasifier for Hydrogen Production", *Chemical Engineering Science,* 62: 636-643 (2007).

[96] Van Ommen, J. R., and Mudde, R. F., "Measuring the Gas-Solids Distribution in Fluidized Beds - A Review", *International Journal of Chemical Reactor Engineering,* 6, R3: (2008).

[97] Yang, S. C., "Density Effect on Mixing and Segregation Processes in a Vibrated Binary Granular Mixture", *Powder Technology,* 164: 65-74 (2006).

[98] Zhang, Y., Jin, B., and Zhong, W., "Fluidization, Mixing and Segregation of a Biomass-Sand Mixture in a Fluidized Bed", *International Journal of Chemical Reactor Engineering,* 6, A88: (2008).

[99] Zhang, Y., Jin, B., and Zhong, W., "Experimental Investigation on Mixing and Segregation Behavior of Biomass Particle in Fluidized Bed", *Chemical Engineering and Processing: Process Intensification,* 48: 745-754 (2009).

[100] Guardiola, J., Rojo, V., and Ramos, G., "Influence of Particle Size, Fluidization Velocity and Relative Humidity on Fluidized Bed Electrostatics", *Journal of Electrostatics,* 37: 1-20 (1996).

[101] Naimer, N. S., Chiba, T., and Nienow, A. W., "Parameter Estimation for a Solids Mixing/Segregation Model for Gas Fluidised Beds", *Chemical Engineering Science,* 37: 1047-1057 (1982).

[102] Rees, A. C., Davidson, J. F., Dennis, J. S., S Fennell, P., Gladden, L. F., Hayhurst, A. N., Mantle, M. D., Muller, C. R., and Sederman, A. J., "The Nature of the Flow Just Above the Perforated Plate Distributor of a Gas-Fluidised Bed, as Imaged Using Magnetic Resonance", *Chemical Engineering Science,* 61: 6002-6015 (2006).

[103] Sahoo, A., and Roy, G. K., "Segregation Characteristics of Irregular Binaries in Gas Solid Fluidized Beds--An ANN-Approach", *Particuology,* 6: 199-206 (2008).

[104] Torquato, S., "Random Heterogeneous Materials: Microstructure and Macroscopic Properties", Springer-Verlag (2002).

[105] Keller, N. K. G., "Mixing and Segregation in 3D Multi-Component Two-Phase Fluidized Beds", *Department of Mechanical Engineering, Iowa State University,* Ph.D. Dissertation: (2012).

[106] Deza, M., Heindel, T. J., and Battaglia, F., "Effects of Mixing using Side Port Air Injection on a Biomass Fluidized Bed", *Journal of Fluids Engineering - Transactions of the ASME,* 133: 111302 (2011).

[107] Min, J., Drake, J. B., Heindel, T. J., and Fox, R. O., "Experimental Validation of CFD Simulations of a Lab-Scale Fluidized-Bed Reactor With and Without Side-Gas Injection", *AIChE Journal,* 56: 1434-1446 (2010).

[108] Drake, J. B., and Heindel, T. J., "The Repeatability and Uniformity of 3D Fluidized Beds", *Powder Technology,* 213: 148-154 (2011).

[109] Bai, W., Keller, N. K. G., Heindel, T. J., and Fox, R. O., "Numerical Study of Mixing and Segregation in a Biomass Fluidized Bed", *Powder Technology,* , under review: (2012).

[110] Keller, N. K. G., Bai, W., Fox, R. O., and Heindel, T. J., "Quantifying Mixing in 3D Multi-Component Particulate Systems", *Chemical Engineering Science,* , under review: (2012).

[111] Formisani, B., Cristofaro, G. D., and Girimonte, R., "A Fundamental Approach to the Phenomenology of Fluidization of Size Segregating Binary Mixtures of Solids", *Chemical Engineering Science,* 56: 109-119 (2001).

[112] Formisani, B., Girimonte, R., and Longo, T., "The Fluidization Process of Binary Mixtures of Solids: Development of the Approach Based on the Fluidization Velocity Interval", *Powder Technology,* 185: 97-108 (2008).

[113] Marzocchella, A., Salatino, P., Di Pastena, V., and Lirer, L., "Transient Fluidization and Segregation of Binary Mixtures of Particles", *AIChE Journal,* 46: 2175-2182 (2000).

Appendix A: Other Analysis Tools (Feature Extraction)

To characterize a fluidized bed in terms of mixing over several dimensions, the amount of information from the 3D images must be condensed. This section will give an overview of other various analysis tools considered for this study.

(A) Material Distribution Over Bed Height

Since it is expected that the particles will mainly segregate in vertical layers with lighter particles floating on the top, a reasonable characterization of a fluidized bed is to illustrate the material distribution as a function of bed height. For this, data are extracted as the average GWS content per slice and the result plotted in a graph for a single bed. Figure A. 1 shows a sample plot for GWS content per slice in percent for a bed of 50% 500-600 μm GWS mixed with 50% GB after fluidizing in 20 second increments (starting at initially well-mixed) with dry air flow rate of $U_g = 1\ U_{mf}$ for GB.

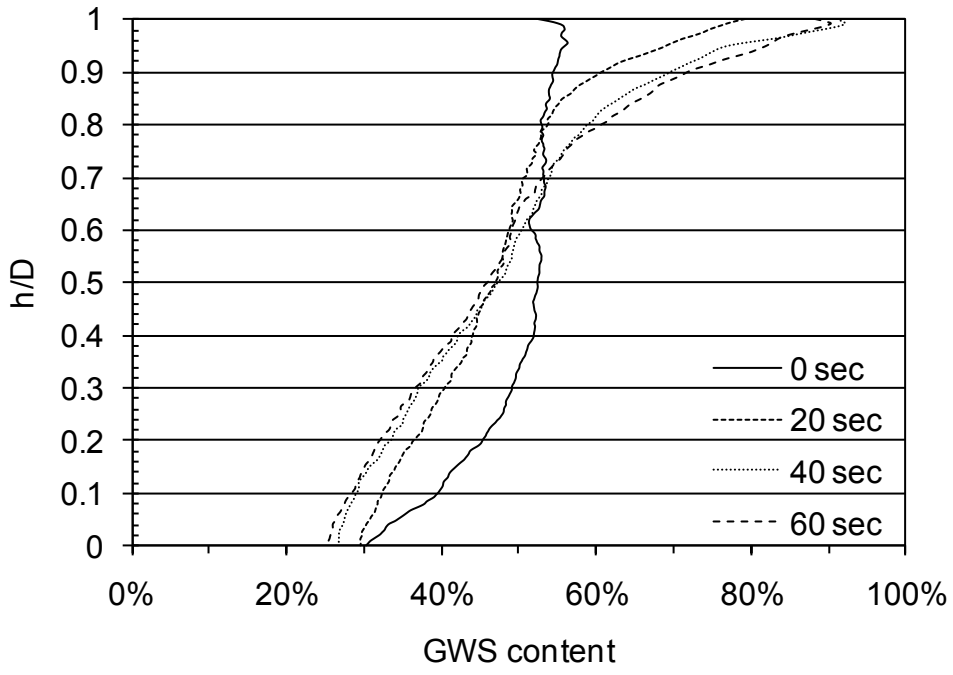

Figure A. 1: Example of GWS content over bed height: 50% 500-600 µm GWS with 50% GB initially well-mixed, fluidized in 20 second intervals for a total fluidization time of 60 seconds with $U_g = 1\ U_{mf}$.

The GWS content per slice was evaluated using the material content image. Every voxel for one slice is considered and the average value calculated. Figure A. 1 demonstrates how much the well-mixed initial condition can also vary locally, illustrated by the solid line for 0 sec. The top part of the fluidized bed is very close to 50% while towards the bottom the GWS content decreases. As the bed is fluidized with a low superficial gas velocity ($U_g = 1\ U_{mf}$) causing segregation, over time the GWS particles move towards the top of the bed, illustrated by higher GWS content in the upper region of the bed vs. a lower GWS content in the lower part for the lines of 20, 40 and 60 seconds of fluidizing.

It shows that while the GWS content over bed height gives valuable insight, the change over time cannot be illustrated as easily and thus a more condensed form of information for fluidized beds is sought.

(B) Average Height

The average height analysis is evaluated using the binary image [2]. For every voxel within the bed, whether it represents GB or GWS, its height above the distributor is determined, and then the average height over the whole bed is calculated for each material. Thus, this analysis yields two numbers per image, or for each condition. It is clear that for a perfectly mixed bed these two numbers would be the same, exactly 0.5, regardless of the material content ratio. A sample data set is illustrated in Figure A. 2, which shows the result of the average height analysis for a bed of 50% 500-600 μm GWS mixed with 50% GB. The bed is initially in a well-mixed condition, marked by both average heights being close to 0.5, and then fluidized with humidified air at $U_g = 1\ U_{mf}$ in 20 second intervals. The advantage of this analysis is that it can be used to illustrate time resolved data.

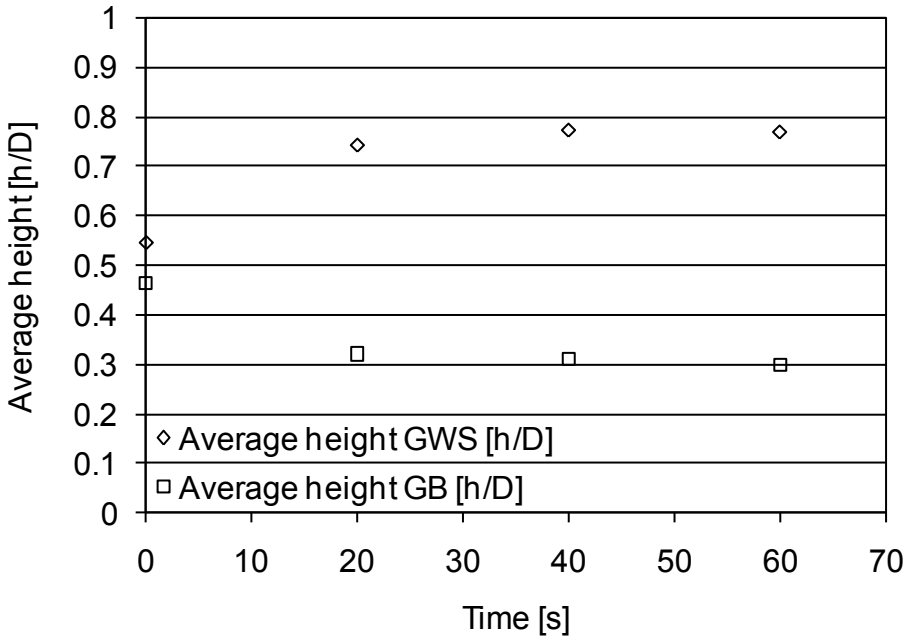

Figure A. 2: Result of average height analysis for a bed of 50% 500-600 µm GWS mixed with 50% GB. The bed was initially well-mixed and was then fluidized with humidified air at $U_g = 1\ U_{mf}$ in 20 second intervals.

The average heights for a perfectly separated bed depend on the material ratio and are listed in Table A.1. For flotsam material the average dimensionless bed height, h_F/D, when perfectly separated is calculated as:

$$\frac{h_F}{D} = \frac{1}{2} * x_{FV} + x_{JV} \tag{7.1}$$

where x_{FV} and x_{JV} are the volume fraction of the flotsam and jetsam material, and h_f and h_j are the flotsam and jetsam average heights, respectively. For a perfectly separated bed, the average dimensionless bed height for jetsam is:

$$\frac{h_J}{D} = \frac{1}{2} * x_{JV} \tag{7.2}$$

Table A. 1: Average dimensionless bed heights [h/D] for GWS and GB for perfectly separated beds.

Material ratio	25% GWS/ 75% GB	50% GWS/ 50% GB	75% GWS/ 25% GB
Average height GWS [h/D]	0.88	0.75	0.63
Average height GB [h/D]	0.38	0.25	0.13

Appendix B: Particle Segregation Number (PSN) – Results from Multiple Experiments

The following tables list the results for repeated experiments in terms of the Particle Segregation Number (PSN) and the associated standard deviation. This is to document the repeatability of the experimental procedures.

Table B. 1: PSN results from repeated experiments with 50% 500-600 µm GWS and 50% 500-600 µm GB at $U_g = 1\ U_{mf}$ with dry air.

Time [s]	0	20	40	60
Set 01 (PSN [%])	56	75	84	83
Set 02 (PSN [%])	36	57	73	78
Set 03 (PSN [%])	44	64	79	84
Set 04 (PSN [%])	29	67	77	84
Set 05 (PSN [%])	45	62	75	84
Average (PSN [%])	42	65	78	83
Standard Deviation	9.1	6.1	3.9	2.3

Table B. 2: PSN results from repeated experiments with 50% 500-600 µm GWS and 50% 500-600 µm GB at $U_g = 2\ U_{mf}$ with dry air.

Time [s]	0	20	40	60
Set 01 (PSN [%])	34	47	43	49
Set 02 (PSN [%])	45	38	35	34
Set 03 (PSN [%])	40	28	28	40
Set 04 (PSN [%])	22	41	42	40
Set 05 (PSN [%])	33	48	43	36
Average (PSN [%])	35	40	38	40
Standard Deviation	7.7	7.3	6.0	5.1

Table B. 3: PSN results from repeated experiments with 50% 500-600 µm GWS and 50% 500-600 µm GB at $U_g = 3\ U_{mf}$ with dry air.

Time [s]	0	20	40	60
Set 01 (PSN [%])	24	31	43	42
Set 02 (PSN [%])	15	24	40	35
Set 03 (PSN [%])	28	42	17	25
Set 04 (PSN [%])	35	33	34	31
Set 05 (PSN [%])	28	35	31	31
Average (PSN [%])	26	33	33	33
Standard Deviation	6.8	5.9	9.0	5.5

Appendix C: Cube Analysis (CA) - Results from Multiple Experiments

The following tables list the results for repeated experiments in terms of the Cube Analysis (CA). This is to document the repeatability of the experimental procedures.

Table C. 1: CA results from Set 01 and Set 02 of repeated experiments with 50% 500-600 µm GWS and 50% 500-600 µm GB, fluidized at U_g = 1 U_{mf} with dry air, for cubes with side length 1, 10, 20, 30, 40, and 50; initial condition and after 20 seconds of fluidizing.

Set 01							Set 02						
Initial condition, 0 seconds, U_g = 1 U_{mf}							Initial condition, 0 seconds, U_g = 1 U_{mf}						
bin \ cube	1	10	20	30	40	50	bin \ cube	1	10	20	30	40	50
0	1.33	0.07	0.00	0.00	0.00	0.00	0	1.13	0.25	0.29	0.00	0.00	0.00
0.1	1.66	1.68	1.74	4.76	1.22	0.00	0.1	1.13	1.03	0.72	0.00	0.00	0.00
0.2	8.84	4.61	4.65	5.29	4.88	0.00	0.2	8.31	2.40	2.73	0.57	4.94	0.00
0.3	3.89	10.27	12.21	12.17	14.63	25.00	0.3	4.28	10.66	9.34	12.50	19.75	5.71
0.4	30.31	29.10	26.60	26.98	36.59	38.89	0.4	36.67	49.35	59.48	63.07	66.67	85.71
0.5	43.76	49.81	52.91	50.79	42.68	36.11	0.5	38.75	32.63	26.72	23.86	8.64	8.57
0.6	7.53	3.96	1.89	0.00	0.00	0.00	0.6	7.34	3.41	0.72	0.00	0.00	0.00
0.7	1.32	0.49	0.00	0.00	0.00	0.00	0.7	1.11	0.26	0.00	0.00	0.00	0.00
0.8	0.26	0.02	0.00	0.00	0.00	0.00	0.8	0.17	0.02	0.00	0.00	0.00	0.00
0.9	0.59	0.00	0.00	0.00	0.00	0.00	0.9	0.64	0.00	0.00	0.00	0.00	0.00
1	0.54	0.00	0.00	0.00	0.00	0.00	1	0.47	0.00	0.00	0.00	0.00	0.00
20 seconds, U_g = 1 U_{mf}							20 seconds, U_g = 1 U_{mf}						
bin \ cube	1	10	20	30	40	50	bin \ cube	1	10	20	30	40	50
0	1.86	0.49	0.00	0.00	0.00	0.00	0	6.28	5.06	4.35	1.70	3.85	2.86
0.1	2.99	2.73	2.79	6.25	2.44	0.00	0.1	2.87	3.19	3.48	3.41	3.85	0.00
0.2	15.91	10.74	12.21	13.02	14.63	12.82	0.2	11.21	5.20	6.82	6.82	7.69	8.57
0.3	5.41	17.99	19.12	18.75	21.95	28.21	0.3	4.68	13.89	13.50	19.89	29.49	25.71
0.4	29.45	28.81	29.26	30.73	32.93	30.77	0.4	29.72	37.45	44.85	42.61	39.74	40.00
0.5	27.74	24.95	25.15	20.83	17.07	15.38	0.5	25.97	19.49	13.64	13.07	10.26	5.71
0.6	6.95	5.90	5.44	5.21	6.10	7.69	0.6	5.90	3.29	2.32	2.27	5.13	0.00
0.7	3.34	2.78	2.21	2.08	3.66	2.56	0.7	2.67	3.29	4.35	1.70	0.00	14.29
0.8	0.90	2.34	2.50	3.13	1.22	2.56	0.8	0.98	2.84	1.02	3.41	0.00	2.86
0.9	2.60	3.05	1.32	0.00	0.00	0.00	0.9	4.90	6.24	5.66	5.11	0.00	0.00
1	2.85	0.21	0.00	0.00	0.00	0.00	1	4.79	0.05	0.00	0.00	0.00	0.00

Table C. 2: CA results from Set 01 and Set 02 of repeated experiments with 50% 500-600 µm GWS and 50% 500-600 µm GB, fluidized at U_g = 1 U_{mf} with dry air, for cubes with side length 1, 10, 20, 30, 40, and 50; after 40 and 60 seconds of fluidizing.

Set 01							Set 02						
40 seconds, U_g = 1 U_{mf}							40 seconds, U_g = 1 U_{mf}						
cube / bin	1	10	20	30	40	50	cube / bin	1	10	20	30	40	50
0	2.43	0.49	0.00	0.52	0.00	0.00	0	6.70	5.37	5.22	2.84	3.85	2.86
0.1	3.96	4.63	3.77	6.77	3.75	0.00	0.1	4.49	5.40	5.37	5.11	6.41	5.71
0.2	18.03	13.89	16.96	18.23	15.00	17.95	0.2	19.38	11.52	12.77	13.07	16.67	11.43
0.3	5.45	15.94	18.41	17.71	28.75	23.08	0.3	6.55	22.74	22.93	28.98	35.90	28.57
0.4	23.50	21.15	20.29	18.75	18.75	17.95	0.4	25.04	25.64	27.43	23.86	20.51	17.14
0.5	24.13	23.03	21.74	18.75	20.00	23.08	0.5	14.11	8.00	4.35	1.70	0.00	14.29
0.6	8.55	8.30	7.83	10.94	11.25	7.69	0.6	3.13	2.08	1.89	2.27	3.85	0.00
0.7	5.14	4.66	5.22	1.56	2.50	7.69	0.7	1.70	1.88	4.50	3.98	3.85	5.71
0.8	1.29	2.95	2.17	5.21	0.00	2.56	0.8	0.68	2.21	2.32	7.95	7.69	14.29
0.9	2.86	4.66	3.62	1.56	0.00	0.00	0.9	6.46	11.62	12.63	10.23	1.28	0.00
1	4.65	0.32	0.00	0.00	0.00	0.00	1	11.75	3.54	0.58	0.00	0.00	0.00
60 seconds, U_g = 1 U_{mf}							60 seconds, U_g = 1 U_{mf}						
cube / bin	1	10	20	30	40	50	cube / bin	1	10	20	30	40	50
0	2.46	0.57	0.15	1.56	0.00	0.00	0	7.68	5.99	5.96	4.55	6.41	2.86
0.1	4.68	5.29	5.81	8.33	4.88	2.63	0.1	7.05	8.58	8.43	6.25	14.10	8.57
0.2	20.54	16.01	16.28	16.15	19.51	23.68	0.2	26.54	19.84	21.95	21.59	21.79	25.71
0.3	5.26	17.13	21.22	20.83	21.95	23.68	0.3	6.85	23.20	26.16	30.68	25.64	22.86
0.4	23.06	21.11	20.49	19.79	21.95	15.79	0.4	17.39	12.05	7.99	2.27	6.41	0.00
0.5	19.62	17.03	15.70	15.10	15.85	18.42	0.5	5.90	2.77	1.31	3.41	6.41	0.00
0.6	8.08	7.85	7.70	7.29	4.88	5.26	0.6	1.34	0.95	1.74	5.68	2.56	11.43
0.7	5.32	4.72	4.94	3.65	9.76	5.26	0.7	1.31	2.59	4.51	4.55	3.85	14.29
0.8	1.30	3.36	3.49	4.17	1.22	5.26	0.8	0.66	2.49	3.78	2.27	3.85	8.57
0.9	3.66	5.89	4.22	3.13	0.00	0.00	0.9	10.70	17.06	16.86	18.75	8.97	5.71
1	6.01	1.05	0.00	0.00	0.00	0.00	1	14.58	4.49	1.31	0.00	0.00	0.00

Table C. 3: CA results from Set 03 and Set 04 of repeated experiments with 50% 500-600 µm GWS and 50% 500-600 µm GB, fluidized at U_g = 1 U_{mf} with dry air, for cubes with side length 1, 10, 20, 30, 40, and 50; initial condition and after 20 seconds of fluidizing.

Set 03							Set 04						
Initial condition, 0 seconds, U_g = 1 U_{mf}							Initial condition, 0 seconds, U_g = 1 U_{mf}						
bin \ cube	1	10	20	30	40	50	bin \ cube	1	10	20	30	40	50
0	0.92	0.10	0.00	0.00	0.00	0.00	0	0.66	0.02	0.00	0.00	0.00	0.00
0.1	1.12	0.94	1.02	0.00	0.00	0.00	0.1	0.76	0.29	0.15	0.00	0.00	0.00
0.2	7.97	2.41	2.05	0.58	4.00	0.00	0.2	7.33	1.72	0.74	0.00	0.00	0.00
0.3	3.99	10.07	8.78	6.36	14.67	14.71	0.3	3.63	9.21	9.43	6.36	13.51	12.50
0.4	35.89	46.70	53.73	60.69	62.67	55.88	0.4	34.18	44.21	52.87	60.12	71.62	59.38
0.5	40.13	35.44	33.38	31.79	18.67	29.41	0.5	41.98	39.77	35.20	33.53	14.86	28.13
0.6	7.27	3.61	1.02	0.58	0.00	0.00	0.6	8.76	4.14	1.62	0.00	0.00	0.00
0.7	1.17	0.69	0.00	0.00	0.00	0.00	0.7	1.27	0.54	0.00	0.00	0.00	0.00
0.8	0.24	0.03	0.00	0.00	0.00	0.00	0.8	0.19	0.10	0.00	0.00	0.00	0.00
0.9	0.65	0.00	0.00	0.00	0.00	0.00	0.9	0.62	0.00	0.00	0.00	0.00	0.00
1	0.65	0.00	0.00	0.00	0.00	0.00	1	0.61	0.00	0.00	0.00	0.00	0.00
20 seconds, U_g = 1 U_{mf}							20 seconds, U_g = 1 U_{mf}						
bin \ cube	1	10	20	30	40	50	bin \ cube	1	10	20	30	40	50
0	5.62	3.91	2.90	1.70	4.11	0.00	0	5.28	3.45	2.76	1.14	0.00	0.00
0.1	5.08	5.71	6.82	3.98	4.11	5.71	0.1	5.22	5.84	6.24	5.68	9.72	5.88
0.2	18.00	10.62	9.43	11.36	12.33	17.14	0.2	16.29	9.76	9.29	9.66	13.89	14.71
0.3	5.89	19.50	24.09	26.70	39.73	25.71	0.3	5.39	16.99	21.77	23.86	26.39	26.47
0.4	26.10	28.91	31.20	29.55	20.55	25.71	0.4	25.29	29.73	30.19	29.55	30.56	20.59
0.5	17.08	12.02	7.26	5.68	4.11	2.86	0.5	19.20	14.55	10.74	8.52	5.56	11.76
0.6	4.23	2.47	2.76	5.68	5.48	8.57	0.6	5.98	4.01	3.77	3.41	2.78	5.88
0.7	1.90	2.30	2.90	3.41	6.85	2.86	0.7	2.85	2.37	3.05	7.39	6.94	0.00
0.8	0.78	2.15	1.89	3.41	1.37	8.57	0.8	1.07	2.54	2.61	3.41	4.17	14.71
0.9	5.48	10.12	10.74	8.52	1.37	2.86	0.9	4.35	8.36	9.43	7.39	0.00	0.00
1	9.83	2.30	0.00	0.00	0.00	0.00	1	9.07	2.40	0.15	0.00	0.00	0.00

Table C. 4: CA results from Set 03 and Set 04 of repeated experiments with 50% 500-600 µm GWS and 50% 500-600 µm GB, fluidized at U_g = 1 U_{mf} with dry air, for cubes with side length 1, 10, 20, 30, 40, and 50; after 40 and 60 seconds of fluidizing.

Set 03							Set 04						
40 seconds, U_g = 1 U_{mf}							40 seconds, U_g = 1 U_{mf}						
bin \ cube	1	10	20	30	40	50	bin \ cube	1	10	20	30	40	50
0	7.78	6.19	5.08	2.84	5.48	2.94	0	6.42	4.45	3.51	1.72	2.74	0.00
0.1	7.70	8.47	9.58	10.23	10.96	8.82	0.1	7.43	8.68	10.67	7.47	9.59	11.76
0.2	26.16	20.57	21.19	21.02	28.77	29.41	0.2	25.41	18.87	18.27	23.56	32.88	26.47
0.3	6.12	20.84	23.51	23.86	21.92	20.59	0.3	6.61	22.39	26.61	28.16	20.55	23.53
0.4	16.66	13.31	11.18	7.95	4.11	0.00	0.4	19.35	15.94	12.72	5.75	9.59	5.88
0.5	7.14	3.41	2.03	4.55	10.96	2.94	0.5	7.64	3.37	2.19	6.32	6.85	0.00
0.6	1.82	1.15	2.32	5.11	1.37	8.82	0.6	1.66	1.16	3.07	3.45	0.00	5.88
0.7	1.36	1.75	3.63	1.70	2.74	8.82	0.7	1.21	2.17	2.78	1.72	4.11	11.76
0.8	0.73	2.82	3.34	6.82	1.37	14.71	0.8	0.57	2.58	2.19	4.02	4.11	8.82
0.9	6.59	15.36	16.84	15.91	12.33	2.94	0.9	6.91	14.72	16.08	17.82	9.59	5.88
1	17.95	6.14	1.31	0.00	0.00	0.00	1	16.79	5.68	1.90	0.00	0.00	0.00
60 seconds, U_g = 1 U_{mf}							60 seconds, U_g = 1 U_{mf}						
bin \ cube	1	10	20	30	40	50	bin \ cube	1	10	20	30	40	50
0	8.74	6.68	6.25	4.00	6.94	5.88	0	8.76	6.17	5.41	4.00	5.56	2.94
0.1	11.46	13.42	13.81	13.71	20.83	14.71	0.1	10.53	13.17	14.77	11.43	16.67	14.71
0.2	30.10	26.67	28.92	28.57	34.72	35.29	0.2	26.80	22.78	24.71	27.43	30.56	26.47
0.3	4.77	15.23	14.68	16.57	4.17	5.88	0.3	5.34	17.02	16.96	14.86	13.89	17.65
0.4	8.99	4.19	3.05	0.00	0.00	0.00	0.4	12.21	7.81	5.26	6.86	4.17	0.00
0.5	2.85	1.05	2.03	0.57	5.56	0.00	0.5	5.18	2.87	3.36	1.71	4.17	2.94
0.6	0.88	1.10	1.02	2.29	5.56	0.00	0.6	1.58	1.23	1.61	4.57	8.33	8.82
0.7	1.28	2.33	1.45	4.57	6.94	5.88	0.7	1.71	2.69	3.07	5.14	2.78	5.88
0.8	0.75	2.52	2.62	7.43	2.78	23.53	0.8	0.90	3.03	4.68	8.00	4.17	17.65
0.9	9.56	19.46	24.13	22.29	12.50	8.82	0.9	7.17	17.61	18.86	16.00	9.72	2.94
1	20.61	7.36	2.03	0.00	0.00	0.00	1	19.82	5.63	1.32	0.00	0.00	0.00

Table C. 5: CA results from Set 05 and the average over all sets of repeated experiments with 50% 500-600 µm GWS and 50% 500-600 µm GB, fluidized at U_g = 1 U_{mf} with dry air, for cubes with side length 1, 10, 20, 30, 40, and 50; initial condition and after 20 seconds of fluidizing.

Set 05							Average						
Initial condition, 0 seconds, U_g = 1 U_{mf}							Initial condition, 0 seconds, U_g = 1 U_{mf}						
bin \ cube	1	10	20	30	40	50	bin \ cube	1	10	20	30	40	50
0	0.92	0.13	0.15	0.00	0.00	0.00	0	0.99	0.11	0.09	0.00	0.00	0.00
0.1	1.08	0.79	0.58	0.00	0.00	0.00	0.1	1.15	0.95	0.84	0.95	0.24	0.00
0.2	7.99	2.41	2.33	0.57	2.63	0.00	0.2	8.09	2.71	2.50	1.40	3.29	0.00
0.3	3.94	9.75	10.04	8.00	18.42	16.13	0.3	3.95	9.99	9.96	9.08	16.20	14.81
0.4	36.41	46.71	53.13	65.14	63.16	64.52	0.4	34.69	43.21	49.16	55.20	60.14	60.88
0.5	39.93	36.24	32.46	26.29	15.79	19.35	0.5	40.91	38.78	36.13	33.25	20.13	24.31
0.6	6.95	3.22	1.31	0.00	0.00	0.00	0.6	7.57	3.67	1.31	0.12	0.00	0.00
0.7	1.03	0.69	0.00	0.00	0.00	0.00	0.7	1.18	0.54	0.00	0.00	0.00	0.00
0.8	0.21	0.05	0.00	0.00	0.00	0.00	0.8	0.21	0.04	0.00	0.00	0.00	0.00
0.9	0.64	0.00	0.00	0.00	0.00	0.00	0.9	0.63	0.00	0.00	0.00	0.00	0.00
1	0.89	0.00	0.00	0.00	0.00	0.00	1	0.63	0.00	0.00	0.00	0.00	0.00
20 seconds, U_g = 1 U_{mf}							20 seconds, U_g = 1 U_{mf}						
bin \ cube	1	10	20	30	40	50	bin \ cube	1	10	20	30	40	50
0	3.73	1.91	1.30	0.57	0.00	0.00	0	4.55	2.96	2.26	1.02	1.59	0.57
0.1	4.50	4.51	5.06	3.41	5.48	5.88	0.1	4.13	4.40	4.88	4.55	5.12	3.50
0.2	18.34	11.63	10.98	11.36	17.81	8.82	0.2	15.95	9.59	9.75	10.45	13.27	12.41
0.3	5.95	20.49	22.69	25.57	30.14	44.12	0.3	5.46	17.77	20.23	22.95	29.54	30.04
0.4	28.18	30.80	31.94	31.82	28.77	8.82	0.4	27.75	31.14	33.49	32.85	30.51	25.18
0.5	17.80	12.09	9.25	5.11	2.74	17.65	0.5	21.56	16.62	13.21	10.64	7.95	10.67
0.6	4.51	2.69	3.47	5.68	2.74	2.94	0.6	5.51	3.67	3.55	4.45	4.44	5.02
0.7	2.04	1.94	3.03	6.25	10.96	2.94	0.7	2.56	2.54	3.11	4.17	5.68	4.53
0.8	0.87	2.57	2.89	2.27	1.37	5.88	0.8	0.92	2.49	2.18	3.13	1.63	6.92
0.9	5.14	9.33	9.39	7.95	0.00	2.94	0.9	4.50	7.42	7.31	5.80	0.27	1.16
1	8.93	2.03	0.00	0.00	0.00	0.00	1	7.10	1.40	0.03	0.00	0.00	0.00

Table C. 6: CA results from Set 05 and the average over all sets of repeated experiments with 50% 500-600 μm GWS and 50% 500-600 μm GB, fluidized at $U_g = 1\ U_{mf}$ with dry air, for cubes with side length 1, 10, 20, 30, 40, and 50; after 40 and 60 seconds of fluidizing.

Set 05							Average						
40 seconds, $U_g = 1\ U_{mf}$							40 seconds, $U_g = 1\ U_{mf}$						
cube / bin	1	10	20	30	40	50	cube / bin	1	10	20	30	40	50
0	5.35	3.84	3.21	1.70	1.39	0.00	0	5.73	4.07	3.40	1.93	2.69	1.16
0.1	6.41	6.70	6.71	3.98	9.72	5.71	0.1	6.00	6.77	7.22	6.71	8.09	6.40
0.2	25.69	19.83	20.26	23.86	27.78	28.57	0.2	22.93	16.94	17.89	19.95	24.22	22.77
0.3	7.08	22.61	26.82	29.55	31.94	25.71	0.3	6.36	20.90	23.66	25.65	27.81	24.30
0.4	20.74	18.04	15.45	9.66	8.33	2.86	0.4	21.06	18.81	17.41	13.19	12.26	8.77
0.5	8.10	3.64	3.50	4.55	4.17	5.71	0.5	12.22	8.29	6.76	7.17	8.39	9.20
0.6	2.04	1.49	1.60	2.27	0.00	5.71	0.6	3.44	2.83	3.34	4.81	3.29	5.62
0.7	1.52	1.84	1.75	2.84	1.39	14.29	0.7	2.19	2.46	3.57	2.36	2.92	9.66
0.8	0.77	2.49	2.62	5.68	6.94	11.43	0.8	0.81	2.61	2.53	5.94	4.02	10.36
0.9	8.06	15.18	17.64	15.91	8.33	0.00	0.9	6.18	12.31	13.36	12.28	6.31	1.76
1	14.25	4.33	0.44	0.00	0.00	0.00	1	13.08	4.00	0.84	0.00	0.00	0.00
60 seconds, $U_g = 1\ U_{mf}$							60 seconds, $U_g = 1\ U_{mf}$						
cube / bin	1	10	20	30	40	50	cube / bin	1	10	20	30	40	50
0	7.71	6.15	6.28	3.43	6.94	5.88	0	7.07	5.11	4.81	3.51	5.17	3.51
0.1	9.20	10.13	10.51	11.43	12.50	11.76	0.1	8.59	10.12	10.67	10.23	13.80	10.48
0.2	30.06	26.80	27.74	27.43	38.89	29.41	0.2	26.81	22.42	23.92	24.23	29.09	28.11
0.3	5.55	16.57	17.52	19.43	8.33	14.71	0.3	5.55	17.83	19.31	20.47	14.80	16.96
0.4	11.83	7.38	5.84	1.14	1.39	0.00	0.4	14.70	10.51	8.53	6.01	6.78	3.16
0.5	4.32	2.27	2.04	1.14	4.17	0.00	0.5	7.57	5.20	4.89	4.39	7.23	4.27
0.6	1.24	1.03	1.02	5.14	11.11	2.94	0.6	2.62	2.43	2.62	4.99	6.49	5.69
0.7	1.52	2.08	2.77	5.71	1.39	11.76	0.7	2.23	2.88	3.35	4.72	4.94	8.62
0.8	0.82	3.25	5.11	6.29	1.39	20.59	0.8	0.89	2.93	3.93	5.63	2.68	15.12
0.9	7.81	18.12	20.00	18.86	13.89	2.94	0.9	7.78	15.63	16.81	15.80	9.02	4.08
1	19.93	6.22	1.17	0.00	0.00	0.00	1	16.19	4.95	1.17	0.00	0.00	0.00

Table C. 7: CA results from Set 01 and Set 02 of repeated experiments with 50% 500-600 µm GWS and 50% 500-600 µm GB, fluidized at $U_g = 2\ U_{mf}$ with dry air, for cubes with side length 1, 10, 20, 30, 40, and 50; initial condition and after 20 seconds of fluidizing.

Set 01							Set 02						
Initial condition, 0 seconds, $U_g = 2\ U_{mf}$							Initial condition, 0 seconds, $U_g = 2\ U_{mf}$						
bin \ cube	1	10	20	30	40	50	bin \ cube	1	10	20	30	40	50
0	0.77	0.00	0.00	0.00	0.00	0.00	0	1.28	0.40	0.29	0.00	0.00	0.00
0.1	0.59	0.14	0.00	0.55	0.00	0.00	0.1	1.39	1.30	1.30	0.00	1.23	0.00
0.2	6.74	1.51	0.73	6.01	0.00	0.00	0.2	7.68	2.70	2.60	2.30	2.47	0.00
0.3	3.84	8.14	8.88	5.46	16.67	0.00	0.3	3.57	10.17	9.54	13.22	18.52	9.38
0.4	34.41	42.00	46.43	40.44	52.78	57.14	0.4	33.90	42.30	48.41	46.55	54.32	62.50
0.5	41.24	41.59	41.78	45.90	30.56	42.86	0.5	43.22	39.72	36.85	37.93	23.46	28.13
0.6	8.29	5.48	2.04	1.64	0.00	0.00	0.6	6.26	2.63	1.01	0.00	0.00	0.00
0.7	2.32	0.91	0.15	0.00	0.00	0.00	0.7	1.14	0.75	0.00	0.00	0.00	0.00
0.8	0.39	0.23	0.00	0.00	0.00	0.00	0.8	0.26	0.03	0.00	0.00	0.00	0.00
0.9	0.84	0.00	0.00	0.00	0.00	0.00	0.9	0.63	0.00	0.00	0.00	0.00	0.00
1	0.57	0.00	0.00	0.00	0.00	0.00	1	0.66	0.00	0.00	0.00	0.00	0.00
20 seconds, $U_g = 2\ U_{mf}$							20 seconds, $U_g = 2\ U_{mf}$						
bin \ cube	1	10	20	30	40	50	bin \ cube	1	10	20	30	40	50
0	2.38	0.65	0.28	1.01	0.00	0.00	0	1.54	0.46	0.14	0.00	0.00	0.00
0.1	2.39	2.01	1.70	3.52	1.30	0.00	0.1	1.94	1.46	1.30	0.00	0.00	0.00
0.2	12.82	5.97	6.09	8.04	7.79	6.67	0.2	11.14	5.10	5.06	2.86	4.88	2.94
0.3	4.90	15.33	15.58	11.56	15.58	3.33	0.3	4.47	12.79	12.14	13.71	23.17	14.71
0.4	30.10	36.03	39.52	42.71	50.65	53.33	0.4	31.01	40.56	48.12	49.71	62.20	64.71
0.5	32.45	30.72	32.44	32.16	24.68	36.67	0.5	33.20	29.61	27.60	30.86	7.32	17.65
0.6	10.16	8.26	4.39	1.01	0.00	0.00	0.6	11.67	8.27	5.64	2.86	2.44	0.00
0.7	3.18	0.92	0.00	0.00	0.00	0.00	0.7	3.14	1.49	0.00	0.00	0.00	0.00
0.8	0.26	0.10	0.00	0.00	0.00	0.00	0.8	0.35	0.27	0.00	0.00	0.00	0.00
0.9	0.84	0.00	0.00	0.00	0.00	0.00	0.9	0.86	0.00	0.00	0.00	0.00	0.00
1	0.53	0.00	0.00	0.00	0.00	0.00	1	0.67	0.00	0.00	0.00	0.00	0.00

Table C. 8: CA results from Set 01 and Set 02 of repeated experiments with 50% 500-600 µm GWS and 50% 500-600 µm GB, fluidized at $U_g = 2\ U_{mf}$ with dry air, for cubes with side length 1, 10, 20, 30, 40, and 50; after 40 and 60 seconds of fluidizing.

Set 01							Set 02						
40 seconds, $U_g = 2\ U_{mf}$							40 seconds, $U_g = 2\ U_{mf}$						
cube / bin	1	10	20	30	40	50	cube / bin	1	10	20	30	40	50
0	1.79	0.31	0.14	0.53	0.00	0.00	0	1.93	0.56	0.29	0.00	0.00	0.00
0.1	1.97	1.81	1.00	5.29	0.00	0.00	0.1	2.39	2.30	2.17	0.57	1.23	0.00
0.2	11.45	5.14	5.13	6.35	5.26	3.33	0.2	11.11	5.65	6.07	3.98	6.17	3.03
0.3	4.77	12.70	14.67	9.52	19.74	13.33	0.3	3.89	11.97	11.71	10.80	23.46	12.12
0.4	31.50	37.87	40.74	41.80	52.63	60.00	0.4	28.86	34.87	41.33	53.98	54.32	60.61
0.5	35.63	35.34	36.04	36.51	22.37	23.33	0.5	35.30	36.43	36.56	30.68	14.81	24.24
0.6	9.14	6.05	2.28	0.00	0.00	0.00	0.6	12.63	7.74	1.88	0.00	0.00	0.00
0.7	2.30	0.75	0.00	0.00	0.00	0.00	0.7	2.67	0.45	0.00	0.00	0.00	0.00
0.8	0.23	0.03	0.00	0.00	0.00	0.00	0.8	0.21	0.03	0.00	0.00	0.00	0.00
0.9	0.71	0.00	0.00	0.00	0.00	0.00	0.9	0.62	0.00	0.00	0.00	0.00	0.00
1	0.52	0.00	0.00	0.00	0.00	0.00	1	0.39	0.00	0.00	0.00	0.00	0.00
60 seconds, $U_g = 2\ U_{mf}$							60 seconds, $U_g = 2\ U_{mf}$						
cube / bin	1	10	20	30	40	50	cube / bin	1	10	20	30	40	50
0	2.30	0.71	0.28	0.52	0.00	0.00	0	1.89	0.55	0.14	0.00	0.00	0.00
0.1	2.49	2.08	2.12	5.24	1.30	0.00	0.1	2.20	2.11	1.59	0.00	1.20	0.00
0.2	13.46	6.89	5.64	9.42	10.39	6.67	0.2	12.07	5.82	5.64	3.41	4.82	3.03
0.3	4.89	14.25	15.37	14.14	20.78	10.00	0.3	4.68	13.55	13.29	14.77	22.89	15.15
0.4	28.69	33.46	35.26	27.75	36.36	40.00	0.4	29.48	37.36	47.83	52.84	48.19	66.67
0.5	32.56	33.97	37.94	41.36	31.17	43.33	0.5	32.49	30.59	26.16	26.70	22.89	15.15
0.6	10.97	7.32	3.24	1.57	0.00	0.00	0.6	12.08	8.39	5.20	2.27	0.00	0.00
0.7	3.09	1.15	0.14	0.00	0.00	0.00	0.7	3.12	1.19	0.14	0.00	0.00	0.00
0.8	0.34	0.17	0.00	0.00	0.00	0.00	0.8	0.26	0.41	0.00	0.00	0.00	0.00
0.9	0.79	0.00	0.00	0.00	0.00	0.00	0.9	0.77	0.02	0.00	0.00	0.00	0.00
1	0.42	0.00	0.00	0.00	0.00	0.00	1	0.96	0.00	0.00	0.00	0.00	0.00

Table C. 9: CA results from Set 03 and Set 04 of repeated experiments with 50% 500-600 μm GWS and 50% 500-600 μm GB, fluidized at $U_g = 2\ U_{mf}$ with dry air, for cubes with side length 1, 10, 20, 30, 40, and 50; initial condition and after 20 seconds of fluidizing.

Set 03							Set 04						
Initial condition, 0 seconds, $U_g = 2\ U_{mf}$							Initial condition, 0 seconds, $U_g = 2\ U_{mf}$						
bin \ cube	1	10	20	30	40	50	bin \ cube	1	10	20	30	40	50
0	0.82	0.02	0.00	0.00	0.00	0.00	0	0.75	0.00	0.00	0.00	0.00	0.00
0.1	1.15	0.54	0.15	0.00	0.00	0.00	0.1	0.92	0.47	0.29	0.00	0.00	0.00
0.2	8.41	3.10	2.76	0.57	1.32	0.00	0.2	7.28	2.00	1.75	0.00	1.33	0.00
0.3	3.96	10.13	11.61	10.34	19.74	21.88	0.3	3.33	8.27	7.89	4.60	10.67	6.06
0.4	33.06	39.88	44.85	49.43	53.95	46.88	0.4	35.01	45.27	53.07	66.09	72.00	72.73
0.5	41.59	41.63	39.04	39.08	25.00	31.25	0.5	43.21	41.01	36.70	29.31	16.00	21.21
0.6	8.23	4.16	1.45	0.57	0.00	0.00	0.6	7.01	2.40	0.29	0.00	0.00	0.00
0.7	1.41	0.51	0.15	0.00	0.00	0.00	0.7	0.86	0.46	0.00	0.00	0.00	0.00
0.8	0.28	0.03	0.00	0.00	0.00	0.00	0.8	0.21	0.12	0.00	0.00	0.00	0.00
0.9	0.65	0.00	0.00	0.00	0.00	0.00	0.9	0.68	0.00	0.00	0.00	0.00	0.00
1	0.44	0.00	0.00	0.00	0.00	0.00	1	0.74	0.00	0.00	0.00	0.00	0.00
20 seconds, $U_g = 2\ U_{mf}$							20 seconds, $U_g = 2\ U_{mf}$						
bin \ cube	1	10	20	30	40	50	bin \ cube	1	10	20	30	40	50
0	1.31	0.15	0.00	0.00	0.00	0.00	0	1.22	0.13	0.00	0.00	0.00	0.00
0.1	1.73	1.25	0.85	0.00	1.30	0.00	0.1	1.87	1.18	0.72	0.00	0.00	0.00
0.2	10.87	4.55	3.56	2.22	2.60	0.00	0.2	11.94	5.74	5.21	2.29	8.00	0.00
0.3	4.50	13.19	14.51	9.44	22.08	15.15	0.3	4.58	14.12	16.21	13.71	20.00	18.18
0.4	33.04	40.82	44.52	57.78	58.44	69.70	0.4	30.30	34.69	38.78	41.14	46.67	57.58
0.5	35.16	32.46	33.85	28.89	15.58	15.15	0.5	34.34	34.95	35.75	41.71	24.00	24.24
0.6	9.23	6.77	2.70	1.67	0.00	0.00	0.6	11.76	8.50	3.33	1.14	1.33	0.00
0.7	2.50	0.68	0.00	0.00	0.00	0.00	0.7	2.62	0.62	0.00	0.00	0.00	0.00
0.8	0.24	0.12	0.00	0.00	0.00	0.00	0.8	0.29	0.07	0.00	0.00	0.00	0.00
0.9	0.79	0.00	0.00	0.00	0.00	0.00	0.9	0.62	0.00	0.00	0.00	0.00	0.00
1	0.64	0.00	0.00	0.00	0.00	0.00	1	0.47	0.00	0.00	0.00	0.00	0.00

Table C. 10: CA results from Set 03 and Set 04 of repeated experiments with 50% 500-600 µm GWS and 50% 500-600 µm GB, fluidized at $U_g = 2\ U_{mf}$ with dry air, for cubes with side length 1, 10, 20, 30, 40, and 50; after 40 and 60 seconds of fluidizing.

Set 03							Set 04						
40 seconds, $U_g = 2\ U_{mf}$							40 seconds, $U_g = 2\ U_{mf}$						
cube / bin	1	10	20	30	40	50	cube / bin	1	10	20	30	40	50
0	1.61	0.40	0.14	0.00	0.00	0.00	0	0.99	0.08	0.00	0.00	0.00	0.00
0.1	1.88	1.56	1.58	0.00	0.00	0.00	0.1	1.35	0.91	0.14	0.00	0.00	0.00
0.2	10.79	3.80	3.17	0.56	5.33	0.00	0.2	11.91	4.15	3.62	0.00	6.67	0.00
0.3	4.30	13.45	13.38	10.67	12.00	9.09	0.3	5.09	15.35	16.81	14.94	20.00	14.71
0.4	31.09	38.37	42.45	52.81	69.33	75.76	0.4	30.93	35.71	39.13	47.13	45.33	61.76
0.5	34.62	32.68	34.39	32.02	13.33	15.15	0.5	33.91	34.45	37.10	35.63	28.00	23.53
0.6	10.65	7.69	4.32	3.93	0.00	0.00	0.6	11.29	8.26	3.04	2.30	0.00	0.00
0.7	3.22	1.73	0.58	0.00	0.00	0.00	0.7	3.13	1.01	0.14	0.00	0.00	0.00
0.8	0.34	0.29	0.00	0.00	0.00	0.00	0.8	0.30	0.07	0.00	0.00	0.00	0.00
0.9	0.93	0.03	0.00	0.00	0.00	0.00	0.9	0.71	0.00	0.00	0.00	0.00	0.00
1	0.57	0.00	0.00	0.00	0.00	0.00	1	0.39	0.00	0.00	0.00	0.00	0.00
60 seconds, $U_g = 2\ U_{mf}$							60 seconds, $U_g = 2\ U_{mf}$						
cube / bin	1	10	20	30	40	50	cube / bin	1	10	20	30	40	50
0	1.67	0.54	0.29	0.00	0.00	0.00	0	1.16	0.25	0.00	0.00	0.00	0.00
0.1	2.15	1.92	1.88	0.00	2.63	0.00	0.1	1.59	1.14	0.72	0.00	0.00	0.00
0.2	11.47	5.39	5.63	2.89	5.26	2.94	0.2	11.39	4.40	4.35	2.31	5.33	0.00
0.3	4.42	12.75	13.71	11.56	15.79	17.65	0.3	4.99	13.48	14.06	13.87	18.67	24.24
0.4	30.48	37.55	41.85	53.76	55.26	55.88	0.4	31.94	39.47	46.38	53.76	54.67	51.52
0.5	34.82	32.68	31.60	29.48	21.05	23.53	0.5	33.46	32.44	30.58	29.48	21.33	24.24
0.6	10.88	7.90	4.62	2.31	0.00	0.00	0.6	10.33	7.52	3.62	0.58	0.00	0.00
0.7	2.44	1.05	0.43	0.00	0.00	0.00	0.7	3.14	1.07	0.29	0.00	0.00	0.00
0.8	0.25	0.20	0.00	0.00	0.00	0.00	0.8	0.29	0.18	0.00	0.00	0.00	0.00
0.9	0.78	0.02	0.00	0.00	0.00	0.00	0.9	0.88	0.03	0.00	0.00	0.00	0.00
1	0.64	0.00	0.00	0.00	0.00	0.00	1	0.81	0.00	0.00	0.00	0.00	0.00

Table C. 11: CA results from Set 05 and the average over all sets of repeated experiments with 50% 500-600 μm GWS and 50% 500-600 μm GB, fluidized at $U_g = 2\ U_{mf}$ with dry air, for cubes with side length 1, 10, 20, 30, 40, and 50; initial condition and after 20 seconds of fluidizing.

Set 05							Average						
Initial condition, 0 seconds, $U_g = 2\ U_{mf}$							Initial condition, 0 seconds, $U_g = 2\ U_{mf}$						
bin \ cube	1	10	20	30	40	50	bin \ cube	1	10	20	30	40	50
0	0.97	0.05	0.00	0.00	0.00	0.00	0	0.92	0.09	0.06	0.00	0.00	0.00
0.1	1.15	0.89	0.87	0.00	0.00	0.00	0.1	1.04	0.67	0.52	0.11	0.25	0.00
0.2	7.95	2.32	2.03	0.57	4.00	0.00	0.2	7.61	2.33	1.98	1.89	1.82	0.00
0.3	4.00	9.26	9.59	6.29	12.00	12.12	0.3	3.74	9.20	9.50	7.98	15.52	9.89
0.4	36.23	47.38	52.91	66.29	68.00	66.67	0.4	34.52	43.37	49.13	53.76	60.21	61.18
0.5	39.00	35.64	33.87	26.86	16.00	21.21	0.5	41.65	39.92	37.65	35.82	22.20	28.93
0.6	7.97	4.03	0.73	0.00	0.00	0.00	0.6	7.55	3.74	1.10	0.44	0.00	0.00
0.7	1.48	0.42	0.00	0.00	0.00	0.00	0.7	1.44	0.61	0.06	0.00	0.00	0.00
0.8	0.20	0.00	0.00	0.00	0.00	0.00	0.8	0.27	0.08	0.00	0.00	0.00	0.00
0.9	0.61	0.00	0.00	0.00	0.00	0.00	0.9	0.68	0.00	0.00	0.00	0.00	0.00
1	0.44	0.00	0.00	0.00	0.00	0.00	1	0.57	0.00	0.00	0.00	0.00	0.00
20 seconds, $U_g = 2\ U_{mf}$							20 seconds, $U_g = 2\ U_{mf}$						
bin \ cube	1	10	20	30	40	50	bin \ cube	1	10	20	30	40	50
0	1.37	0.22	0.14	0.00	0.00	0.00	0	1.56	0.32	0.11	0.20	0.00	0.00
0.1	1.86	1.66	1.01	0.00	0.00	0.00	0.1	1.96	1.51	1.12	0.70	0.52	0.00
0.2	12.21	4.90	5.34	2.31	7.79	0.00	0.2	11.80	5.25	5.05	3.54	6.21	1.92
0.3	4.76	14.75	14.57	13.87	18.18	21.88	0.3	4.64	14.04	14.60	12.46	19.80	14.65
0.4	30.43	36.25	40.40	46.82	55.84	50.00	0.4	30.98	37.67	42.27	47.63	54.76	59.06
0.5	33.52	32.02	34.49	35.26	18.18	28.13	0.5	33.74	31.95	32.83	33.78	17.95	24.37
0.6	11.41	8.89	3.90	1.73	0.00	0.00	0.6	10.85	8.14	3.99	1.68	0.75	0.00
0.7	2.81	1.19	0.14	0.00	0.00	0.00	0.7	2.85	0.98	0.03	0.00	0.00	0.00
0.8	0.19	0.12	0.00	0.00	0.00	0.00	0.8	0.27	0.13	0.00	0.00	0.00	0.00
0.9	0.75	0.00	0.00	0.00	0.00	0.00	0.9	0.77	0.00	0.00	0.00	0.00	0.00
1	0.67	0.00	0.00	0.00	0.00	0.00	1	0.60	0.00	0.00	0.00	0.00	0.00

Table C. 12: CA results from Set 05 and the average over all sets of repeated experiments with 50% 500-600 μm GWS and 50% 500-600 μm GB, fluidized at $U_g = 2\ U_{mf}$ with dry air, for cubes with side length 1, 10, 20, 30, 40, and 50; after 40 and 60 seconds of fluidizing.

Set 05							Average						
40 seconds, $U_g = 2\ U_{mf}$							40 seconds, $U_g = 2\ U_{mf}$						
bin \ cube	1	10	20	30	40	50	bin \ cube	1	10	20	30	40	50
0	1.32	0.17	0.00	0.00	0.00	0.00	0	1.53	0.30	0.12	0.11	0.00	0.00
0.1	2.08	1.42	1.15	0.00	0.00	0.00	0.1	1.93	1.60	1.21	1.17	0.25	0.00
0.2	12.73	6.65	6.34	2.84	7.89	0.00	0.2	11.60	5.08	4.87	2.75	6.27	1.27
0.3	4.60	13.85	14.99	14.20	19.74	21.21	0.3	4.53	13.47	14.31	12.03	18.99	14.09
0.4	28.78	33.57	35.45	42.61	44.74	57.58	0.4	30.23	36.08	39.82	47.67	53.27	63.14
0.5	33.34	32.86	36.46	37.50	27.63	21.21	0.5	34.56	34.35	36.11	34.47	21.23	21.49
0.6	11.91	9.72	5.33	2.84	0.00	0.00	0.6	11.13	7.89	3.37	1.81	0.00	0.00
0.7	3.55	1.66	0.29	0.00	0.00	0.00	0.7	2.97	1.12	0.20	0.00	0.00	0.00
0.8	0.33	0.10	0.00	0.00	0.00	0.00	0.8	0.28	0.10	0.00	0.00	0.00	0.00
0.9	0.77	0.00	0.00	0.00	0.00	0.00	0.9	0.75	0.01	0.00	0.00	0.00	0.00
1	0.58	0.00	0.00	0.00	0.00	0.00	1	0.49	0.00	0.00	0.00	0.00	0.00
60 seconds, $U_g = 2\ U_{mf}$							60 seconds, $U_g = 2\ U_{mf}$						
bin \ cube	1	10	20	30	40	50	bin \ cube	1	10	20	30	40	50
0	1.19	0.35	0.00	0.00	0.00	0.00	0	1.64	0.48	0.14	0.10	0.00	0.00
0.1	1.42	1.02	1.16	0.00	1.37	0.00	0.1	1.97	1.66	1.49	1.05	1.30	0.00
0.2	10.63	3.79	2.90	1.15	2.74	0.00	0.2	11.80	5.26	4.83	3.84	5.71	2.53
0.3	4.90	13.97	13.77	12.64	20.55	20.59	0.3	4.78	13.60	14.04	13.40	19.73	17.53
0.4	32.19	37.41	41.01	50.57	56.16	55.88	0.4	30.56	37.05	42.47	47.74	50.13	53.99
0.5	35.44	35.64	38.12	34.48	19.18	23.53	0.5	33.75	33.06	32.88	32.30	23.12	25.96
0.6	10.22	6.82	3.04	1.15	0.00	0.00	0.6	10.89	7.59	3.95	1.58	0.00	0.00
0.7	2.51	0.92	0.00	0.00	0.00	0.00	0.7	2.86	1.08	0.20	0.00	0.00	0.00
0.8	0.28	0.07	0.00	0.00	0.00	0.00	0.8	0.28	0.21	0.00	0.00	0.00	0.00
0.9	0.67	0.00	0.00	0.00	0.00	0.00	0.9	0.78	0.01	0.00	0.00	0.00	0.00
1	0.54	0.00	0.00	0.00	0.00	0.00	1	0.68	0.00	0.00	0.00	0.00	0.00

Table C. 13: CA results from Set 01 and Set 02 of repeated experiments with 50% 500-600 μm GWS and 50% 500-600 μm GB, fluidized at $U_g = 3\ U_{mf}$ with dry air, for cubes with side length 1, 10, 20, 30, 40, and 50; initial condition and after 20 seconds of fluidizing.

Set 01							Set 02						
Initial condition, 0 seconds, $U_g = 3\ U_{mf}$							Initial condition, 0 seconds, $U_g = 3\ U_{mf}$						
bin \ cube	1	10	20	30	40	50	bin \ cube	1	10	20	30	40	50
0	0.78	0.02	0.00	0.00	0.00	0.00	0	0.71	0.02	0.00	0.00	0.00	0.00
0.1	0.61	0.22	0.00	0.55	0.00	0.00	0.1	0.80	0.31	0.00	0.00	0.00	0.00
0.2	7.38	1.23	1.06	4.37	0.00	0.00	0.2	7.29	1.65	1.61	0.00	1.39	0.00
0.3	4.38	9.60	8.61	10.93	12.82	9.09	0.3	3.79	8.74	7.89	4.02	15.28	0.00
0.4	36.67	47.92	53.63	48.63	61.54	69.70	0.4	35.47	46.39	55.56	66.09	69.44	81.82
0.5	37.18	34.97	35.05	35.52	25.64	21.21	0.5	42.21	38.81	33.77	29.31	13.89	18.18
0.6	8.08	4.96	1.66	0.00	0.00	0.00	0.6	6.83	3.27	1.02	0.57	0.00	0.00
0.7	3.11	0.94	0.00	0.00	0.00	0.00	0.7	1.07	0.49	0.15	0.00	0.00	0.00
0.8	0.37	0.14	0.00	0.00	0.00	0.00	0.8	0.16	0.24	0.00	0.00	0.00	0.00
0.9	0.92	0.00	0.00	0.00	0.00	0.00	0.9	0.80	0.09	0.00	0.00	0.00	0.00
1	0.52	0.00	0.00	0.00	0.00	0.00	1	0.88	0.00	0.00	0.00	0.00	0.00
20 seconds, $U_g = 3\ U_{mf}$							20 seconds, $U_g = 3\ U_{mf}$						
bin \ cube	1	10	20	30	40	50	bin \ cube	1	10	20	30	40	50
0	1.94	0.64	0.28	0.51	0.00	0.00	0	1.36	0.35	0.00	0.00	0.00	0.00
0.1	1.93	1.71	1.81	4.10	0.00	0.00	0.1	1.29	0.96	1.16	0.00	0.00	0.00
0.2	10.84	3.72	2.78	5.64	4.76	2.86	0.2	7.60	2.68	2.32	0.57	5.26	0.00
0.3	4.64	12.77	14.31	11.28	10.71	20.00	0.3	3.67	8.52	7.67	5.68	9.21	11.76
0.4	32.27	43.10	53.61	57.95	70.24	68.57	0.4	33.98	43.97	51.81	58.52	64.47	67.65
0.5	35.28	33.22	25.56	20.51	14.29	8.57	0.5	41.12	38.75	36.03	35.23	21.05	20.59
0.6	9.60	4.06	1.67	0.00	0.00	0.00	0.6	7.95	4.07	1.01	0.00	0.00	0.00
0.7	1.99	0.61	0.00	0.00	0.00	0.00	0.7	1.46	0.59	0.00	0.00	0.00	0.00
0.8	0.28	0.16	0.00	0.00	0.00	0.00	0.8	0.29	0.12	0.00	0.00	0.00	0.00
0.9	0.70	0.00	0.00	0.00	0.00	0.00	0.9	0.64	0.00	0.00	0.00	0.00	0.00
1	0.53	0.00	0.00	0.00	0.00	0.00	1	0.65	0.00	0.00	0.00	0.00	0.00

Table C. 14: CA results from Set 01 and Set 02 of repeated experiments with 50% 500-600 µm GWS and 50% 500-600 µm GB, fluidized at $U_g = 3\ U_{mf}$ with dry air, for cubes with side length 1, 10, 20, 30, 40, and 50; after 40 and 60 seconds of fluidizing.

Set 01							Set 02						
40 seconds, $U_g = 3\ U_{mf}$							40 seconds, $U_g = 3\ U_{mf}$						
cube / bin	1	10	20	30	40	50	cube / bin	1	10	20	30	40	50
0	1.34	0.08	0.00	0.00	0.00	0.00	0	1.10	0.22	0.00	0.00	0.00	0.00
0.1	1.62	0.87	0.57	3.61	0.00	0.00	0.1	1.30	0.99	0.87	0.00	0.00	0.00
0.2	12.75	4.95	4.53	5.15	2.35	0.00	0.2	8.58	3.01	2.62	1.71	4.05	0.00
0.3	5.24	16.61	15.86	14.95	23.53	18.18	0.3	4.21	10.22	10.32	7.43	14.86	15.63
0.4	31.24	38.90	46.46	49.48	49.41	60.61	0.4	35.15	45.12	50.73	59.43	64.86	56.25
0.5	34.47	32.07	29.89	25.77	24.71	21.21	0.5	38.62	35.03	33.58	31.43	16.22	28.13
0.6	9.33	5.33	2.41	1.03	0.00	0.00	0.6	7.98	4.76	1.89	0.00	0.00	0.00
0.7	2.29	1.02	0.28	0.00	0.00	0.00	0.7	1.64	0.62	0.00	0.00	0.00	0.00
0.8	0.31	0.18	0.00	0.00	0.00	0.00	0.8	0.24	0.03	0.00	0.00	0.00	0.00
0.9	0.71	0.00	0.00	0.00	0.00	0.00	0.9	0.69	0.00	0.00	0.00	0.00	0.00
1	0.70	0.00	0.00	0.00	0.00	0.00	1	0.49	0.00	0.00	0.00	0.00	0.00
60 seconds, $U_g = 3\ U_{mf}$							60 seconds, $U_g = 3\ U_{mf}$						
cube / bin	1	10	20	30	40	50	cube / bin	1	10	20	30	40	50
0	1.52	0.23	0.29	0.00	0.00	0.00	0	1.26	0.44	0.29	0.00	0.00	0.00
0.1	1.93	0.85	0.57	2.63	0.00	0.00	0.1	1.22	1.04	1.16	0.00	0.00	0.00
0.2	13.04	4.88	3.45	8.42	7.06	2.94	0.2	7.95	2.40	2.61	0.58	2.67	0.00
0.3	5.19	16.34	18.25	15.26	21.18	14.71	0.3	3.63	8.52	8.12	5.81	12.00	9.09
0.4	31.99	41.10	44.40	48.95	51.76	73.53	0.4	32.22	40.93	46.23	58.14	61.33	63.64
0.5	33.83	31.27	30.75	23.68	20.00	8.82	0.5	42.07	42.19	41.30	35.47	24.00	27.27
0.6	8.68	4.20	2.30	1.05	0.00	0.00	0.6	9.27	4.33	0.29	0.00	0.00	0.00
0.7	2.16	0.97	0.00	0.00	0.00	0.00	0.7	1.22	0.15	0.00	0.00	0.00	0.00
0.8	0.35	0.16	0.00	0.00	0.00	0.00	0.8	0.18	0.00	0.00	0.00	0.00	0.00
0.9	0.72	0.00	0.00	0.00	0.00	0.00	0.9	0.63	0.00	0.00	0.00	0.00	0.00
1	0.59	0.00	0.00	0.00	0.00	0.00	1	0.35	0.00	0.00	0.00	0.00	0.00

Table C. 15: CA results from Set 03 and Set 04 of repeated experiments with 50% 500-600 μm GWS and 50% 500-600 μm GB, fluidized at $U_g = 3\ U_{mf}$ with dry air, for cubes with side length 1, 10, 20, 30, 40, and 50; initial condition and after 20 seconds of fluidizing.

Set 03							Set 04						
Initial condition, 0 seconds, $U_g = 3\ U_{mf}$							Initial condition, 0 seconds, $U_g = 3\ U_{mf}$						
bin \ cube	1	10	20	30	40	50	bin \ cube	1	10	20	30	40	50
0	1.18	0.43	0.29	0.00	0.00	0.00	0	0.78	0.08	0.00	0.00	0.00	0.00
0.1	1.24	0.87	1.01	0.00	0.00	0.00	0.1	1.00	0.64	0.44	0.00	0.00	0.00
0.2	8.66	2.39	2.01	1.14	3.90	0.00	0.2	8.40	1.90	1.74	0.58	2.70	0.00
0.3	3.99	10.43	9.77	8.52	14.29	15.63	0.3	4.29	10.40	8.43	5.20	10.81	11.76
0.4	36.46	48.62	58.19	70.45	66.23	68.75	0.4	37.02	49.36	59.59	71.10	71.62	73.53
0.5	39.30	33.63	27.59	19.89	15.58	15.63	0.5	37.66	32.62	27.62	22.54	14.86	14.71
0.6	6.47	2.98	1.15	0.00	0.00	0.00	0.6	7.52	3.86	2.03	0.58	0.00	0.00
0.7	1.00	0.55	0.00	0.00	0.00	0.00	0.7	1.71	0.96	0.15	0.00	0.00	0.00
0.8	0.18	0.10	0.00	0.00	0.00	0.00	0.8	0.41	0.18	0.00	0.00	0.00	0.00
0.9	0.59	0.00	0.00	0.00	0.00	0.00	0.9	0.68	0.00	0.00	0.00	0.00	0.00
1	0.93	0.00	0.00	0.00	0.00	0.00	1	0.53	0.00	0.00	0.00	0.00	0.00
20 seconds, $U_g = 3\ U_{mf}$							20 seconds, $U_g = 3\ U_{mf}$						
bin \ cube	1	10	20	30	40	50	bin \ cube	1	10	20	30	40	50
0	1.08	0.17	0.14	0.00	0.00	0.00	0	1.17	0.10	0.00	0.00	0.00	0.00
0.1	1.31	0.92	0.58	0.00	0.00	0.00	0.1	1.39	1.19	0.72	0.00	0.00	0.00
0.2	9.51	3.46	3.32	1.73	2.60	0.00	0.2	9.65	3.52	3.45	1.14	5.19	3.03
0.3	4.35	12.02	12.57	9.83	19.48	27.27	0.3	4.54	11.18	11.94	11.36	16.88	15.15
0.4	33.07	39.02	43.50	56.07	61.04	51.52	0.4	35.72	46.14	51.51	63.64	62.34	63.64
0.5	40.20	39.81	38.58	32.37	16.88	21.21	0.5	37.10	32.80	31.22	23.86	15.58	18.18
0.6	7.64	3.98	1.16	0.00	0.00	0.00	0.6	7.41	4.17	1.15	0.00	0.00	0.00
0.7	1.29	0.54	0.14	0.00	0.00	0.00	0.7	1.45	0.80	0.00	0.00	0.00	0.00
0.8	0.25	0.10	0.00	0.00	0.00	0.00	0.8	0.22	0.10	0.00	0.00	0.00	0.00
0.9	0.62	0.00	0.00	0.00	0.00	0.00	0.9	0.67	0.00	0.00	0.00	0.00	0.00
1	0.68	0.00	0.00	0.00	0.00	0.00	1	0.70	0.00	0.00	0.00	0.00	0.00

Table C. 16: CA results from Set 03 and Set 04 of repeated experiments with 50% 500-600 µm GWS and 50% 500-600 µm GB, fluidized at $U_g = 3\ U_{mf}$ with dry air, for cubes with side length 1, 10, 20, 30, 40, and 50; after 40 and 60 seconds of fluidizing.

Set 03							Set 04						
40 seconds, $U_g = 3\ U_{mf}$							40 seconds, $U_g = 3\ U_{mf}$						
cube / bin	1	10	20	30	40	50	cube / bin	1	10	20	30	40	50
0	1.57	0.28	0.00	0.00	0.00	0.00	0	1.25	0.32	0.14	0.00	0.00	0.00
0.1	1.57	1.40	1.15	0.00	0.00	0.00	0.1	1.52	1.24	1.01	0.00	0.00	0.00
0.2	8.65	3.27	3.30	1.14	3.90	0.00	0.2	9.24	3.52	3.60	2.29	4.00	0.00
0.3	3.90	10.17	10.33	9.14	15.58	15.63	0.3	4.16	10.00	8.21	9.71	14.67	15.63
0.4	34.24	43.45	50.07	61.71	68.83	78.13	0.4	33.60	43.12	52.88	58.29	64.00	62.50
0.5	38.70	36.18	34.15	28.00	11.69	6.25	0.5	38.77	36.57	32.56	29.71	17.33	21.88
0.6	8.15	4.53	1.00	0.00	0.00	0.00	0.6	8.51	4.50	1.59	0.00	0.00	0.00
0.7	1.60	0.67	0.00	0.00	0.00	0.00	0.7	1.61	0.70	0.00	0.00	0.00	0.00
0.8	0.27	0.05	0.00	0.00	0.00	0.00	0.8	0.28	0.03	0.00	0.00	0.00	0.00
0.9	0.69	0.00	0.00	0.00	0.00	0.00	0.9	0.62	0.00	0.00	0.00	0.00	0.00
1	0.66	0.00	0.00	0.00	0.00	0.00	1	0.45	0.00	0.00	0.00	0.00	0.00
60 seconds, $U_g = 3\ U_{mf}$							60 seconds, $U_g = 3\ U_{mf}$						
cube / bin	1	10	20	30	40	50	cube / bin	1	10	20	30	40	50
0	1.51	0.33	0.29	0.00	0.00	0.00	0	1.16	0.25	0.00	0.00	0.00	0.00
0.1	1.68	1.10	0.72	0.00	0.00	0.00	0.1	1.52	1.30	1.30	0.57	0.00	0.00
0.2	9.89	3.55	3.16	1.69	1.30	0.00	0.2	9.17	3.65	3.60	1.14	5.19	3.03
0.3	4.16	12.33	12.34	9.55	18.18	16.13	0.3	3.99	9.80	8.07	5.14	12.99	3.03
0.4	32.49	42.58	48.21	61.24	62.34	64.52	0.4	33.65	43.61	52.74	66.29	64.94	84.85
0.5	38.29	34.29	33.57	27.53	18.18	19.35	0.5	39.33	36.81	33.00	26.86	16.88	9.09
0.6	8.63	4.87	1.58	0.00	0.00	0.00	0.6	8.21	3.96	1.30	0.00	0.00	0.00
0.7	1.55	0.85	0.14	0.00	0.00	0.00	0.7	1.35	0.57	0.00	0.00	0.00	0.00
0.8	0.26	0.08	0.00	0.00	0.00	0.00	0.8	0.19	0.05	0.00	0.00	0.00	0.00
0.9	0.68	0.00	0.00	0.00	0.00	0.00	0.9	0.69	0.00	0.00	0.00	0.00	0.00
1	0.85	0.00	0.00	0.00	0.00	0.00	1	0.76	0.00	0.00	0.00	0.00	0.00

Table C. 17: CA results from Set 05 and the average over all sets of repeated experiments with 50% 500-600 μm GWS and 50% 500-600 μm GB, fluidized at $U_g = 3\ U_{mf}$ with dry air, for cubes with side length 1, 10, 20, 30, 40, and 50; initial condition and after 20 seconds of fluidizing.

Set 05							Average						
Initial condition, 0 seconds, $U_g = 3\ U_{mf}$							Initial condition, 0 seconds, $U_g = 3\ U_{mf}$						
bin \ cube	1	10	20	30	40	50	bin \ cube	1	10	20	30	40	50
0	0.93	0.07	0.00	0.00	0.00	0.00	0	0.88	0.12	0.06	0.00	0.00	0.00
0.1	1.10	0.52	0.29	0.00	0.00	0.00	0.1	0.95	0.51	0.35	0.11	0.00	0.00
0.2	8.51	2.73	2.61	0.57	4.11	0.00	0.2	8.05	1.98	1.81	1.33	2.42	0.00
0.3	4.02	10.89	10.30	6.25	13.70	14.71	0.3	4.10	10.01	9.00	6.99	13.38	10.24
0.4	35.21	44.31	52.39	64.77	68.49	79.41	0.4	36.16	47.32	55.87	64.21	67.47	74.64
0.5	40.13	37.67	33.38	28.41	13.70	5.88	0.5	39.30	35.54	31.48	27.13	16.74	15.12
0.6	7.57	3.30	1.02	0.00	0.00	0.00	0.6	7.29	3.67	1.38	0.23	0.00	0.00
0.7	1.39	0.49	0.00	0.00	0.00	0.00	0.7	1.65	0.69	0.06	0.00	0.00	0.00
0.8	0.20	0.02	0.00	0.00	0.00	0.00	0.8	0.27	0.14	0.00	0.00	0.00	0.00
0.9	0.58	0.00	0.00	0.00	0.00	0.00	0.9	0.71	0.02	0.00	0.00	0.00	0.00
1	0.37	0.00	0.00	0.00	0.00	0.00	1	0.65	0.00	0.00	0.00	0.00	0.00
20 seconds, $U_g = 3\ U_{mf}$							20 seconds, $U_g = 3\ U_{mf}$						
bin \ cube	1	10	20	30	40	50	bin \ cube	1	10	20	30	40	50
0	1.01	0.08	0.00	0.00	0.00	0.00	0	1.31	0.27	0.08	0.10	0.00	0.00
0.1	1.25	0.85	0.43	0.00	0.00	0.00	0.1	1.43	1.13	0.94	0.82	0.00	0.00
0.2	9.79	3.37	3.29	0.00	2.56	0.00	0.2	9.48	3.35	3.03	1.82	4.08	1.18
0.3	4.31	11.16	9.73	9.09	14.10	15.15	0.3	4.30	11.13	11.24	9.45	14.08	17.87
0.4	34.31	44.53	52.50	63.07	70.51	69.70	0.4	33.87	43.35	50.59	59.85	65.72	64.21
0.5	38.34	35.03	32.05	27.84	12.82	15.15	0.5	38.41	35.92	32.69	27.96	16.13	16.74
0.6	7.87	4.24	2.00	0.00	0.00	0.00	0.6	8.09	4.11	1.40	0.00	0.00	0.00
0.7	1.53	0.63	0.00	0.00	0.00	0.00	0.7	1.54	0.63	0.03	0.00	0.00	0.00
0.8	0.28	0.10	0.00	0.00	0.00	0.00	0.8	0.26	0.12	0.00	0.00	0.00	0.00
0.9	0.64	0.00	0.00	0.00	0.00	0.00	0.9	0.65	0.00	0.00	0.00	0.00	0.00
1	0.68	0.00	0.00	0.00	0.00	0.00	1	0.65	0.00	0.00	0.00	0.00	0.00

Table C. 18: CA results from Set 05 and the average over all sets of repeated experiments with 50% 500-600 μm GWS and 50% 500-600 μm GB, fluidized at $U_g = 3\ U_{mf}$ with dry air, for cubes with side length 1, 10, 20, 30, 40, and 50; after 40 and 60 seconds of fluidizing.

Set 05							Average						
40 seconds, $U_g = 3\ U_{mf}$							40 seconds, $U_g = 3\ U_{mf}$						
bin \ cube	1	10	20	30	40	50	bin \ cube	1	10	20	30	40	50
0	1.09	0.00	0.00	0.00	0.00	0.00	0	1.27	0.18	0.03	0.00	0.00	0.00
0.1	1.40	0.69	0.29	0.00	0.00	0.00	0.1	1.48	1.04	0.78	0.72	0.00	0.00
0.2	9.59	4.09	4.02	1.14	3.90	0.00	0.2	9.76	3.77	3.61	2.29	3.64	0.00
0.3	4.26	11.42	12.07	10.29	15.58	21.21	0.3	4.35	11.68	11.36	10.30	16.85	17.25
0.4	34.78	44.73	48.71	62.29	62.34	60.61	0.4	33.80	43.06	49.77	58.24	61.89	63.62
0.5	38.14	33.91	32.33	26.29	18.18	18.18	0.5	37.74	34.75	32.50	28.24	17.63	19.13
0.6	7.46	4.27	2.59	0.00	0.00	0.00	0.6	8.29	4.68	1.89	0.21	0.00	0.00
0.7	1.63	0.87	0.00	0.00	0.00	0.00	0.7	1.75	0.78	0.06	0.00	0.00	0.00
0.8	0.31	0.02	0.00	0.00	0.00	0.00	0.8	0.28	0.06	0.00	0.00	0.00	0.00
0.9	0.69	0.00	0.00	0.00	0.00	0.00	0.9	0.68	0.00	0.00	0.00	0.00	0.00
1	0.66	0.00	0.00	0.00	0.00	0.00	1	0.59	0.00	0.00	0.00	0.00	0.00
60 seconds, $U_g = 3\ U_{mf}$							60 seconds, $U_g = 3\ U_{mf}$						
bin \ cube	1	10	20	30	40	50	bin \ cube	1	10	20	30	40	50
0	0.91	0.08	0.00	0.00	0.00	0.00	0	1.27	0.27	0.17	0.00	0.00	0.00
0.1	1.25	0.74	0.58	0.00	0.00	0.00	0.1	1.52	1.01	0.87	0.64	0.00	0.00
0.2	8.78	2.78	2.92	0.57	2.74	0.00	0.2	9.77	3.45	3.15	2.48	3.79	1.19
0.3	3.79	10.27	9.33	8.05	13.70	14.71	0.3	4.15	11.45	11.22	8.76	15.61	11.53
0.4	32.51	41.16	47.52	57.47	65.75	67.65	0.4	32.57	41.88	47.82	58.42	61.22	70.84
0.5	40.65	40.89	38.92	33.91	17.81	17.65	0.5	38.83	37.09	35.51	29.49	19.37	16.44
0.6	9.69	3.96	0.73	0.00	0.00	0.00	0.6	8.89	4.27	1.24	0.21	0.00	0.00
0.7	1.29	0.12	0.00	0.00	0.00	0.00	0.7	1.51	0.53	0.03	0.00	0.00	0.00
0.8	0.18	0.00	0.00	0.00	0.00	0.00	0.8	0.23	0.06	0.00	0.00	0.00	0.00
0.9	0.61	0.00	0.00	0.00	0.00	0.00	0.9	0.67	0.00	0.00	0.00	0.00	0.00
1	0.35	0.00	0.00	0.00	0.00	0.00	1	0.58	0.00	0.00	0.00	0.00	0.00

Appendix D: Particle Segregation Number (PSN) – Results from All X-ray Experiments

The following tables list the results for all experiments completed with X-ray computed tomography in terms of the Particle Segregation Number (PSN).

Table D. 1: PSN results from experiments with 212-300 µm GWS and 500-600 µm GB at different flow rates, different mixture ratios, with dry or humidified air.

humidified air		no				yes			
time [s]		0	20	40	60	0	20	40	60
mixture ratio	U_g/U_{mf}								
	1	63.6	55.9	59.8	55.9	46.0	61.3	59.0	63.6
25/75	2	61.3	60.5	60.5	56.7	51.3	53.6	53.6	51.3
	3	64.4	60.5	60.5	60.5	57.5	54.4	58.2	49.0
	1	61.3	75.1	75.1	77.4	62.1	88.9	93.5	93.5
50/50	2	55.9	65.9	67.4	69.0	61.3	58.2	59.8	57.5
	3	63.6	66.7	62.1	61.3	39.8	53.6	57.5	51.3
	1	58.2	46.7	46.0	48.3	41.4	57.5	60.5	49.8
75/25	2	42.1	49.8	52.9	52.1	49.8	50.6	46.0	52.9
	3	13.0	39.1	48.3	50.6	49.8	53.6	52.1	51.3

Table D. 2: PSN results from experiments with 500-600 µm GWS and 500-600 µm GB at different flow rates, different mixture ratios, with dry or humidified air.

humidified air		no				yes			
time [s]		0	20	40	60	0	20	40	60
mixture ratio	U_g/U_{mf}								
	1	1.5	56.7	59.8	60.5	15.3	49.0	48.3	53.6
25/75	2	30.7	36.8	36.0	45.2	26.8	47.5	41.4	36.8
	3	24.5	39.8	38.3	43.7	35.2	40.6	46.0	33.0
	1	55.9	75.1	84.3	82.8	16.1	84.3	92.7	94.3
50/50	2	34.5	46.7	42.9	49.0	20.7	52.1	37.5	39.1
	3	23.8	31.4	42.9	42.1	-15.3	26.1	39.8	26.1
	1	-8.4	76.6	88.1	92.7	42.9	101.9	102.7	99.6
75/25	2	15.3	89.7	85.1	89.7	16.1	69.7	68.2	78.2
	3	-7.7	34.5	22.2	37.5	-10.0	34.5	40.6	19.2

Table D. 3: PSN results from experiments with 800-1000 µm GWS and 500-600 µm GB at different flow rates, different mixture ratios, with dry or humidified air.

humidified air		no				yes			
time [s]		0	20	40	60	0	20	40	60
mixture ratio	U_g/U_{mf}								
	1	21.5	20.7	27.6	33.7	25.3	31.4	16.1	30.7
25/75	2	1.5	33.0	28.4	27.6	16.1	29.9	19.9	23.0
	3	9.2	22.2	31.4	26.8	6.9	27.6	26.8	26.8
	1	28.4	59.8	66.7	72.8	18.4	49.8	58.2	60.5
50/50	2	14.6	23.8	19.2	21.5	25.3	17.6	19.9	24.5
	3	13.8	17.6	17.6	22.2	26.1	16.1	15.3	19.9
	1	26.8	45.2	63.6	75.9	29.9	46.7	52.9	52.1
75/25	2	28.4	7.7	12.3	10.0	12.3	13.0	16.9	20.7
	3	11.5	16.1	15.3	8.4	22.2	20.7	19.9	20.7

Appendix E: Visual Results

The following is a list of figures illustrating the results of all experiments completed during the preliminary data acquisition phase through visual observations. All photographs have been visually enhanced and modified for better illustration and to fit the format of this report and should therefore only be used for qualitative analysis.

(C) Results from Experiments with 9.5 cm ID FBR

Figure E. 1: Photographs of experiments with 25% 212-300 μm GCC mixed with 75% 500-600 μm GB and fluidized at $U_g = 2\ U_{mf}$ with dry air in the 9.5 cm ID FBR at the specified intervals.

Figure E. 2: Photographs of experiments with 25% 212-300 μm GCC mixed with 75% 500-600 μm GB and fluidized at $U_g = 2\ U_{mf}$ with humidified air in the 9.5 cm ID FBR at the specified intervals.

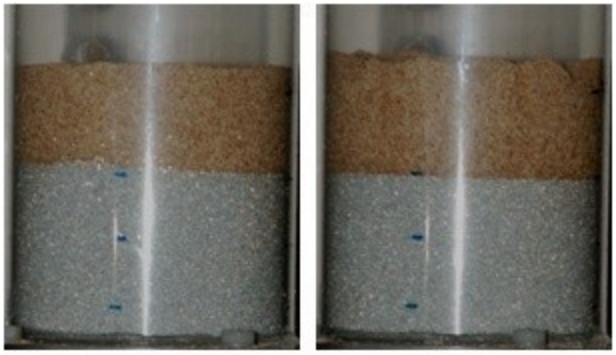

Figure E. 3: Photographs of experiments with 25% 212-300 μm GCC mixed with 75% 500-600 μm GB and fluidized at U_g = 1 U_{mf} with humidified air in the 9.5 cm ID FBR at the specified intervals.

Figure E. 4: Photographs of experiments with 25% 212-300 μm GCC mixed with 75% 500-600 μm GB and fluidized at U_g = 1.5 U_{mf} with humidified air in the 9.5 cm ID FBR at the specified intervals.

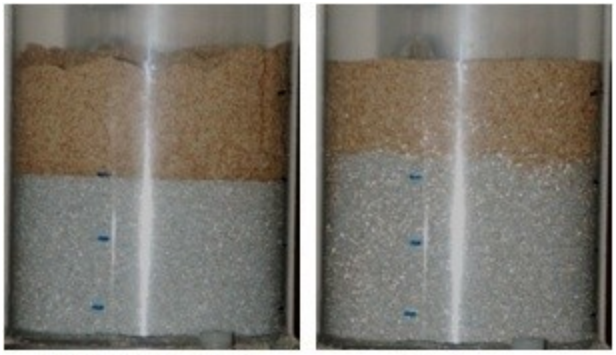

Figure E. 5: Photographs of experiments with 25% 212-300 μm GCC mixed with 75% 500-600 μm GB and fluidized at $U_g = 2.6\ U_{mf}$ with humidified air in the 9.5 cm ID FBR at the specified intervals.

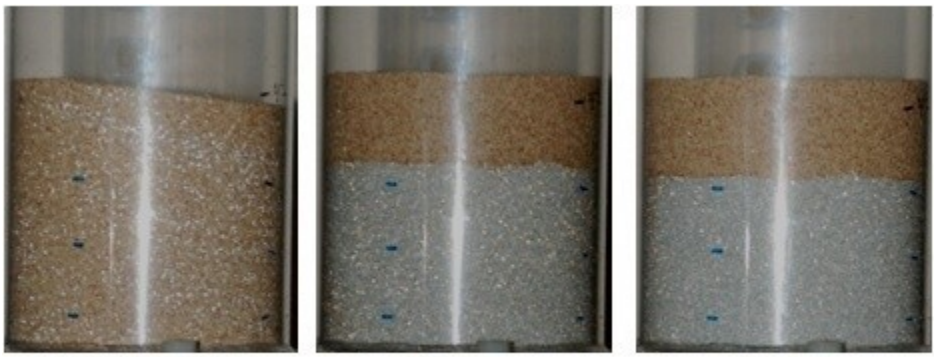

Figure E. 6: Photographs of experiments with 25% 212-300 μm GCC mixed with 75% 500-600 μm GB and fluidized at $U_g = 2\ U_{mf}$ with humidified air in the 9.5 cm ID FBR at the specified intervals.

Figure E. 7: Photographs of experiments with 25% 500-600 μm GCC mixed with 75% 500-600 μm GB and fluidized at $U_g = 2\ U_{mf}$ with humidified air in the 9.5 cm ID FBR at the specified intervals.

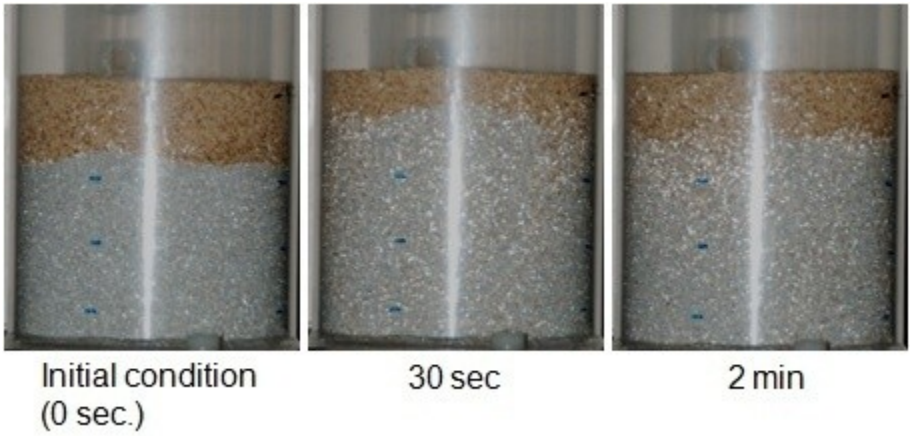

Figure E. 8: Photographs of experiments with 25% 500-600 μm GCC mixed with 75% 500-600 μm GB and fluidized at $U_g = 3\ U_{mf}$ with humidified air in the 9.5 cm ID FBR at the specified intervals.

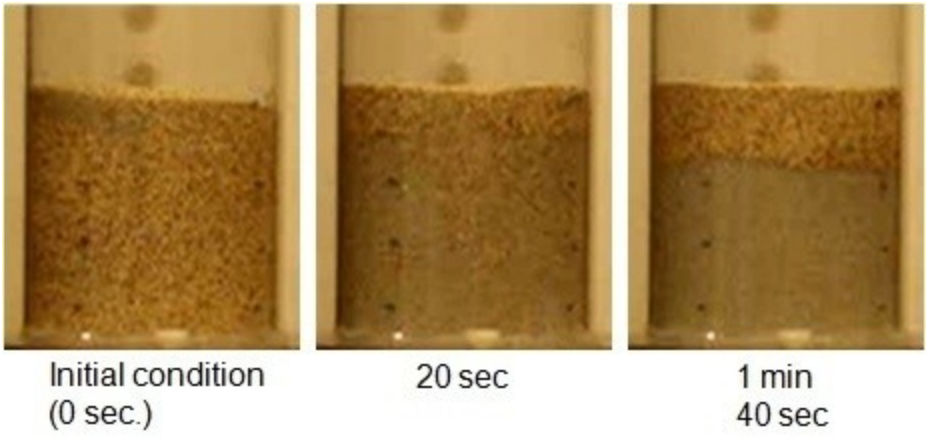

Figure E. 9: Photographs of experiments with 25% 500-600 μm GCC mixed with 75% 500-600 μm GB and fluidized at $U_g = 2\ U_{mf}$ with humidified air in the 9.5 cm ID FBR at the specified intervals.

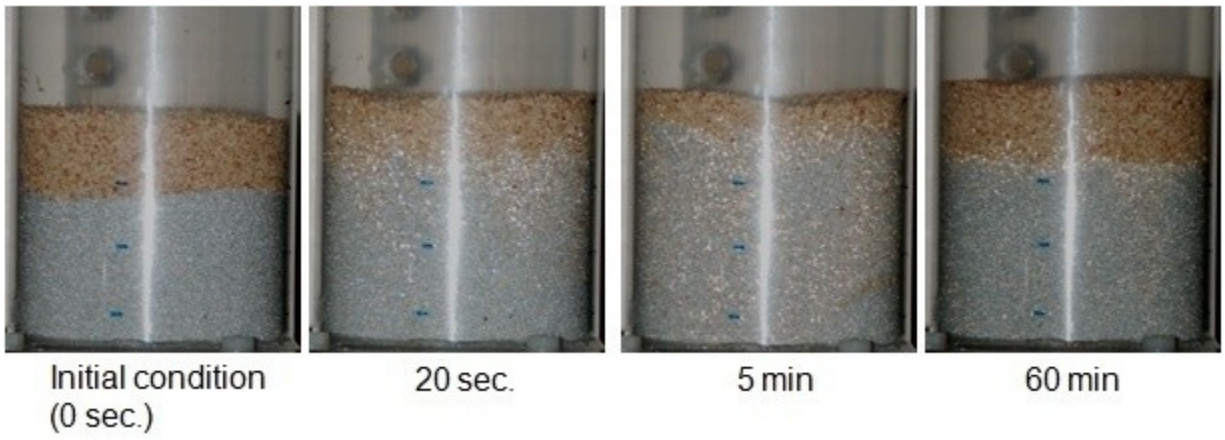

Figure E. 10: Photographs of experiments with 25% 800-1000 μm GCC mixed with 75% 500-600 μm GB and fluidized at $U_g = 2\ U_{mf}$ with humidified air in the 9.5 cm ID FBR at the specified intervals.

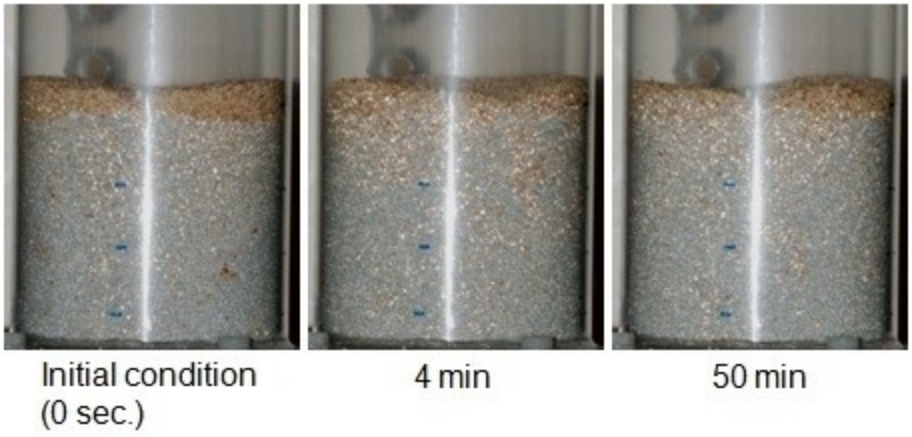

Figure E. 11: Photographs of experiments with 25% 800-1000 μm GCC mixed with 75% 500-600 μm GB and fluidized at $U_g = 3\ U_{mf}$ with humidified air in the 9.5 cm ID FBR at the specified intervals.

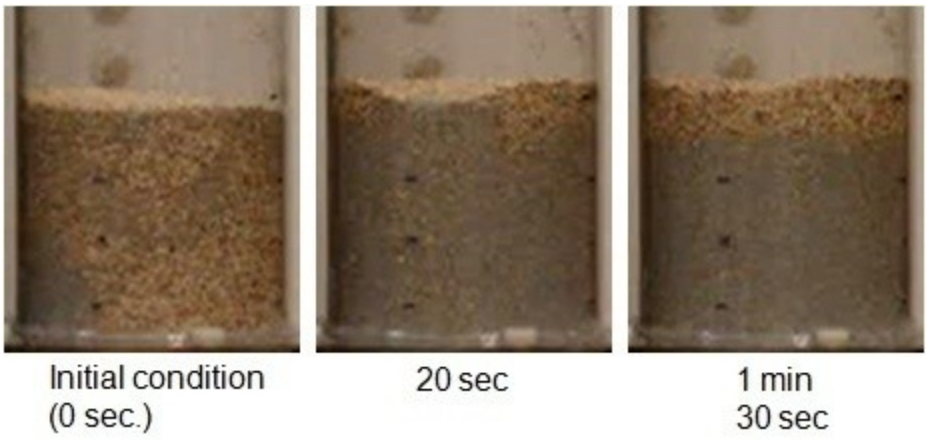

Figure E. 12: Photographs of experiments with 25% 800-1000 μm GCC mixed with 75% 500-600 μm GB and fluidized at $U_g = 2\ U_{mf}$ with humidified air in the 9.5 cm ID FBR at the specified intervals.

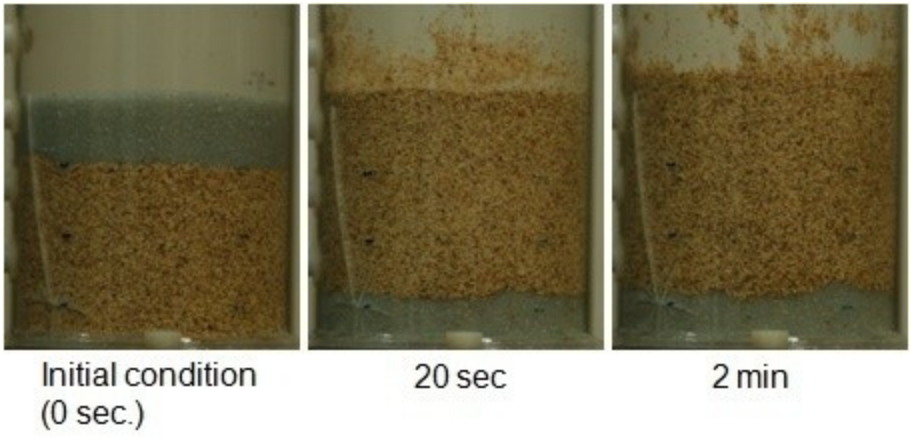

Figure E. 13: Photographs of experiments with 75% 500-600 μm GCC mixed with 25% 500-600 μm GB and fluidized at $U_g = 2\ U_{mf}$ with humidified air in the 9.5 cm ID FBR at the specified intervals.

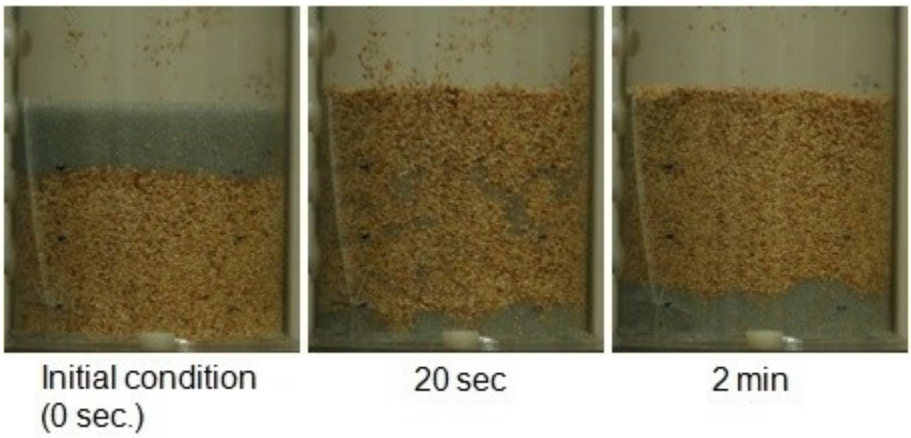

Figure E. 14: Photographs of experiments with 75% 800-1000 μm GCC mixed with 25% 500-600 μm GB and fluidized at $U_g = 2\ U_{mf}$ with humidified air in the 9.5 cm ID FBR at the specified intervals.

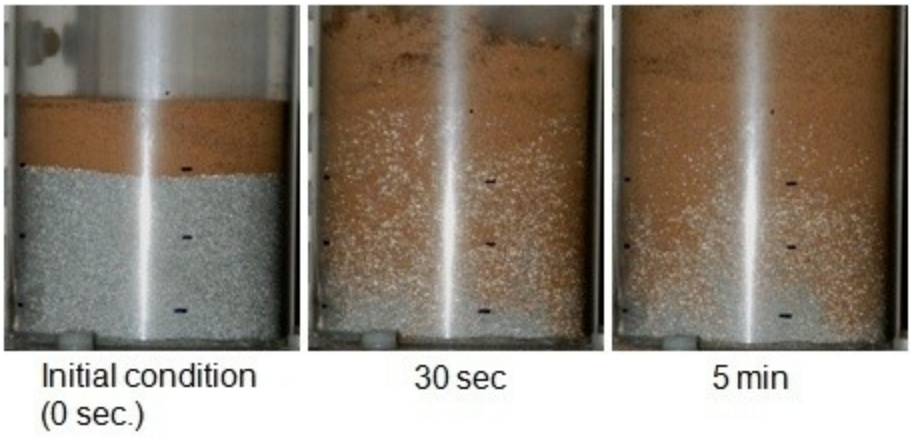

Figure E. 15: Photographs of experiments with 25% 212-300 μm GWS mixed with 75% 500-600 μm GB and fluidized at $U_g = 2\ U_{mf}$ with dry air in the 9.5 cm ID FBR at the specified intervals.

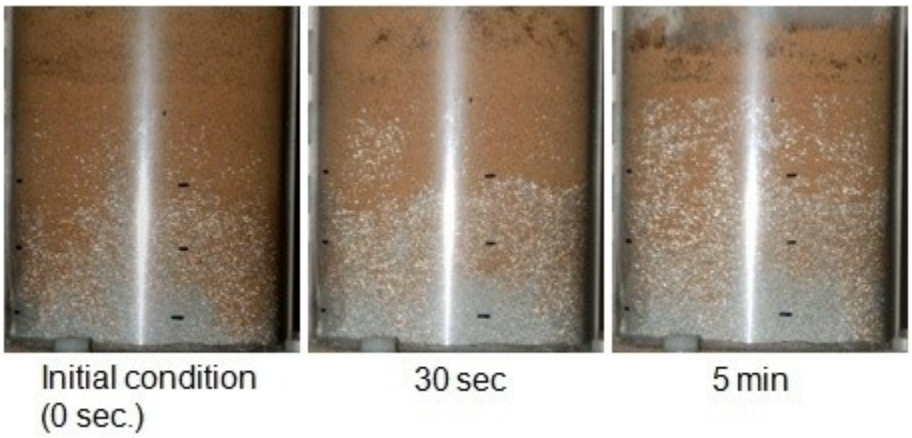

Figure E. 16: Photographs of experiments with 25% 212-300 μm GWS mixed with 75% 500-600 μm GB and fluidized at $U_g = 2\ U_{mf}$ with humidified air in the 9.5 cm ID FBR at the specified intervals.

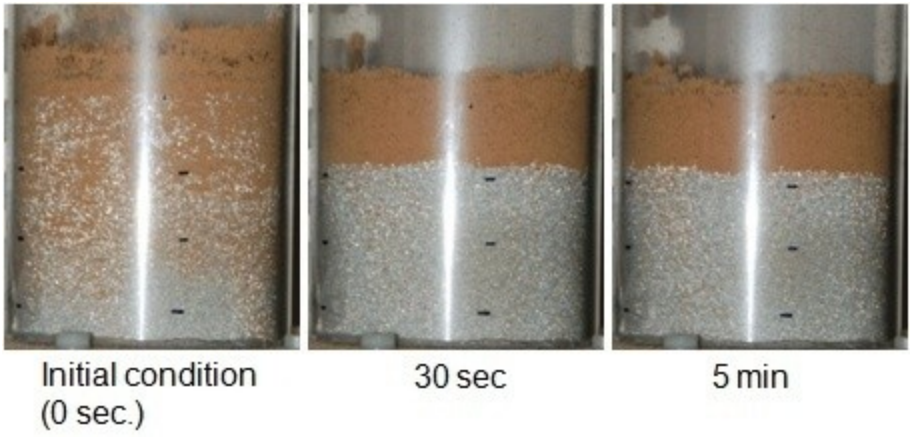

Figure E. 17: Photographs of experiments with 25% 212-300 μm GWS mixed with 75% 500-600 μm GB and fluidized at U_g = 1.5 U_{mf} with humidified air in the 9.5 cm ID FBR at the specified intervals.

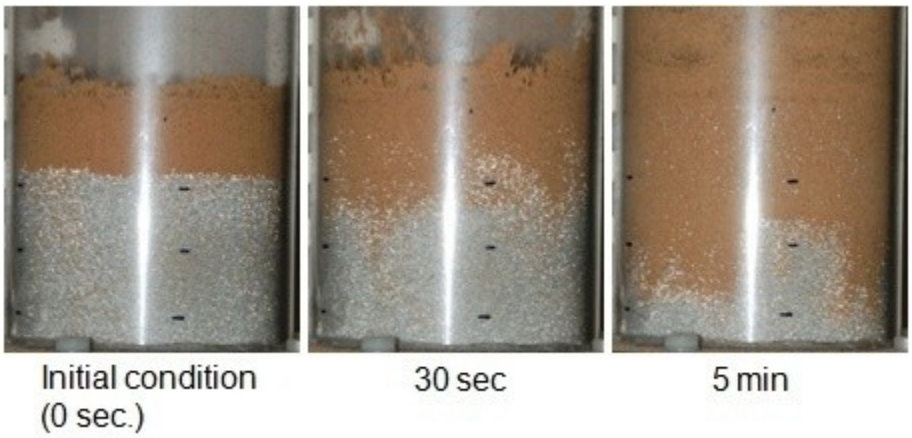

Figure E. 18: Photographs of experiments with 25% 212-300 μm GWS mixed with 75% 500-600 μm GB and fluidized at U_g = 1.5 U_{mf} with dry air in the 9.5 cm ID FBR at the specified intervals.

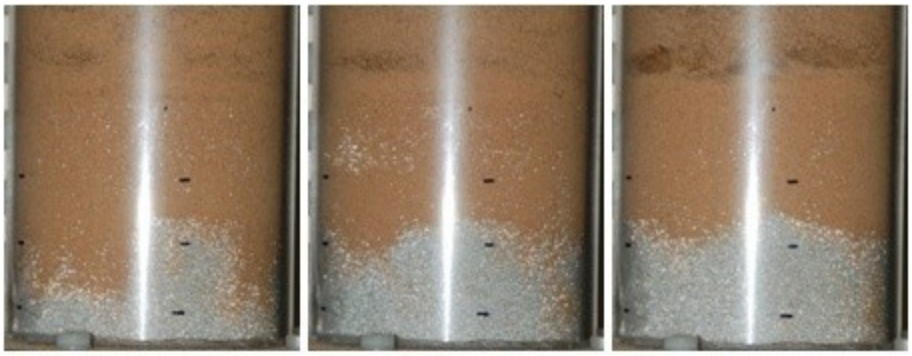

Figure E. 19: Photographs of experiments with 25% 212-300 μm GWS mixed with 75% 500-600 μm GB and fluidized at $U_g = 1.2\ U_{mf}$ with dry air in the 9.5 cm ID FBR at the specified intervals.

Figure E. 20: Photographs of experiments with 25% 500-600 μm GWS mixed with 75% 500-600 μm GB and fluidized at $U_g = 2\ U_{mf}$ with dry air in the 9.5 cm ID FBR at the specified intervals.

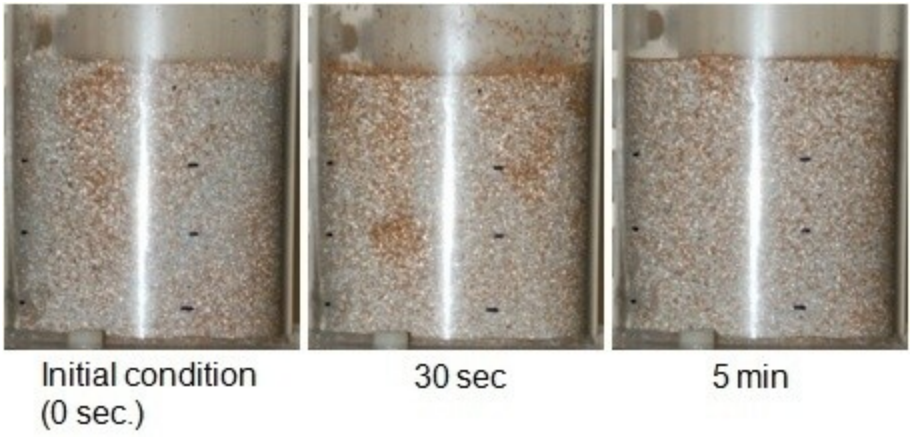

Figure E. 21: Photographs of experiments with 25% 500-600 μm GWS mixed with 75% 500-600 μm GB and fluidized at $U_g = 2\ U_{mf}$ with humidified air in the 9.5 cm ID FBR at the specified intervals.

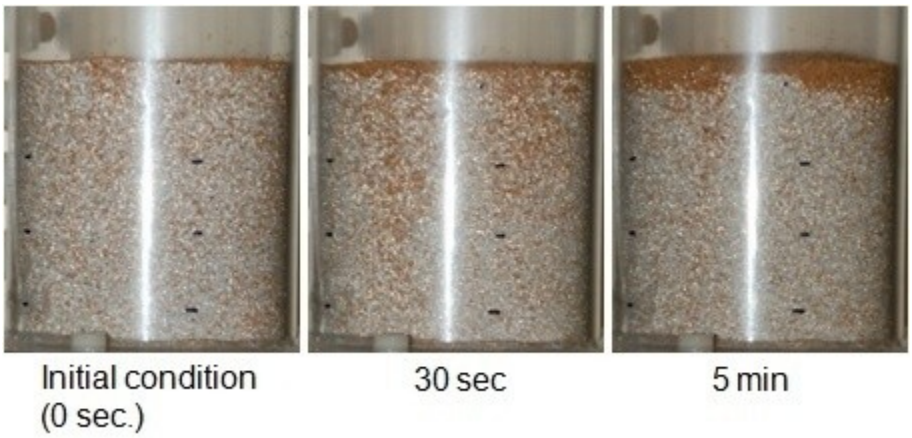

Figure E. 22: Photographs of experiments with 25% 500-600 μm GWS mixed with 75% 500-600 μm GB and fluidized at $U_g = 1.5\ U_{mf}$ with humidified air in the 9.5 cm ID FBR at the specified intervals.

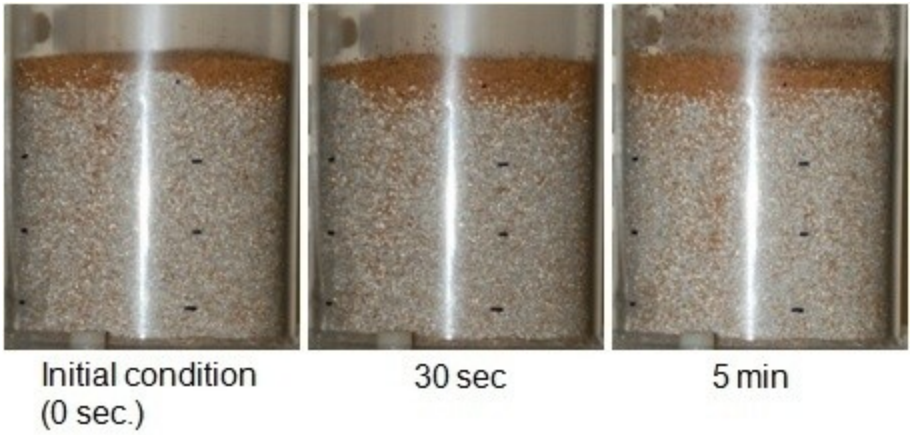

Figure E. 23: Photographs of experiments with 25% 500-600 μm GWS mixed with 75% 500-600 μm GB and fluidized at U_g = 1.5 U_{mf} with dry air in the 9.5 cm ID FBR at the specified intervals.

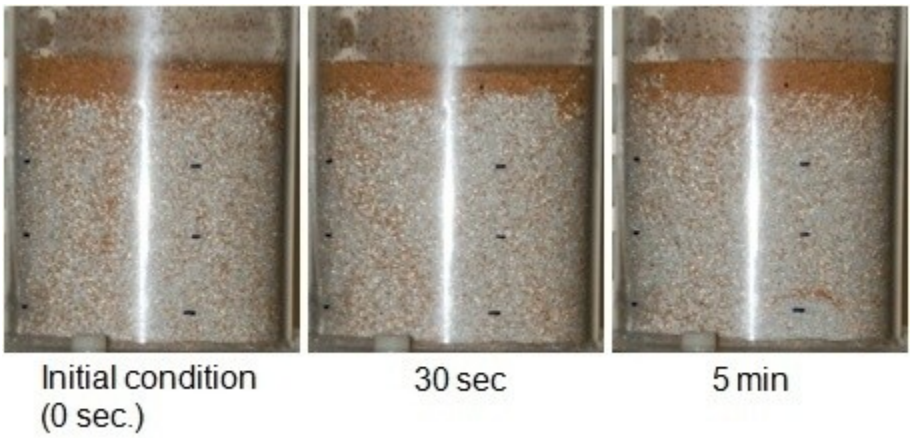

Figure E. 24: Photographs of experiments with 25% 500-600 μm GWS mixed with 75% 500-600 μm GB and fluidized at U_g = 1.2 U_{mf} with dry air in the 9.5 cm ID FBR at the specified intervals.

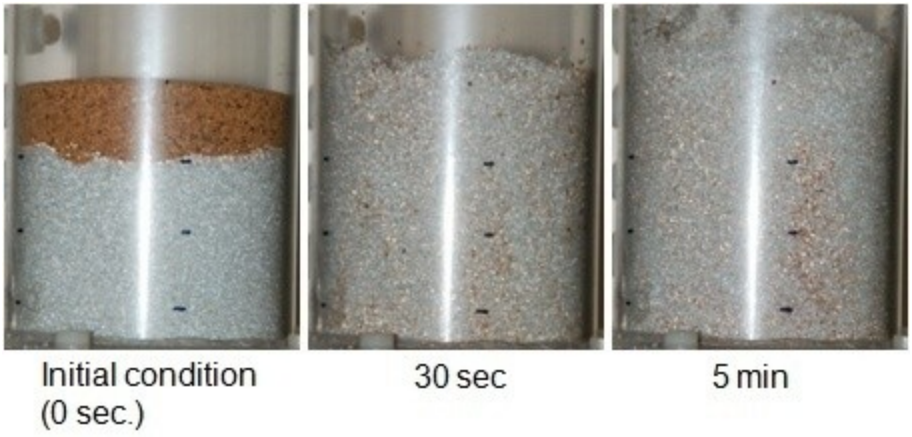

Figure E. 25: Photographs of experiments with 25% 800-1000 μm GWS mixed with 75% 500-600 μm GB and fluidized at $U_g = 2\ U_{mf}$ with dry air in the 9.5 cm ID FBR at the specified intervals.

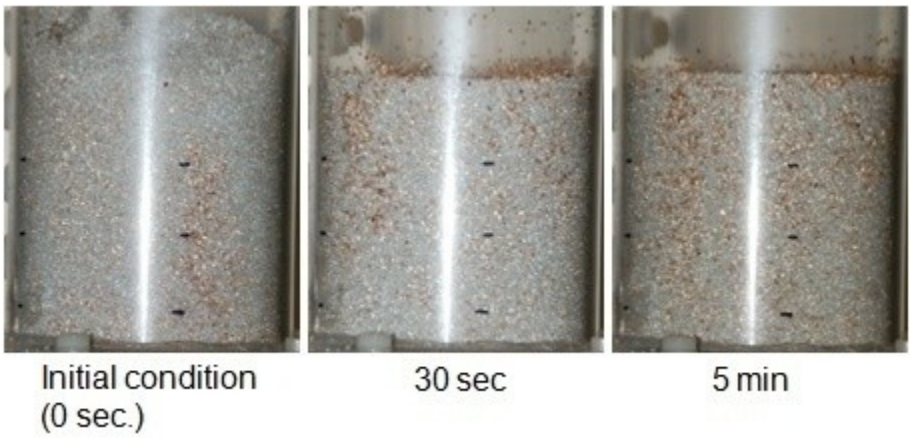

Figure E. 26: Photographs of experiments with 25% 800-1000 μm GWS mixed with 75% 500-600 μm GB and fluidized at $U_g = 2\ U_{mf}$ with humidified air in the 9.5 cm ID FBR at the specified intervals.

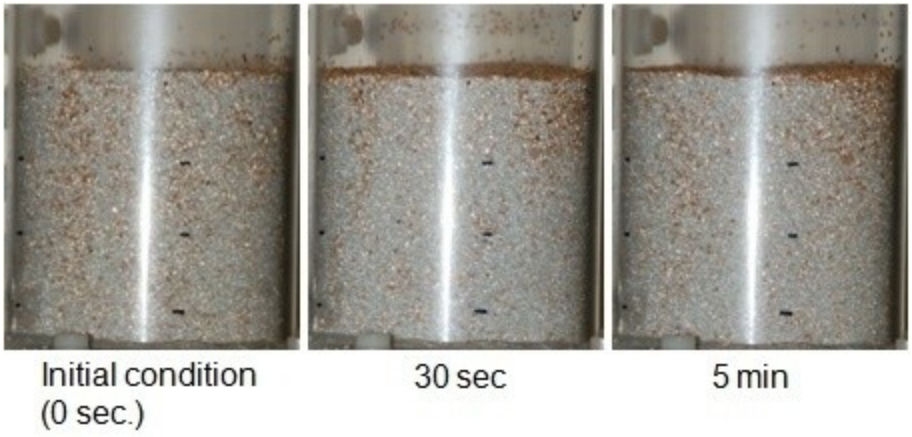

Figure E. 27: Photographs of experiments with 25% 800-1000 μm GWS mixed with 75% 500-600 μm GB and fluidized at U_g = 1.5 U_{mf} with humidified air in the 9.5 cm ID FBR at the specified intervals.

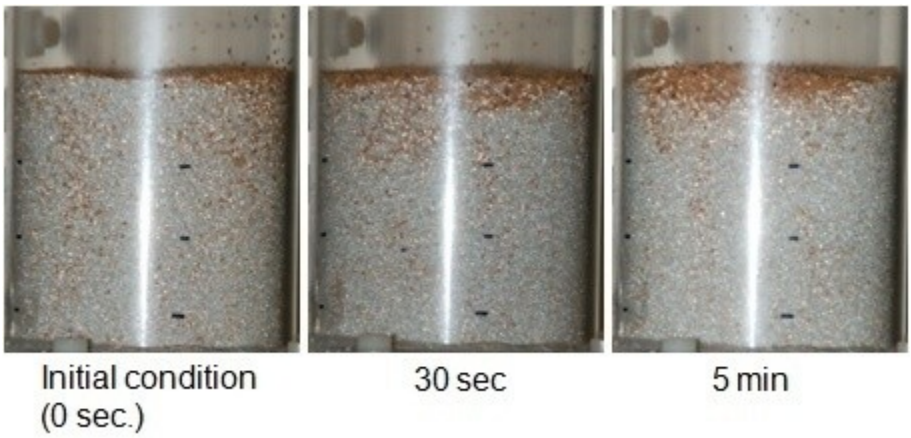

Figure E. 28: Photographs of experiments with 25% 800-1000 μm GWS mixed with 75% 500-600 μm GB and fluidized at U_g = 1.5 U_{mf} with dry air in the 9.5 cm ID FBR at the specified intervals.

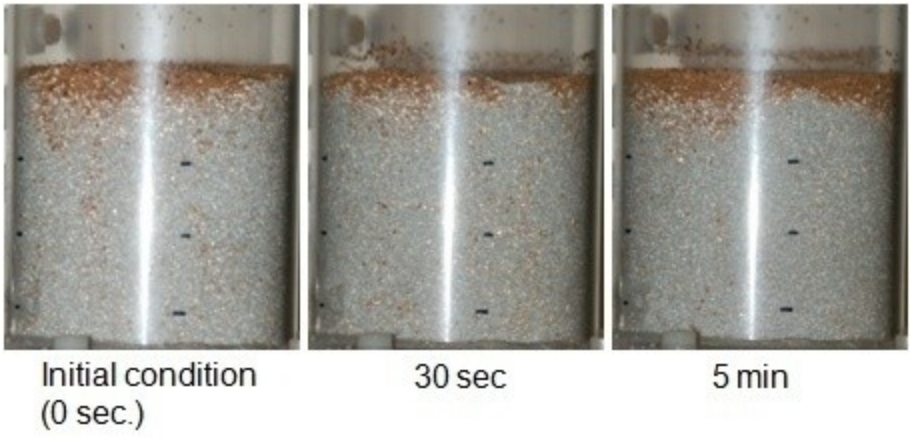

Figure E. 29: Photographs of experiments with 25% 800-1000 μm GWS mixed with 75% 500-600 μm GB and fluidized at $U_g = 1.2\ U_{mf}$ with dry air in the 9.5 cm ID FBR at the specified intervals.

(D) Results from Experiments with 15.2 cm ID FBR

Figure E. 30: Photographs of experiments with 25% 212-300 μm GWS mixed with 75% 500-600 μm GB and fluidized at $U_g = 2\ U_{mf}$ with dry air in the 15.2 cm ID FBR at the specified intervals.

Figure E. 31: Photographs of experiments with 25% 212-300 μm GWS mixed with 75% 500-600 μm GB and fluidized at $U_g = 2\ U_{mf}$ with humidifed air in the 15.2 cm ID FBR at the specified intervals.

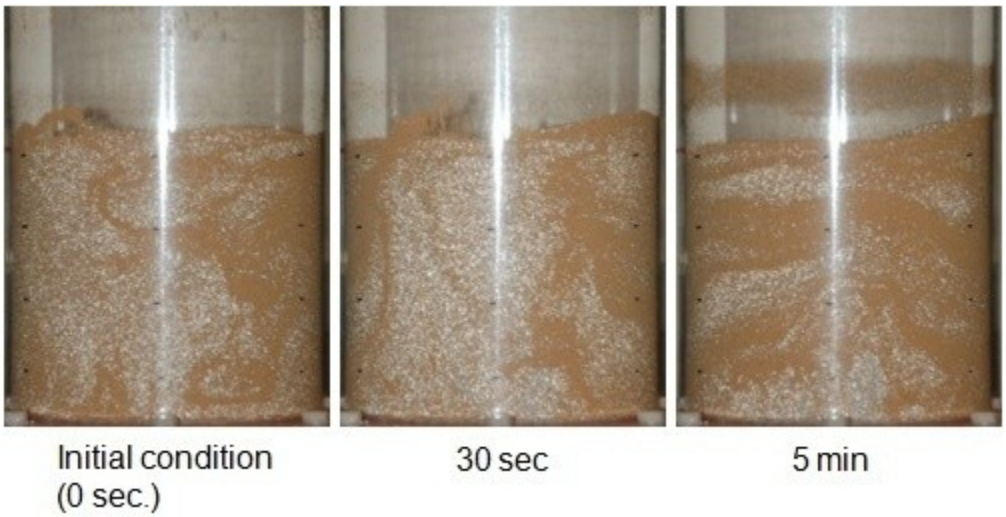

Figure E. 32: Photographs of experiments with 25% 212-300 μm GWS mixed with 75% 500-600 μm GB and fluidized at $U_g = 1.5\ U_{mf}$ with humidifed air in the 15.2 cm ID FBR at the specified intervals.

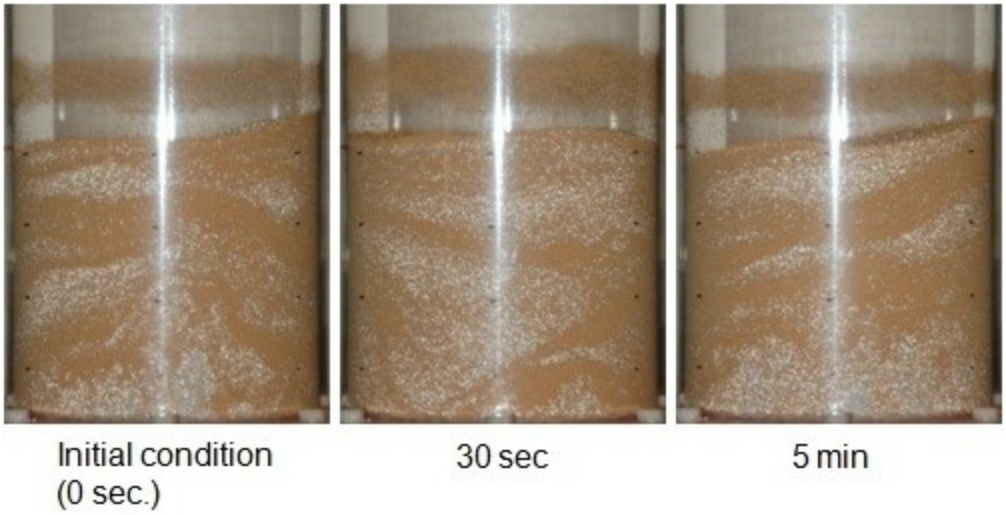

Figure E. 33: Photographs of experiments with 25% 212-300 μm GWS mixed with 75% 500-600 μm GB and fluidized at U_g = 1.5 U_{mf} with dry air in the 15.2 cm ID FBR at the specified intervals.

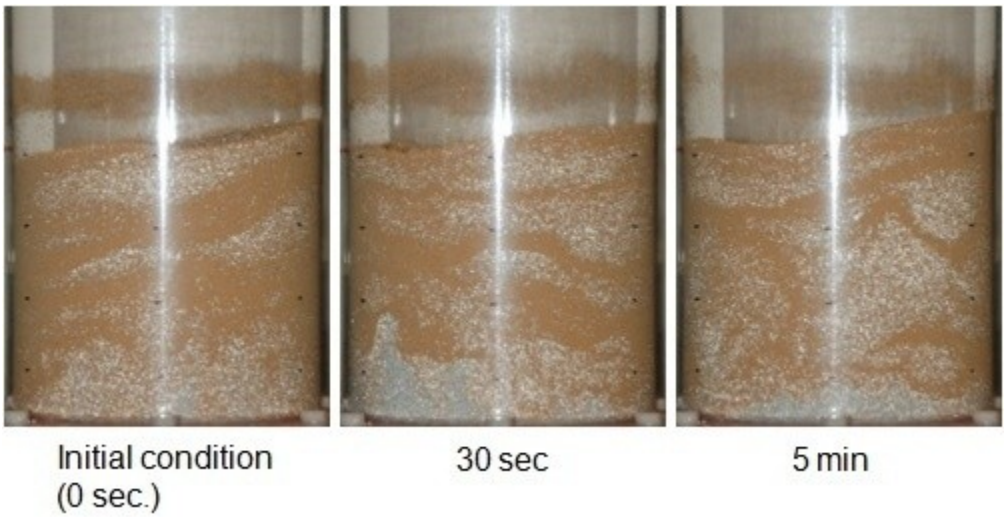

Figure E. 34: Photographs of experiments with 25% 212-300 μm GWS mixed with 75% 500-600 μm GB and fluidized at U_g = 1.2 U_{mf} with dry air in the 15.2 cm ID FBR at the specified intervals.

Figure E. 35: Photographs of experiments with 25% 500-600 µm GWS mixed with 75% 500-600 µm GB and fluidized at $U_g = 2\ U_{mf}$ with dry air in the 15.2 cm ID FBR at the specified intervals.

Figure E. 36: Photographs of experiments with 25% 500-600 µm GWS mixed with 75% 500-600 µm GB and fluidized at $U_g = 2\ U_{mf}$ with humidified air in the 15.2 cm ID FBR at the specified intervals.

Figure E. 37: Photographs of experiments with 25% 500-600 µm GWS mixed with 75% 500-600 µm GB and fluidized at U_g = 1.5 U_{mf} with humidified air in the 15.2 cm ID FBR at the specified intervals.

Figure E. 38: Photographs of experiments with 25% 500-600 µm GWS mixed with 75% 500-600 µm GB and fluidized at U_g = 1.5 U_{mf} with dry air in the 15.2 cm ID FBR at the specified intervals.

Figure E. 39: Photographs of experiments with 25% 500-600 μm GWS mixed with 75% 500-600 μm GB and fluidized at U_g = 1.2 U_{mf} with dry air in the 15.2 cm ID FBR at the specified intervals.

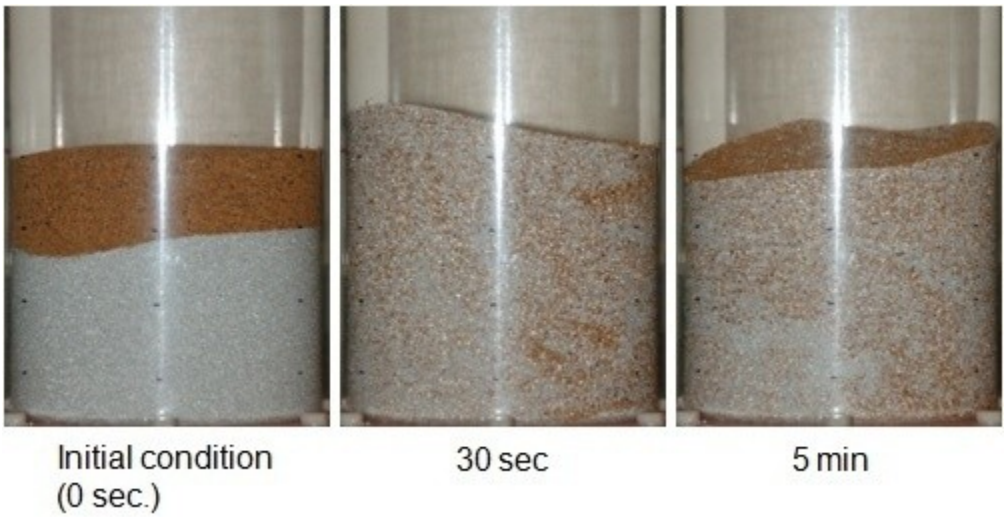

Figure E. 40: Photographs of experiments with 25% 800-1000 μm GWS mixed with 75% 500-600 μm GB and fluidized at U_g = 2 U_{mf} with dry air in the 15.2 cm ID FBR at the specified intervals.

Figure E. 41: Photographs of experiments with 25% 800-1000 μm GWS mixed with 75% 500-600 μm GB and fluidized at $U_g = 2\ U_{mf}$ with humidified air in the 15.2 cm ID FBR at the specified intervals.

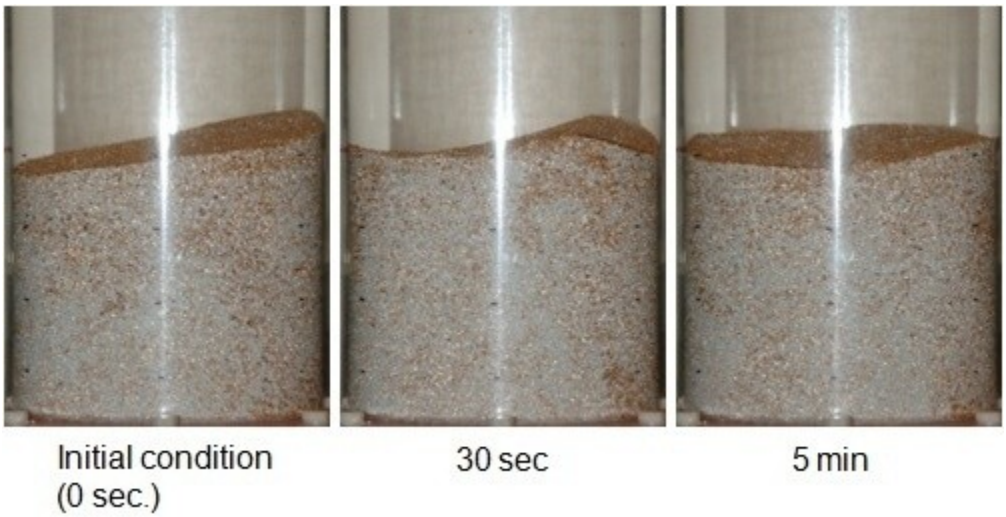

Figure E. 42: Photographs of experiments with 25% 800-1000 μm GWS mixed with 75% 500-600 μm GB and fluidized at $U_g = 1.5\ U_{mf}$ with humidified air in the 15.2 cm ID FBR at the specified intervals.

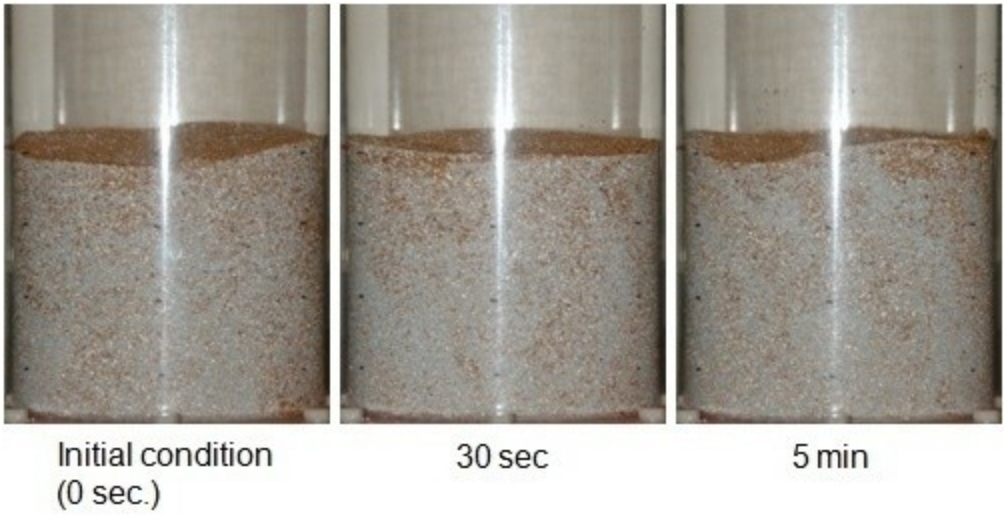

Figure E. 43: Photographs of experiments with 25% 800-1000 μm GWS mixed with 75% 500-600 μm GB and fluidized at U_g = 1.5 U_{mf} with dry air in the 15.2 cm ID FBR at the specified intervals.

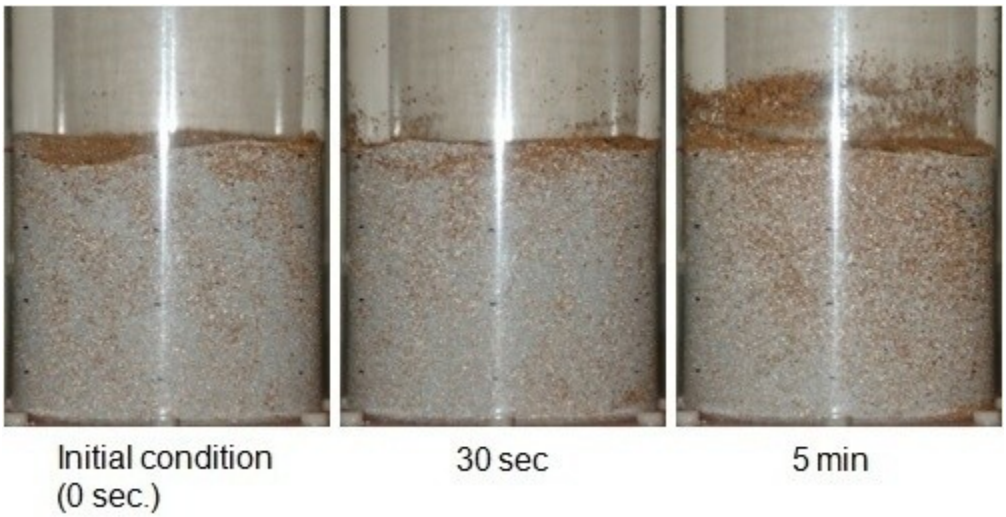

Figure E. 44: Photographs of experiments with 25% 800-1000 μm GWS mixed with 75% 500-600 μm GB and fluidized at U_g = 1.5 U_{mf} with dry air in the 15.2 cm ID FBR at the specified intervals.